Antal Kerpely Doctoral School of Materials Science and Technology

Innovative Development and Investigation of Doped and Cu-Composite $BaTiO_3$ Materials for Advanced Multilayer Ceramic Capacitors

A Dissertation Submitted in Partial Fulfillment of the Requirements for the Degree of Doctor of Philosophy in Ceramics Engineering as a Part of Stipendium Hungaricum Scholarship in Material Science and Technology

By
Mohammed Tihtih

Supervisor:
Dr. István Kocserha, Associate Professor

Head of the Doctoral School
Prof. Dr. Valéria Mertinger

Institute of Ceramic and Polymer Engineering
Faculty of Materials and Chemical Engineering
University of Miskolc
Miskolc, Hungary
2024

“You may say anything you like but, we all are made up of ferroelectrics.”

B. T. Matthias

ACKNOWLEDGEMENT

My success in this Ph.D. program could not have been achieved without the deep cooperation, invaluable assistance, and ongoing support of many individuals. Through these few sentences, I would like to express my heartfelt thanks to them.

First and foremost, I am immensely grateful to my previous supervisor, *Prof. László A. Gömze*, for his overwhelming support, advice, encouragement, commitment, and supervision from the start until midway through my Ph.D. candidature at the University of Miskolc. *Prof. Gömze*, who passed away in January 2022, was a dedicated and supportive person with a great passion for research. My deepest appreciation goes to my current supervisor, *Dr. Kocserha István*, who has always been actively engaged in my Ph.D. project by guiding, inspiring, and supporting me, including correcting my thesis and giving meaningful advice. I could not have completed this research without his extensive support.

I would like to thank all the respected professors at the University of Miskolc who taught me various subjects over the first two years of the Ph.D. program. I am also grateful to the reviewer, *Dr. Béla Fiser*, for his insightful comments and suggestions on several aspects of my study; his constant support and positive opinions about my work during the whole Ph.D. course helped me achieve the desired outcomes. I extend my thanks to *Dr. Katalin Balázsi*, *Dr. Béla Fiser*, and *Prof. Peter Baumli* for their valuable questions, feedback, and comments on my dissertation. Their careful review and constructive suggestions have significantly improved this dissertation.

I also thank *Dr. Jamal Eldin Fadoul Mohammed Ibrahim* and *Dr. Emese Kurovics* for their unlimited support in the experimental work. My thanks extend to *Dr. Daniel Koncz-Horvath* for his assistance in conducting investigations related to scanning electron microscopy and energy dispersive spectroscopy, and to *Dr. Tamás Szabó* and *Ms. Ildikó Tasnádi* for their help with conducting FT-IR analysis. I express my deepest appreciation to all the staff members in the Antal Kerpely Doctoral School of Materials Science and Technology, University of Miskolc, for their advice, technical support, continual assistance, and cooperation during the experimental work over the past years.

I am sincerely grateful to *Ms. Agnes Solczi*, not only for being our faculty coordinator and facilitating all administrative work but also for her encouragement, support, and generous invitations to join her hiking trips. I also extend my thanks to my colleagues for their useful and enjoyable study, experimentation, and collaboration, as well as for sharing their extensive and valuable practical skills and knowledge with me.

I acknowledge the Hungarian government for providing me with a full scholarship during my Ph.D. study. Special thanks go to my close colleague, *Dr. Jamal Eldin Fadoul Mohammed Ibrahim*, for his encouragement, understanding, and support throughout my Ph.D. journey.

Finally, my love and deep gratitude go to my parents and all my family members, who have always provided me with their unconditional love, encouragement, and profound support throughout my Ph.D. program and academic career.

Mohammed Tihtih
May 2024

Contents

LIST OF FIGURES

LIST OF TABLES

LIST OF ABBREVIATIONS

BT	**B**arium **T**itanate
MLCCs	**M**ultilayer **C**eramic **C**apacitors
PCMs	**P**hase **T**ransition **M**aterials
XRD	**X**-**R**ay **D**iffraction
SEM	**S**canning **E**lectron **M**icroscope
EDS	**E**nergy **D**ispersive **S**pectroscopy
TGA	**T**hermal **G**ravimetric **A**nalysis
DTA	**D**ifferential **T**hermal **A**nalysis
2θ	**D**iffraction **A**ngles
λ	**W**avelength
PDF	**P**owder **D**iffraction **F**ile
FWHM	**F**ull **W**idth at the **H**alf **M**aximum
MMC	**M**etal–**M**atrix **C**omposite
RT	**R**oom **T**emperature
FT-IR	**F**ourier **T**ransform **I**nfrared
Cu	**C**opper
Sr	**S**trontium
Y	**Y**ttrium
BST	**B**arium **S**trontium **T**itanate
V	**V**olume of the **U**nit **C**ell
VBM	**V**alence **B**and **M**aximum
CBM	**C**onduction **B**and **M**inimum
EDAX	**E**nergy-**D**ispersive **X**-ray **S**pectrometer
TC	**T**hermal **C**onductivity
R	**R**esistance
C	**C**apacitance
BSrT	$Ba_{1-x}Sr_xTiO_3$
BYT	$Ba_{1-x}Y_xTiO_3$
BSrTY	$BaTi_{1-x}Y_xO_3$
BTY	$Ba_{1-x}Y_xTi_{1-x}Y_xO_3$
BYTY	$Ba_{1-x}Sr_xTi_{1-x}Y_xO_3$

Abstract

Electroceramics are necessary component in modern technologies of many kinds. In this regard, barium meta-titanate ($BaTiO_3$ or BT) based materials with ABO_3 perovskite structure are potential candidates for applications in electronic devices because of their piezoelectric, ferroelectric, and optical properties. Barium titanate-based materials have attracted significant interest, due to their widespread applications in wireless communication, space and defense. Barium titanate based ferroelectric materials are suitable for these applications due to their electric field dependent permittivity (ε_r) and low dielectric loss (tan δ) above Curie temperature (Tc). Ferroelectric materials generally have high dielectric losses, which is due to piezoelectric grain resonance and domain wall motion.

This thesis investigates the synthesis, characterization, and properties of doped $BaTiO_3$ ceramics prepared using a modified sol-gel method. Various compositions including $BaTiO_3$, $Ba_{1-x}Sr_xTiO_3$, $Ba_{1-x}Y_xTiO_3$, $BaTi_{1-x}Y_xO_3$, $Ba_{1-x}Y_xTi_{1-x}Y_xO_3$, and $Ba_{1-x}Sr_xTi_{1-x}Y_xO_3$ ($x=0.075$) were successfully synthesized and characterized for their structural, microstructural, chemical compositional stoichiometry, optical, thermal conductivity, and mechanical properties. X-ray diffraction (XRD) and Rietveld refinement revealed the tetragonal structure of BT, BSrT, and BYT ceramics, while BSrTY, BTY, and BYTY samples exhibited a cubic structure. Fourier-transform infrared spectroscopy (FT-IR) supported the XRD analysis and scanning electron microscopy (SEM) indicated the formation of particles in flat block shapes. Energy-dispersive X-ray spectroscopy (EDS) confirmed the high purity of the ceramic samples. The thermal conductivity changes induced by Y and Sr dopants were attributed to alterations in Ti-O bond distances and bond strengths. UV-vis spectroscopy identified a decrease in the optical band gap due to oxygen vacancies and lattice distortions. Mechanical strength analysis revealed a correlation between dopant content and compressive strength, with undoped $BaTiO_3$ exhibiting the highest strength. Additionally, dense BST-Cux ceramic composites were fabricated using spark plasma sintering, demonstrating enhanced AC conductivity with increasing Cu content and temperature. Electrical conductivity mechanisms shifted from oxygen vacancy migration to band conduction, and dielectric behavior varied based on phase ratio, with composites displaying elevated permittivity at low frequencies. These findings provide insights into the defect structure and thermoelectric behavior of doped $BaTiO_3$ ceramics, contributing to their potential applications in micro-optical electro-mechanical systems and the multilayer ceramic capacitor (MLCC) industry.

Introduction

Barium titanate (BT) is a type of material that is often used in the electrical and electronic industries due to its various desirable properties, such as its ability to exhibit ferroelectricity, pyroelectricity, and piezoelectricity, as well as having a high dielectric permittivity and a positive temperature coefficient of resistivity. It is abbreviated as BT and is written as $BaTiO_3$ in chemical notation [1], [2]. Perovskite materials that are derived from barium titanate have a wide range of applications, including use in devices that have a positive temperature coefficient, devices that generate pulses, infrared detectors, microwave electronics that can be voltage-tuned, multilayer ceramic capacitors, piezoelectric and ultrasonic actuators, thermal sensors and controllers, and microwave devices that utilize piezoelectric transducers and charge storage devices[3-5] and so forth. To produce multilayer ceramic capacitors (MLCCs) using BT material, the formulation of the BT must be carefully designed to control its electrical properties, particularly at high temperatures and under high electric fields [6]. To improve the reliability of multilayer ceramic capacitors (MLCCs) made with BT, various additives and dopants, such as yttria (Y_2O_3), are substituted to the $BaTiO_3$.

Yttrium (Y) is added to barium titanate to improve the reliability of multilayer ceramic capacitors. The Y^{3+} ion has an ionic radius that is intermediate in size between the Ba^{2+} and Ti^{4+} ions, which allows it to occupy either the Ba^{2+} or Ti^{4+} site in the BT lattice [7]. This means that the Y^{3+} ion can act as an acceptor or donor depending on its position in the lattice, and its inclusion in the BT structure is influenced by kinetic and thermodynamic factors [8], [9]. It is reported that the formation energy of $Y_{\dot{B}a} + V_{Ba}''$is 7.23 eV whereas it is only 4.35 eV to form a $Y_{\dot{B}a} + V_{Ba}'''$ defect [10]. The oxygen partial pressure and sintering temperature can create vacancies in the BT lattice for the Ba^{2+} or Ti^{4+} ions. These vacancies can then be filled by Y^{3+} ions, which may occupy either both or one of the sites [11]. The solubility of yttrium ions in the BT lattice, and therefore their ability to occupy the vacancies created by the Ba^{2+} or Ti^{4+} ions, is influenced by the Ba/Ti ratio, the dopant concentration, and its solubility. The solubility of Y ions can vary depending on whether they are occupying the Ba-site or the Ti-site in the lattice. According to a study by Wang et al. [12], the solubility of Y^{3+} ions in the BT lattice can vary depending on the sintering conditions and the site in the lattice that the ions are occupying. For example, the solubility of Y^{3+} ions at the Ba-site is approximately 1.5% when sintered in air at 1440-1470°C, but it increases to 4% when sintered under reducing conditions. The solubility of Y^{3+} ions at the Ti-site is higher, at approximately 12.2% when sintered in air at 1515 °C. In addition, the introduction of Y^{3+} ions into the BT lattice can cause structural changes, such as a phase transformation from tetragonal to cubic. The amount of yttrium ions added to BT can be consumed by various processes during the processing of the ceramic material. A study by Belous et al.[13] found that the dopant could be consumed in processes such as the exchange of paramagnetic impurities that occupy Ti-sites, charge compensation mechanisms, and the formation of secondary phases such as $Ba_6Ti_{17}O_{40}$ and $Y_2Ti_2O_7$. These secondary phases can form when the solid solubility of the dopant in the BT is exceeded. The yttrium ions can also influence the charge compensation mechanisms in the BT lattice [14-16].

It is possible to improve the structural, optical, and thermoelectric properties of a barium titanate system by adding the appropriate amount of dopants [14], [15]. The formation of secondary phases such as $Ba_2TiSi_2O_8$, $Ba_6Ti_{17}O_{40}$, Y_2TiO_5, and pyrochlore-type phases like

$R_2Ti_2O_7$ (where R is a rare-earth element such as Dy, Er, Ho, or Y) [16-18] has been observed when barium titanate is doped with rare-earth elements [19]. These secondary phases are usually formed when the amount of dopant exceeds its solubility limit in the BT lattice and reacts with other free ions in the system, like Ti^{4+}. The formation of these phases depends on factors such as the sintering conditions and the concentration of the dopant. The presence of these secondary phases can adversely affect the structural and dielectric properties of BT, which is of concern for industrial applications. Among the pyrochlore-type phases that have been reported, $Y_2Ti_2O_7$ has been suspected to have a negative impact on the reliability of barium titanate (BT)-based MLCCs [20], [21]. This phase is believed to have a highly conductive nature and to cause resistance degradation in BT through the acceleration of oxygen vacancy electromigration [22]. The effects of $Y_2Ti_2O_7$ and other secondary phases on the structural and dielectric properties of BT are of high interest for industrial applications, as several studies have reported negative impacts on the major properties of BT [21], [22]. The investigation of the parameters that influence the formation of $Y_2Ti_2O_7$ and its potential effects on BT is of interest in both the academic and industrial fields, as Y_2O_3 is a commonly used dopant in the production of MLCCs.

The electrical conductivity of a material can be measured to study the properties related to defects in non-stoichiometric compounds [23]. The advantage of measuring electrical conductivity is that it allows us to examine the properties of materials at high temperatures and monitor these properties during the materials' processing. However, interpreting electrical conductivity data, especially for polycrystalline materials, can be difficult due to the complexity of the physical sense of electrical conductivity.

Thermal management is important for ensuring the reliability and integrity of electronics in a variety of applications. To optimize the performance and device design of electronics in challenging thermal environments, it is essential to understand the thermal properties of barium titanate. These properties, including thermal conductivity and heat capacity, play a significant role in the design and efficiency of many applications, particularly in thermal management in the optoelectronic industries and phase transition materials (PCMs) [24], [25]. In addition, evaluating the mechanical properties, such as compressive strength of MLCCs is necessary to understand the internal stresses imposed on the MLCCs [26] and to extend their lifetime. $BaTiO_3$ has also been used in a range of electro-optic systems due to its excellent optical characteristics, including highly sensitive photodetectors, second harmonic generators, light sensors, and optical signal processing [27], [28]. By altering the content of yttrium (Y) in $Ba_{1-x}Y_xTiO_3$ ceramic materials, it is possible to modify the physical characteristics and energy band gap of the material, potentially expanding its potential technological applications. Several methods have been used to synthesize $BaTiO_3$ for electrical device applications, including conventional solid-state reaction, hydrothermal technique, and co-precipitation. However, the sol-gel method is particularly useful for fabricating new compositions because it allows for control of the stoichiometry and homogeneity of the material and can be performed at lower temperatures using simple laboratory equipment. In this report, sol-gel method was used to prepare yttrium-doped $BaTiO_3$ at different doping concentrations and sintered the materials in air. The resulting materials were analysed to study the structural, microstructural, thermoelectrical, and optical properties, with a focus on the stoichiometric ratio of $BaTiO_3$ and its semiconducting nature in relation to its use in multilayer ceramic capacitors.

Since ceramics are brittle, a variety of approaches to enhance their fracture resistance, compressive strength and optical properties have been reported. Recently, novel composite materials that exhibit excellent functional as well as mechanical properties have been developed for advanced engineering applications. Among them, ceramic matrix composites with ferroelectric/piezoelectric secondary dispersoids have been proposed. The electromechanical properties of ferroelectric/piezoelectric phases induced interesting functions in the composites. By utilizing the electromechanical properties of the ferroelectric material, it is possible to detect crack propagation. When an electric field is applied to the ferroelectric materials, anisotropic internal stresses induced can increase or decrease fracture toughness, depending on the poling direction. Ferroelectric particles dispersed in the ceramic matrix composite are expected to exhibit such smart functions that can predict the fracture, which electric signal can be detected during crack propagation, and controlling the crack.

In the past few years, Komandin and his colleagues have proposed a ferroelectric nanocomposite with high strength and toughness such as PZT/Pt [32] and $BaTiO_3$/SiC [33] and many researchers have extensively investigated its excellent mechanical properties and also in such electrical properties as dielectric constant, the Curie temperature, and so on. Various compositions such as $BaTiO_3/Al_2O_3$[34], $BaTiO_3$/3Y–TZP [35], and $BaTiO_3/ZrO_2$ [36] composites have been studied. High fracture toughness has been recently achieved for a $BaTiO_3$ toughened Al_2O_3 system [34]where the fracture toughness reached 5.1 MPa $m^{1/2}$ for a composition of 5 mol% $BaTiO_3$ in Al_2O_3 matrix composites, while that of a monolithic Al_2O_3 is around 4 MPa $m^{1/2}$.

Barium strontium titanate BST still attracts much attention due to its unique properties, such as high tunable dielectric constant, low dielectric loss, and low dielectric relaxation time [18], [37]which are promising in the application as microwave resonators, phase shifters, pyroelectric sensors, and capacitors [38], [39] It was known that either stress or oxygen content will affect the dielectric properties of BST significantly, i.e., the ability of simultaneously achieving both high tuning and high dielectric Q is limited by the strain, while the properties are detrimentally influenced by the oxygen vacancies. It is suggested that the introduction of metallic particles, such as silver, into the ceramics matrix, could relieve the internal stresses and depress the oxygen vacancy[40], and even result in the great enhancement of the dielectric constant about percolation threshold for thus metal/ceramics composites. In addition, it is believed that a rationally modified synthetic route can also be adapted for the preparation of $BaSrTiO_3$–Cu (BST-Cu) composite powders. Not only the development of a new synthetic route but also an advanced sintering method had to be adopted in order to obtain a microstructure with metallic inclusions of Cu homogeneously dispersed in an ultrafine ceramic matrix of BST. Much effort concerning the control of the size and distribution of metal nanoparticles has been undertaken in this context, but only micro composites have been reported so far. As mentioned above, it is believed that the realization of uniformly distributed metal particles within a ceramic matrix is a prerequisite for achieving good percolative ceramic–metal composites as a rather novel concept of dielectric materials. In this study, spark plasma sintering (SPS) has been carried out to successfully consolidate BST–Cu powders into composites preserving ultrafine microstructures. Because SPS offers the combined advantages of fast heating rates, the application of mechanical pressure, very short sintering times, and relatively low sintering temperatures, this technique provides an effective approach to promote densification and to reduce grain coarsening during sintering of nano or submicron-composite powders [41-44].

The motivation for this PhD work lies in the optimization of barium titanate (BT) based materials, particularly those doped with yttrium (Y) and strontium (Sr), to enhance their performance in multilayer ceramic capacitors (MLCCs) and other electronic applications. By delving into the intricate interactions between yttrium and strontium dopants and the BT lattice, the aim is to improve MLCC reliability by understanding and controlling the influence of dopants on material properties. Through experimental investigations, the focus is on elucidating the thermodynamic and kinetic factors governing dopant incorporation and solubility, ultimately enabling precise control over material properties. Additionally, this research endeavors to explore how yttrium and strontium doping influences the structural, optical, and thermoelectric properties of BT, employing advanced characterization techniques to analyze phase transformations and energy band gaps. Utilizing innovative synthesis methods such as the sol-gel process allows for the fabrication of yttrium and strontium-doped BT with tailored stoichiometry and homogeneity, while investigating novel composite materials incorporating BT aims to enhance mechanical, electrical, and optical properties, particularly through the integration of ferroelectric/piezoelectric secondary dispersoids to improve fracture resistance and electromechanical functionality. Furthermore, this work explores the synthesis of BT-based composites with metallic particles like copper, utilizing advanced sintering techniques such as spark plasma sintering (SPS) to preserve ultrafine microstructures and optimize composite performance. Through these endeavors, this PhD research contributes to advancing BT-based materials for various electronic applications, with a particular emphasis on enhancing MLCC reliability and performance.

1. Literature review and background of the research

1.1 Historical development

Perovskites obtain their name from the calcium titanium oxide ($CaTiO_3$) structure which was first discovered in the Ural Mountains of Russia by Gustav Rose in 1839 and is named after a Russian nobleman and mineralogist Count Lev Aleksevich Von Perovski (1792–1856)[32].

Generally, perovskites have the general formula ABO_3 where, A and B are two cations of very different sizes and O is an anion that bonds to both[33]. A large number of perovskite type oxides have been studied because of their interesting properties including superconductivity, insulator-metal transition, ionic conduction characteristics[34], dielectric properties and ferroelectricity[35]. Perovskite is one of the most frequently encountered structures in solid-state physics, and it accommodates most of the metal ions in the periodic table with a significant number of different anions. During the last few years, many experimental and theoretical investigations were devoted to the study of perovskite solids typically ABO_3.

The physicochemical properties of these materials are dependent on the crystal structure, lattice defect, exposed lattice plane, surface morphology, particle size, and specific surface area as well as the pore structure[36]. Up to now, a large number of perovskite-type oxides and perovskite-like oxides have been generated and investigated for clarifying their physicochemical properties.

Recently, perovskite structured ceramics have become one of the worldwide materials due to their peculiar properties viz. ferroelectric, thermo-electric, pyroelectric, dielectric and optical properties. Depending on these peculiar properties perovskite ceramics have several extraordinary applications such as random access memories, tunable microwave devices, capacitors, displays, piezoelectric devices, sensors, actuators, transducers and wireless communications [37].

1.2 Structure and stability of ABO_3 Perovskite

Perovskite structure have the general formula as ABO_3. The A site cation is slightly larger than B cation. The B atom has 6-fold co-ordination number and the A atom have 12-fold co-ordination number as shown in Fig.1. In general, Divalent A cations are 12-fold coordinated by oxygen anions and sits in corners of the cube at corner position (0, 0, 0). The tetravalent B cations lie within oxygen octahedral, occupies the body center position (½, ½, ½). The oxygen atoms are at the face center of the cubic lattice at position (½, ½, 0).

The prediction criteria for identification of formability of perovskite structure can be estimated by calculating tolerance factor (t) suggested by Goldschmidt as[38];

$$t = \frac{R_A + R_O}{\sqrt{2}(R_B + R_O)} \tag{1}$$

Where, R_A, R_B and R_O are the ionic radii of A, B and O ion respectively. Typically, the structures with t= 0.95 – 1.0 are cubic and the structures with t >1 is tetragonal [39]. There have also been reports of systems with t = 0.8 – 0.9 that do not take the perovskite form.

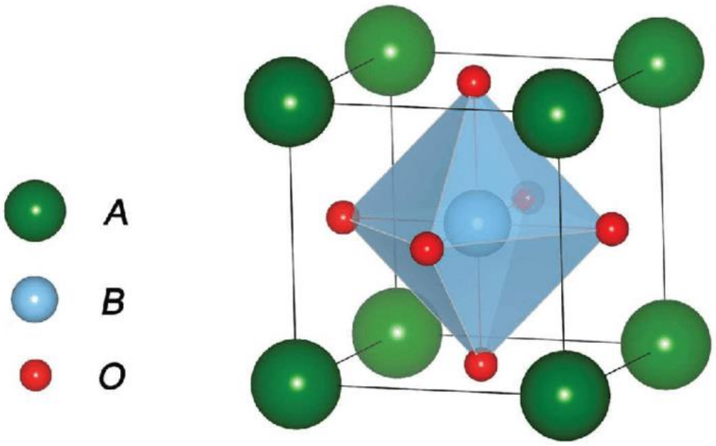

Figure 1. The ideal structure of ABO_3 perovskite compounds [40]

1.3 Electronic ceramics

The genesis of electronic ceramics can be traced back to the formative stages of the ceramic whitewares industry, where specialized electrical insulators first emerged. However, it was the exigencies of World War II, particularly the imperative for increasingly high-performance spark plugs in automotive and aircraft engines, that catalyzed significant advancements in this domain. Traditional porcelain substrates, ubiquitous in household applications and low-voltage insulation, underwent systematic refinement to meet the exacting demands of wartime technology. This pivotal juncture heralded the emergence of high-performance, molecularly engineered electronic ceramics. In contemporary contexts, high-technology ceramics represent integral constituents of electronic and electrical systems, permeating diverse sectors encompassing consumer electronics, industrial infrastructure, and military apparatus. Within the electronic domain, these ceramics assume pivotal roles in circuitry, facilitating a spectrum of functions spanning computational processing, signal modulation, telecommunications, and power distribution [37]. Despite their omnipresent utility, electronic ceramics often operate in a background capacity, quietly underpinning critical aspects of technological infrastructure.

1.4 Barium titanate ($BaTiO_3$)

The discovery of ferroelectricity in barium titanate ($BaTiO_3$) has given birth to many ABO_3 type materials. The diversity of structures exhibited by $BaTiO_3$ based perovskites, continues to fascinate in a range of areas including solid state chemistry, physics, and the earth sciences [40].
Its simplest structure is cubic, which is the high temperature form for many mixed oxides of the ABO_3 type. The simple cubic structure (space symmetry Pm-3m) consists of corner sharing oxygen octahedra (BO_6) arranged in three dimensions with smaller, highly charged cations (B: Ti^{4+}, Zr^{4+}, Sn^{4+}, Nb^{5+}, Ta^{5+}, W^{6+}, etc.) located in the middle of the octahedra, and lower charged, larger cations (A: Na^{+}, K^{+}, Ca^{2+}, Ba^{2+}, Pb^{2+}, etc.) in between the octahedra. The perovskite and crystal structure of $BaTiO_3$ are shown in Fig.2.1 most perovskite-type ferroelectrics are compounds with either $A^{2+}B^{4+}O_3^{2-}$ or $A^{1+}B^{5+}O_3^{2-}$ type formula.

$BaTiO_3$ is a white solid and typical ABO_3 perovskite-type material. It has four kinds of crystal systems: hexagonal, cubic, tetragonal, orthorhombic and rhombohedral, depending on the phase transition temperature [41]. The basic crystalline structure of $BaTiO_3$ at above 130°C is the ideal cubic perovskite structure. Below Curie temperature $BaTiO_3$ is tetragonal. When the temperature is decreased further, the structure of $BaTiO_3$ gradually changes from tetragonal to orthorhombic, and finally to rhombohedral. In the cubic perovskite phase, the barium and oxygen ions together form a face-centered cubic lattice (fcc), with titanium ions positioned on octahedral interstices.

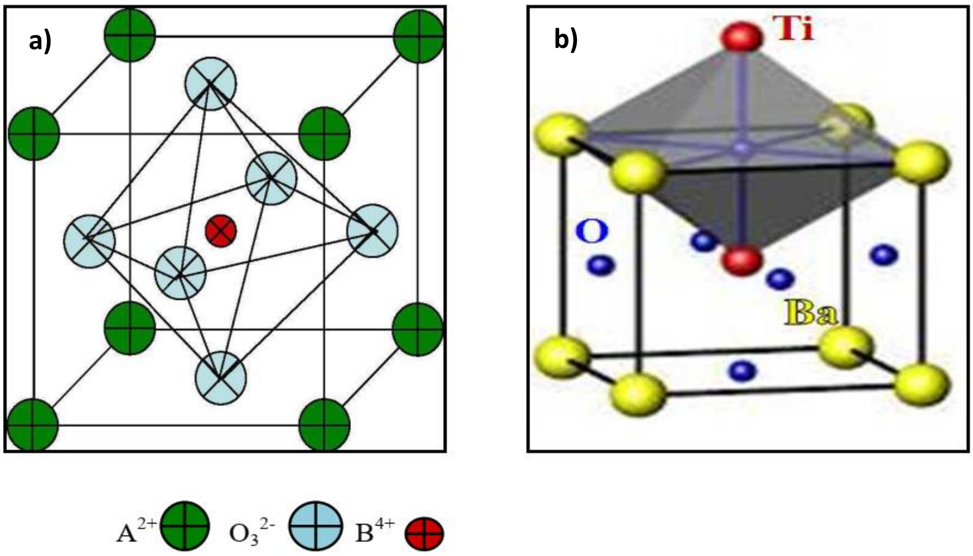

Figure 2. a) Perovskite Structure and b) Crystal Structure of $BaTiO_3$ [42]

Habib et al [41] finds the influence of temperature, aging time and particle size of titania precursor on the hydrothermal crystallization of $BaTiO_3$ and the morphological changes occurring during the formation of $BaTiO_3$ [41]. Hung et al adopted the sol–gel process along with the addition of a surfactant in order to get controlled sized and well-dispersed $BaTiO_3$ nanopowders [42].

1.5 Synthesis of $BaTiO_3$

Various methods have been employed to prepare $BaTiO_3$ materials, each with its unique advantages and applications. These methods include the molten salt method [43], sputtering [44], hydrothermal [45], solvo-thermal [46], which involve the use of both solvent and heat to drive chemical reactions, and sol-gel [47], where a solution precursor undergoes hydrolysis and condensation reactions to form a gel that can be further processed into desired forms. Amongst these methods, hydrothermal and sol-gel routes stand out as the most extensively employed for synthesizing $BaTiO_3$ nanoparticles. The hydrothermal method, leveraging aqueous solutions under controlled temperature and pressure conditions, offers superior crystallinity and phase purity even at relatively low temperatures. Similarly, sol-gel synthesis provides a versatile approach for tailoring the properties of $BaTiO_3$ nanoparticles, facilitating precise control over composition, particle size, and morphology. These methods collectively enable the production of $BaTiO_3$ nanoparticles with a highly crystalline structure and pure phases, essential for various technological applications.

1.6 Doping Barium titanate ceramics

The intentional introduction of impurities into a host lattice is the process known as doping [48] leading to novel phenomena very different from the precursor materials. Bulk semiconductors are successfully doped to build functional devices, and imparted by new electrical, optical, mechanical, and magnetic properties [49], [50]. crystalline semiconductors with unusual size-dependent optical and electronic behavior, however, are already marketed for applications as wavelength-tunable lasers, optical gain devices, bioimaging and solar cells [49]. Because their electronic states are confined to a small volume, doping nanocrystals results in phenomena not found in bulk materials.

Doping $BaTiO_3$ ceramics is of great importance in the fabrication of electric and electronic devices, and a large number of different dopants can be accommodated in the $BaTiO_3$ lattice. The ionic radius of dopants is the parameter which mainly determines the substitution site. For ions of the first series of the transition metals, like Cr^{3+}, Mn^{2+}, Mn^{3+}, Fe^{3+}, Co^{3+} and Ni^{2+}, it is well established that they preferentially substitute on the Ti^{4+} site.

1.6.1 Doping mechanism

The usual mechanism of charge compensation for the ions involves the creation of a stoichiometric amount of oxygen vacancies, so they behave as acceptor dopants [51]. Rare earth ions such as La^{3+} (1.15 Å) and Nd^{3+} (1.08 Å) are incorporated exclusively at the Ba^{2+} (1.42 Å) site, as their size is incompatible with that of Ti^{4+} (0.61 Å). These ions are known to act as donor dopants [52] . For the smaller lanthanide ions from Sm^{3+} to Lu^{3+}, the site occupied by the foreign cation is not exclusive. It is suggested that the ionic radius, dopant concentration, sintering atmosphere and Ba/Ti molar ratio all play crucial roles [52].

The properties of $BaTiO_3$ can thus be modified through the incorporation with various ions. One of the important applications is the change in the magnitude and character of electrical conductivity induced by appropriate dopants, which leads to semiconducting behavior of $BaTiO_3$ which is an insulator at room temperature. For instance, donor doping $BaTiO_3$ nanocrystals with trivalent ions (e.g., Y^{3+}, La^{3+}, Nd^{3+}, Sm^{3+}) causes an anomalous increase in electrical resistivity, known as the positive temperature coefficient of resistivity (PTCR) effect [53]. In this regard, electronic compensation is believed to be responsible for the PTCR effect, where reduction of a corresponding number of Ti^{4+} to Ti^{3+} ions occur and the reduced Ti^{3+} ions provide the source of semiconductivity [54]. The effect of a specific dopant on the mechanical and thermal conductivity of $BaTiO_3$ strongly depends on the substitution site, grain size, doping concentration, and defects [52].

1.7 Current research on $Ba_{1-x}Sr_xTiO_3$ in past five years

W. Q Cao et al [55] prepared the barium titanate powders by wet chemical route method. The surface composition of ceramic powders prepared via the low temperature Aqueous Synthesis, with formula $Ba_{1-x}Sr_xTiO_3$ (x=0-1), have been investigated. They measured the total relative amount of carbonate by X-ray diffraction and compared to that present on surface. The influence of Sr on the crystal structure, microstructure, and thermal expansion of $Ba_{0.98}Sr_{0.02}Ti_{1-x}Mn_xO_3$ ceramics ($0\leq x\leq 0.02$) was investigated by H.T Langhammer et al [56]. Compared to Sr "free" samples the transition region between tetragonal and hexagonal phase shifting was observed for higher concentrations of Mn. They used the Goldschmidt tolerance factor to discuss the stabilization of the tetragonal phase by the Sr impurity.

Sol–gel synthesis of $Ba_{1-x}Sr_xTiO_3$ (x=0.1, 0.2) ceramic fibers with a diameter of 6–10 µm using catechol-complexed titanium isopropoxide, barium acetate hydrate and strontium acetate hydrate as precursors has been investigated by M. Shandilya et al [57]. They studied the Microstructural development of barium strontium titanate ($Ba_{1-x}Sr_xTiO_3$) ceramic fibers as a function of strontium concentrations. From X-ray diffraction a well-developed cubic phase of (Ba, Sr) TiO_3 was noted at 1100 °C. N.P Bhagya et al [58] studied the Eu^{3+} doped BST (65:35), and BST (80:20) at different compositional ratios of $BaTiO_3$, $SrTiO_3$ and Eu_2O_3. Both structural and microsurface analyses were done using X-ray diffraction and scanning electron microscopy, respectively. At room temperature they investigated the photoluminescence properties of doped samples.

A. Karaphun et al [59] studied the $Ba_{0.6}Sr_{0.4}TiO_3$ (BST) nanopowders preparation by using the modified citrate method with ammonium nitrate as a combustion promoter, and the formation mechanism, phase evolution, and particle size have been investigated using TG/DTA, XRD, and SEM. E. Hajisaeid et al [60] discussed the ceramic–polymer composites. The samples were fabricated from barium strontium titanate powder (BST) and polypropylene-graft-poly (styrene-stat-divinylbenzene) (ER) using a twinscrew extruder.

P. Khirade et al [61] reported a simple, economic and low-temperature green combustion synthesis of $Ba_{1-x}Sr_xTiO_3$ (BST) ceramic nanopowders for composition x = 0.0, 0.2, 0.4, 0.6, 0.8 and 1.0 with lemon juice as a firing agent. The samples were prepared by sol-gel combustion method. The fabricated nanopowders were characterized by TGA/DSC, XRD, FT-IR, FESEM, TEM etc. analytical techniques. XRD analysis reveals the formation of single-phasic tetragonal perovskite structure with no impurity phases for x = 0.0 to 0.2 samples. However, cubic phase was appeared for x = 0.4 to 1.0 samples. The saturation electric polarization (Ps), remanence polarization (Pr) and coercive field (Ec) decreases with increase in Sr^{2+} content expected to be dependent on the creation of oxygen vacancies and occurrence of cubic polymorphs by doping of Sr^{2+} ions. They studied the effects of Sr^{2+} ions on $BaTiO_3$ properties, where, the Sr^{2+}-substitution has brought an overall enhancement in dielectric and electrical properties. However, the ferroelectric characteristics are weakened, which is primarily attributed to a considerable variation in the micro-structure of the solid.

M. Arshad et al [62] discussed lead-free strontium-doped ferroelectric ceramics with the compositional formula $Ba_{1-x}Sr_xTiO_3$ (barium strontium titanate, BST) at (x = 0, 0.25, 0.3, and 0.35) synthesized using a solid-state reaction. Their samples samples are characterized by X-ray diffraction (XRD) and Raman spectroscopy. Further dielectric properties and impedance are examined. The analysis from XRD and Raman spectrum studies revealed that the lattice constant, unit cell volume along with tetragonality ratio, Curie temperature (Tc), and dielectric constant along with dielectric loss factor decreased, which increased Sr^{2+} ions. Impedance spectroscopy revealed that relaxation behavior and obviously are responsible for conduction in the BST ceramic samples. Resistivity increased with the increase in Sr concentration. Activation energy of the grain boundary was higher than the grain, suggesting that the grain boundary has higher resistance. Ionic conduction in BST ceramics was considered for superior conduction. Lead-free and environment-friendly BST ceramics have the potential to be useful for multilayer chip capacitor and dynamic random-access memory.

G. Panomsuwan [63] prepared Barium strontium titanate ($Ba_{1-x}Sr_xTiO_3$, BSTO: x=0, 0.3 and 0.5) ceramics by sintering sol–gel derived BSTO powders at 1350 °C for 2 h. they found the average grain size of BSTO ceramics decreased from 15 to 2 μm with increasing Sr molar fraction. X-ray structural analysis revealed that BSTO ceramics exhibited tetragonal structure (x=0 and 0.3) and transformed into cubic structure at high Sr molar fraction (x=0.5) at room temperature. They found also the energy storage density of pure $BaTiO_3$ was about 0.2 J/cm3; however, energy storage efficiency was less than 50%. After doping with Sr molar fraction of 0.5, energy storage density decreased to 0.1 J/cm3 but its energy storage efficiency significantly improved to 90%.

1.8 Current research on $Ba_{1-x}Y_xTiO_3$

H. C. Padmini et al. [64] prepared $SrTiO_3$ by the solid-state reaction process and found that the thermal conductivity can be successfully decreased in dysprosium modified $SrTiO_3$ ceramic powders. H. Muta et al. [65] investigated the structural and thermoelectric properties of rare earth (Y, La, Sm, Gd, and Dy) modified $BaTiO_3$ and he examined the influence of the doping and the rising of the temperature on decreasing the thermal conductivity, indeed, the number of merits is enhanced by the difference in the thermal conductivity.

Z. Penk et al. described [66] the effects of preparation method on the phase formation behavior, dielectric and electric properties of $Ba_{1-x}Y_xTiO_3$ (x=0.15 and 0.85) ceramics. They found that when the $Ba_{1-x}Y_xTiO_3$ ceramics sintered at 1050 °C for 20 h, it showed more homogeneous microstructure, a higher dielectric constant (about 1.7×105), and a lower dielectric loss. The enhanced dielectric properties for $Ba_{1-x}Y_xTiO_3$ ceramics should be closely linked with the grain size. Moreover, the different microstructures between grain (nanodomain) and grain boundary were proposed to explain the enhanced dielectric properties.

E. Rosa Selva et al. [67] synthesized $Y_xBa_{1-x}TiO_3$ (YBT)(x=0, 4 and 8%) by solid-state reaction method as well as a 1:1 heterojunction with yttria-stabilized zirconia (BST08/YSZ). They characterized the obtained samples (BT, YBT04, YBT08 and YBT08/YSZ) using TGA/DTA, XRD and SEM-EDS analysis. Their results showed that samples calcined under reducing atmosphere presented a higher crystallinity degree, less amount of secondary phase of pyrochlore and greater limit of solubility for the Y dopant when compared to samples calcined under inert atmosphere. Doping was proved by the preferential peak shift, increase in micro strain, and decrease in lattice parameters and crystallite size. SEM micrographs showed an efficient sintering process with well-defined grain boundaries. The average grain size of the samples decreased proportionally with the amount of yttrium, showing that Y presents an inhibitory role in the grain growth process.

1.9 Current research on co-doped $BaTiO_3$

It is widely recognized that impurities significantly impact the major properties of $BaTiO_3$ ceramic material. Indeed, adequate ion doping or co-doping is considered an effective and useful technique to improve the structural, microstructural, optical, dialectical, and physical properties of BT. Similarly, the major characteristics of $BaTiO_3$ can easily be modified by doping a cation ion at the X -site and/ or Y -site. Typically, the ionic radius can be employed to predict the site occupation of various dopants, e.g., dopants with wide ionic radius and low valence are appropriate to occupy the X-site of Ba^{2+} (rBa^{2+}=1.35 Å) and dopants with high valence and smaller ionic radius are appropriate to occupy the Y-site of Ti^{4+} (rTi^{4+}=0.61 Å) [68]. The substitution site can also be defined X/Y ratio [69]. Moreover, the $BaTiO_3$ can be modified into the semiconductor material using some type of doping which changes the structure and grain size to use in optoelectronic applications [70]. Numerous studies have been performed on the production and investigation of doped BT with different substitutions such as Sr and Ca at Ba site [71], [72] and Fe, Mn, Sn, Zr, and Y at Ti site to enhance its major properties [73-77]. While La, Sr, Ca, Co, Fe, Mn, and Ni co-doping at both Ba and Ti sites has been carried out for piezoelectric, optical, and magnetic properties of $BaTiO_3$ [78-81]. Besides that, recently, Sr^{2+} and Y^{3+} modified BT materials have received much interest as technologically crucial lead-free ferroelectric materials [71-87]. Nevertheless, to the best of our knowledge, no similar studies were dedicated to the investigation of the optical, thermal conductivity, and compressive strength of Sr and Y co-doped $BaTiO_3$ using the sol-gel method.

Table 1. Effect of doping on some properties of $BaTiO_3$

Material	Synthesis method	Calcination temperature (°C)	Structure	Band gap (eV)	Thermal conductivity (W.m^{-}1. K^{-1})	Ref.
$BaTiO_3$	Solid-state reaction	1100, 4h	Tetragonal	3.30	2.26	[88]
$Ba_{0.99}Bi_{0.01}TiO_3$	Sol-gel	800, 3h	Tetragonal	3.00	-	[89]
$Ba_{0.75}Sr_{0.15}TiO_3$	Sol-gel	950, 3h	Tetragonal	-	3.72	[15]
$BaTi_{0.8}Fe_{0.2}O_3$	sol-gel auto combustion	900, 2h	Tetragonal	3.11	-	[90]
$BaTi_{0.72}Y_{0.28}O_3$	Sol-gel	1050sc, 3h	Tetragonal	2.87	1.97	[91]
$BaTi_{0.985}Co_{0.005}Nb_{0.01}O_3$	Solid-state reaction	1100,5h	Hexagonal	2.98	-	[78]

1.10 Ceramic-Metal composites

Ceramic metal composites, or CMCs, combine ceramic phases with light metals to enhance properties and reduce costs. They offer higher strength, stiffness, hardness, wear resistance, and lower thermal expansion. Despite challenges like processing costs and reduced ductility, recent advances show promise. These composites address ceramic brittleness by incorporating ductile reinforcements like particles and fibers. Ongoing research aims to improve fracture toughness and reliability. CMCs represent significant progress in material science. Ceramic metal composites combine ceramic and metal phases to enhance material properties and reduce processing costs. These composites offer improved strength, stiffness, hardness, wear resistance, and reduced thermal expansion coefficients. Recent advancements include exploring continuous phases for an interpenetrating microstructure, addressing ceramic brittleness by incorporating ductile reinforcement morphologies. Despite their potential, ceramics lack plastic deformation at ambient temperatures, leading to lower fracture toughness compared to metals. Research focuses on enhancing fracture toughness and in-service reliability by minimizing flaws. Composite materials like MMCs and ceramic–matrix composites (CMCs) represent significant advancements, with interpenetrating composites offering unique structural advantages.

CMCs have been under investigation for more than 30 years with some successful commercial applications emerging with enhanced material properties and reduction in processing costs summarized e.g., by Zhi Ye [92] and by the authors [93], [94] Inclusions of a ceramic phase are used in light metals like aluminum and magnesium to achieve higher strength, stiffness, hardness, wear resistance and reduced coefficient of thermal expansion. The main drawback of the material has been the high costs associated with the processing and the loss of ductility of the material. It is interesting to see the subject matters from both sides, as the closely related ceramic matrix composites (CMCs) incorporate metal phases to increase the toughness of the brittle ceramic matrix that also have been investigated [95] thoroughly. Traditionally, the continuous phase of the composite has been designated as the matrix. More recently, interest has arisen in composites where both phases are continuous, resulting in an interpenetrating microstructure [96]. One method to achieve such a microstructure is the infiltration of molten metal into a porous ceramic body called a preform. Moreover, the concept of ductile-phase toughening of brittle materials [97] has been widely used in composites with different ductile reinforcement morphologies, such as particles, fibers, and laminates. However, for the same volume fraction of the ductile reinforcing phase, the ductile phase in laminate form has the maximum toughening efficiency, followed (in order of potency) by fiber and particulate morphologies [98].

In contrast to metals, which can exhibit plastic deformation before fracture due to the high mobility of dislocations, ceramics do not show plasticity at ambient temperatures. Owing to plastic deformation, the fracture process in metals involves extensive energy dissipation. The absence of such energy dissipating phenomenon in ceramics results in their relatively low fracture toughness and leads them to fail catastrophically under mechanical and thermal loading. For instance, the values of fracture toughness for Al_2O_3 or Si_3N_4 ceramics are 3–5 and 3–6 MPa $m^{1/2}$ respectively. In comparison, the fracture toughness values of pure metals such as Al, Cu, or Ni may reach 100–150 MPa $m^{1/2}$. In practice, it means that ceramics are very sensitive to the presence, distribution, and size of flaws such as cracks, pores, inclusions, etc. For that reason, over the last 30 years, one of the major scientific and technological efforts of ceramic research in the field of structural ceramics has been directed toward improving (i) the fracture toughness by activating a variety of energy-dissipating phenomena in the fracture process, i.e. imparting them a damage tolerant behavior, and (ii) the in-service reliability of ceramics by decreasing the flaw size and by increasing the homogeneity of their distribution. Despite the tremendous progress that has been made in the understanding and development of monolithic materials with improved properties, composite materials that successfully combine the advantageous properties of individual components represent a breakthrough in that direction. Depending on the nature of the base material, one must distinguish between metal–matrix composites (MMC) and ceramic–matrix composites (CMC). Recently, interest has arisen in interpenetrating composites (IPCs) [99]. Contrary to conventional particulate or fiber-reinforced ceramic or metal/intermetallic matrixes, the IPCs consist of co-continuous 3D interpenetrating networks of ceramic and metal/intermetallic phases, resulting in an interpenetrating microstructure.

1.11 Spark plasma sintering (SPS)

Spark plasma sintering (SPS) is a rapid and efficient method for fabricating bulk materials from powders, offering fast heating, short holding times, and lower sintering temperatures compared to conventional techniques. It's particularly useful for processing challenging materials like nanostructured materials, composites, and refractory metals. However, further research is needed to fully understand its mechanisms, including the controversial role of spark plasma and discharge during the process. SPS, also known as the field-activated sintering technique and pulsed electric current sintering, is a comparatively novel sintering process that allows the fabrication of bulk materials from powders using a fast heating rate (up to 1000 °C min^{-1}) and short holding times (in most cases 0–15 min) at low sintering temperatures (200–300 °C lower than most conventional sintering techniques) [100-103]. Because of its great advantages, SPS is by far the most popular of the ultrarapid sintering techniques and is used to process nanostructured materials, amorphous materials, intermetallic compounds, metal matrix and ceramic matrix composites, highly refractory metals, and ceramics, etc., which are difficult to sinter by common methods [104-106].

Extensive efforts have been made in investigating SPS and developing it as a promising technique for the rapid densification of advanced new materials with various applications [107-109]. However, limited data are available on the sintering mechanism involved in the SPS process. In addition, a significant gap exists in the fundamental understanding of the SPS mechanisms. This gap is due to the complexity of the thermal, electrical, and mechanical processes that may be involved during SPS, in addition to their dependence on the SPS parameters. In particular, the existence of spark plasma and the occurrence of discharge in the sintering process are highly controversial.

Scholarly discourse commonly acknowledges that during the SPS process, a high electric–pulsed current is applied to the electrodes (as shown in Figure 3), and the microscopic electrical discharges in the gaps between the powder particles generate plasma, causing sintering [110]. The spark discharge can effectively eliminate adsorptive gas and any impurities present on the surface of the powder particles and can easily destroy the oxide films on the particle surface, leading to an enhancement of the thermal diffusion ability of the sintered material [110]. In addition, Joule heating and plastic deformation effects contribute to the densification of the powders.

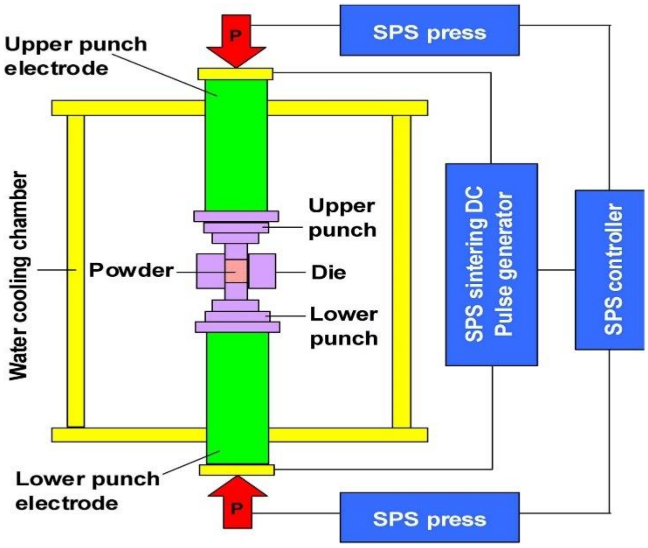

Figure 3. A schematic of the SPS process [110].

1.12 Knowledge gap

The literature review reveals a significant body of work on doped barium titanate synthesis and applications. However, the impact of dopants (Sr, Y) on $BaTiO_3$ composites, particularly on mechanical and thermoelectrical properties, remains unexplored. The sol-gel method, known for precise stoichiometry control, has not been extensively employed at lower temperatures using simple equipment for these investigations. Moreover, no studies have addressed the comparative influence of strontium and yttrium co-doping on the structural, microstructural, compressive strength, thermoelectrical, and optical properties of $BaTiO_3$ composites. This gap necessitates a comprehensive analysis focusing on major properties, emphasizing the stoichiometric ratio of $BaTiO_3$ and its semiconducting nature, especially concerning its application in multilayer ceramic capacitors (MLCCs). Additionally, the recent surge in interest surrounding ceramic-metal composites, due to enhanced permittivity and thermal conductivity near the percolation threshold, lacks detailed investigations into their electrical and thermal conductivity. Despite widespread studies on colossal permittivity in these composites, there is a notable absence of reports on the synthesis and spark plasma sintering of $Ba_{0.85}Sr_{0.15}TiO_3$-Cu composite powders, with no dedicated publication on the electrical, dielectric, and thermal properties of $Ba_{0.85}Sr_{0.15}TiO_3$-Cu ceramic composites. Closing these gaps is crucial for advancing our understanding of these materials and unlocking their potential applications.

1.13. Objectives

The primary objectives of this study are as follows:

1. Structural, Optical, and Thermoelectric Enhancement of BSrxT Ceramics:
    - Produce BSrxT ceramics with varying Sr concentrations (x=0, 5, 12.5, 15, 20, and 30%) using the sol-gel method.
    - Investigate the effects of Sr concentration on lattice parameters, crystalline phase, and microstructure through X-ray diffraction (XRD) and scanning electron microscopy (SEM).
    - Analyze compositional stoichiometry using energy dispersive spectrum (EDS) analysis.
    - Evaluate compressive strength properties as a function of Sr content and grain size.
    - Study thermal conductivity at room temperature.
2. Yttrium-Doped $BaTiO_3$ for Multilayer Ceramic Capacitors (MLCCs):
    - Prepare yttrium doped $BaTiO_3$ with various doping concentrations and sinter the materials in air.
    - Investigate structural, microstructural, thermoelectric, and optical properties, with a focus on stoichiometric ratio and semiconducting nature for MLCC applications.
3. Sr and Y Doped and Co-Doped $BaTiO_3$ Ceramics:
    - Utilize sol-gel technique to prepare BSrxT ceramics with formulas $BaTiO_3$, $B_{1-x}Sr_xTiO_3$, $Ba_{1-x}Y_xTiO_3$, $BaT_{1-x}Y_xO_3$, $Ba_{1-x}Y_xTi_{1-x}Y_xO_3$, and $Ba_{1-x}Sr_xTi_{1-x}Y_xO_3$ (x=0.075).
    - Investigate influences of Sr^{2+} and Y^{3+} ions on phase structure, lattice constants, and microstructure using XRD and SEM.
    - Identify compositional stoichiometry with EDS analysis.
    - Examine optical behavior through UV-visible spectroscopy.
    - Analyze compressive strength properties as functions of Sr and Y concentrations and grain size distribution.
    - Investigate thermal conductivity as a function of temperature.
4. Enhanced Electrical Properties with Copper Incorporation:
    - Incorporate copper metal as reinforcement within the BST ceramic matrix to enhance electrical properties.
    - Evaluate the composite's characteristics as an innovative electrical material with applications in optoelectronics, microelectronics, and spintronics devices.

2. Experimental Techniques

Synthesis of samples is an imperative task, and it can be solved by various synthesis techniques. Synthesis of the nanocrystalline ceramics is one of the most vital and rapidly growing areas of research in the field of nanotechnology. As the bulk material come near to nanoscale its properties drastically change. These properties are attributed to the size, shape, and distribution of the particles in the materials, which in turn depend on the method of synthesis. The methods of synthesis play a very important role about structural, physical, and chemical properties of perovskite. structured materials. In this thesis, the ceramics $Ba_{1-x}SrTiO_3$ and $Ba_{1-x}Y_xO_3$ were synthesized using sol-gel technique. The detailed synthesis procedure is specified in this chapter.

2.1. Synthesis of $Ba_{1-x}Sr_xTiO_3$ ceramics

The pure and Sr-modified $BaTiO_3$ powders were prepared through the sol-gel method [89], [114] using Barium acetate trihydrate ($Ba (CH_3CO_2)_2.3H_2O$) (99,9% purity), Strontium acetate ($C_4H_6O_4Sr$) (99% purity) and Titanium alkoxide $Ti [OCH(CH_3)_2]_4$(97%, purity) as primary precursors, while introducing lactic acid and acetic acid as pivotal stabilizing agents, a strategic evolution inspired by recent investigations into solution chemistry optimization. The process commences with the dissolution of titanium isopropoxide in a precisely calibrated mixture of water and acetic acid, maintaining a delicate equilibrium at 70°C while employing a novel agitation mechanism operating at 300rpm, a nuanced refinement inspired by computational modeling insights into fluid dynamics [122], [123]. Generally, the raw materials used in the sol-gel process were metal alkoxides and acetates. The specification of raw materials is given in Table 2.

Table 2. Specification of chemicals used in sol-gel experiments.

Chemical	Chemical formula	Company	Purity (%)
Barium acetate	$(CH_3COO)_2Ba$	Sigma–Aldrich	≥99.00
Strontium acetate	$(CH3COO)_2Sr$	Sigma–Aldrich	≥99.00
Yttrium acetate	$C_6H_{11}O_7Y$	Sigma–Aldrich	≥99.00
Titanium (IV) isopropoxide	$Ti [OCH(CH_3)_2]_4$	Sigma–Aldrich	≥97.00
Acetic acid	CH3COOH	Sigma–Aldrich	≥99.50
Acetyl–acetone	$CH_3COCH_2COCH_3$	Sigma–Aldrich	≥99.30
Distilled water	H_2O	Sigma–Aldrich	

Different processing steps were followed for the synthesis of Sr-modified Barium titanate ceramics with composition ($Ba_{1-x}Sr_xTiO_3$, x = 0, 5, 12.5, 15, 20 and 30%) as shown in Figure 4. The first step consists of the preparation of a clear solution of Barium and Strontium acetates, the preparation of 100ml of Barium and Strontium acetates at 1 M/L, requires; 25.54g of the latter, distilled water, and a few drops of acetic acid (0.25ml), the obtained mixture is subjected to continuous stirring at 80 °C until a very transparent (clean) solution is obtained. The final solution is adjusted with distilled water (Solution A). The second step is to prepare a colloidal solution of Titanium alkoxide TiO_2. The preparation of 500 ml of 1mol / l Titanium sol requires; 143.5g of Titanium alkoxide, 22.5g of lactic acid, and 300g of distilled water. A 1% excess of Titanium was added to the lactic acid solution to account for losses of Ti due to hydrolysis and the sol filtration operation. Introducing Titanium alkoxide into the lactic acid solution with stirring at 70 °C immediately gives a white milky precipitate. The obtained mixture, subjected to continuous stirring for about 24 hours, gradually passes from a white solution to a completely transparent sol (Solution B). The third step consists of mixing the obtained solutions (A and B). These solutions are mixed in stoichiometric proportions, according to the chemical formula $Ba_{1-x}Sr_xTiO_3$ (x = 0, 0.05, 0.125, 0.15, 0.2 and 0.3) with stirring for 5 min, to ensure the homogeneity of the final solution. The destabilization of this solution is ensured by the evaporation of the solvent in a programmable oven at the temperature of 80°C for 48h (Step 4). The obtained xerogel is ground in an agate mortar to break up the agglomerates of the powder and increase its responsiveness. The powders, after grinding, were calcined in the air in a programmable furnace at the temperature of 950°C for 3 h.

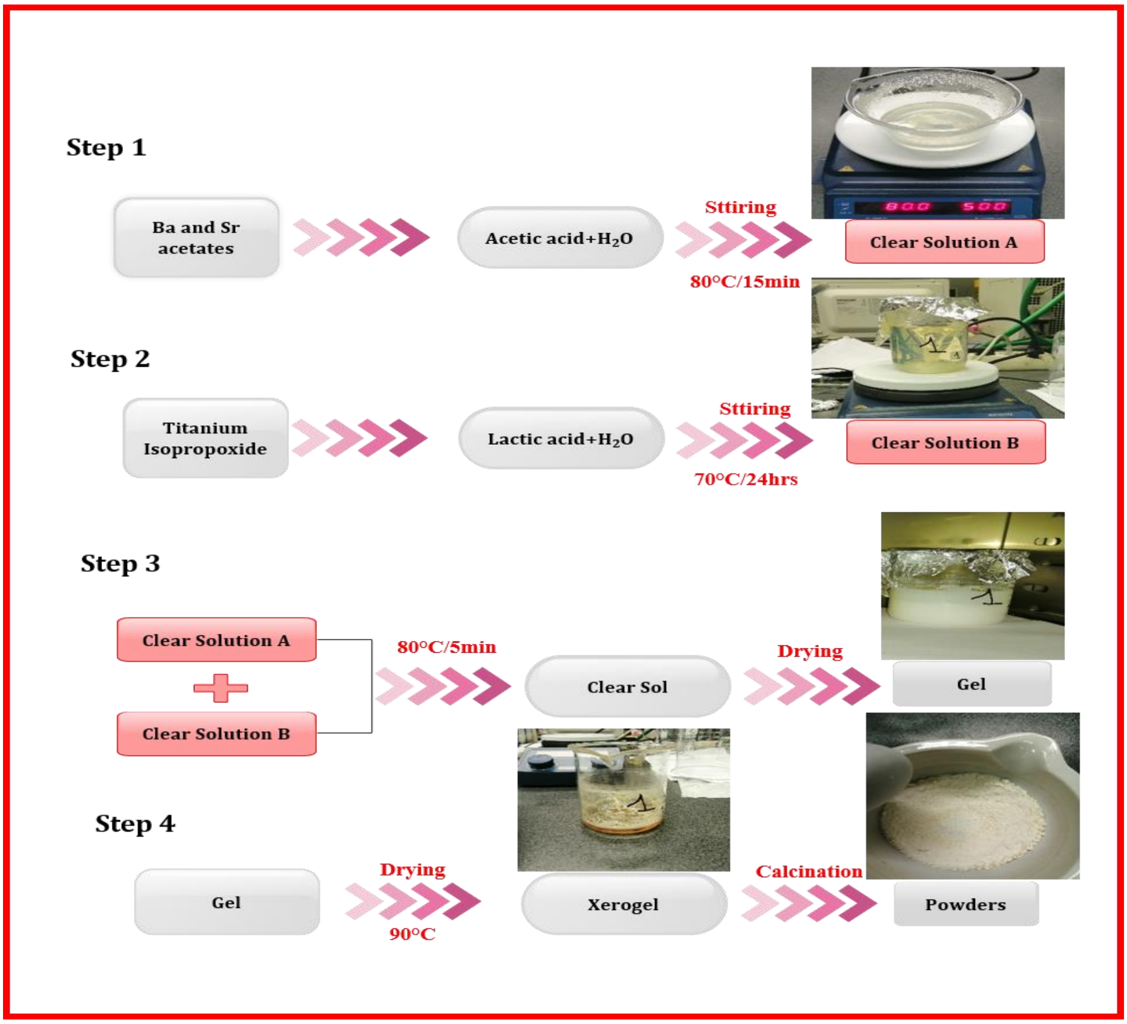

Figure 4. $Ba_{1-x}Sr_xTiO_3$ (x = 0.0–0.3) synthesis flowchart of the produced ceramic powders synthesized through sol-gel process

2.2. Synthesis of $Ba_{1-x}Y_xTiO_3$ ceramics

BYxT; x=0-30% ceramic samples were prepared via sol-gel method and outlined in Figure 5. The process involves using three precursors barium acetate trihydrate [Ba $(CH_3CO_2)_2.3H_2O$ ≥ 99% Aldrich], yttrium acetate hydrate III [$C_6H_{11}O_7Y$ ≥ 99% Aldrich], and titanium isopropoxide [$Ti(OCH(CH_3)_2)_4$]≥ 97% Aldrich]. Lactic acid (CH_3CH (OH) CO_2H) and Acetic acid CH_3COOH were used as a stabilizing agent, while distilled water was employed as a substance for dissolving the barium and yttrium acetates. The first step involves dissolving a specific amount of titanium isopropoxide in water and acetic acid while stirring continuously at 70 °C. the previous solution was stabilized using Lactic acid as a chelating agent to form a stable Ti–solution and to avoid premature precipitation. A transparent TiO_2 with adequate proportions was obtained. In the second step, barium acetate and yttrium acetate are dissolved in distilled water at 90 °C for 15 minutes and then added to the TiO_2 mixture. Initially, white precipitates are formed, and the solution becomes cloudy for 10 minutes, which then will be converted to a clear Ba-Ti-Y solution at 80 °C. The sol was converted into a viscous gel at 80 °C for 1 h. The gel was dried at 120 °C overnight and turned into a white dried gel. To avoid the agglomeration of the powders and improve reactivity, the resultant xerogel is processed in an agate mortar. Finally, the raw powders were calcined at the temperature of 950 °C for 3 hours to obtain BYT powders. The calcined powders were pressed into pellets and sintered at 1200 °C for 6h in air, with a heating/cooling step size of 5 °C/min.

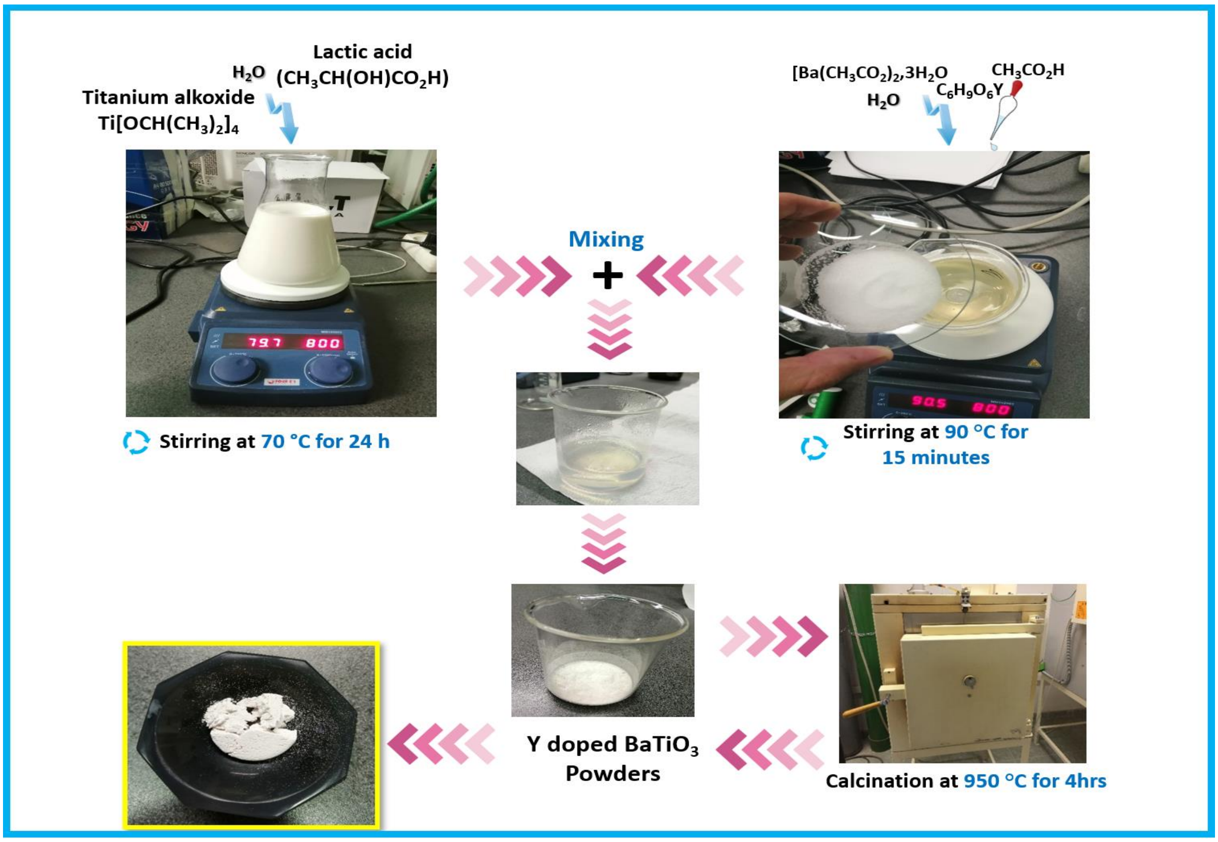

Figure 5. Synthesis flowchart of the ceramic materials

2.3 Preparation of co-doped samples

The Y and Sr doped/co-doped $BaTiO_3$ powders were synthesized via sol-gel technique [89] using Barium acetate trihydrate (Ba $(CH_3CO_2)_2.3H_2O$), Yttrium acetate (C6H9O6Y), Strontium acetate ($C_4H_6O_4Sr$), and Titanium alkoxide Ti $[OCH(CH_3)_2]_4$ as starting materials. Lactic acid (CH_3CH (OH) CO_2H) was employed as a peptizing agent, distilled water as a solvent, and acetic acid to dissolve the acetates.

Various processing procedures were used for the synthesis of BT, BSrT, BYT, BTY, BYTY, and BSrTY ceramic materials. The first stage consisted mainly of preparing a clear solution of Barium, Strontium, and Yttrium acetates individually using distilled water as a solvent, indeed, to prepare 100ml of the solution at 1 M/L, needs; 25.54g of Barium, Yttrium, and Strontium acetates powders, and a small drop of acetic acid (0.25ml), then the resulting mixture is continuously stirred at the temperature of 80 °C until a clear transparent solution is produced (Solution A). The next stage consists of the preparation of a clear solution of TiO_2. The synthetizes of 250 ml of 1M/L TiO_2 solution required; 71.75g of Titanium alkoxide, 150g of distilled water, and 11.25g of lactic acid. A white milky precipitate is produced as quickly as TiO_2 solution is added to the lactic acid while stirring it at 70 °C. After around 24 hours of continuous stirring, the resultant mixture progressively transforms into an entirely clear sol (Solution B). The next stage includes mixing the previously prepared solutions A and B. To guarantee the homogeneity of the final product, the prepared solutions were mixed with referring to the compositional formulas $BaTiO_3$, $B_{1-x}Sr_xTiO_3$, $Ba_{1-x}Y_xTiO_3$, $BaT_{1-x}Y_xO_3$, $Ba_{1-x}Y_xTi_{1-x}Y_xO_3$, and $Ba_{1-x}Sr_xTi_{1-x}Y_xO_3$ ($x=0.075$) with continuous stirring for 5 minutes. The obtained gel was powdered in a programmable oven at 80°C for 48 hours. Then, the xerogel product is ground to break up the powders' agglomeration and improve its reactivity. The powders, after grinding, were calcined at 950°C/3h under a heating rate of 5°C/min hours using a programmable furnace.

2.4 Preparation of BST-Cu and spark plasma sintering process

The obtained Barium strontium titanate powders (BST) through the sol-gel technique were mixed with high-purity Cu powders (Cu, purity: 99.8%, average particle size: 5µm, Sigma Aldrich, Germany). First, the BST powders were mixed with Cu content ranging from 0 to 40 wt.% by ball milling with ethanol in a resin container for 12 hours, utilizing zirconia balls as grinding media. Subsequently, the slurry was dried, and the resulting mixed powders were extracted. In order to densify the BST–Cu composite powders, spark plasma sintering (SPS) was carried out at Tallinn University of Technology, Department of Mechanical and Industrial Engineering, Tallinn, Estonia, using a graphite pressure die with an inner diameter of 20 mm. In a typical processing cycle, powder (2–2.6 g) was loaded into the die. The powders with different copper content were heated under vacuum initially up to 600 °C by a preset program within 3 minutes, and above this temperature, a heating rate of 100 °C/min was applied until the final sintering temperature (TF = 950 °C) was reached. The temperature was monitored and regulated using an optical pyrometer focused on the surface of the graphite die. After reaching TF, a uniaxial pressure of 50 MPa was applied, and a dwelling time of 15 minutes was maintained for sintering.

2.5 Characterizations of ceramic materials

In material science, characterization refers to the use of external techniques to probe. into the internal structure and properties of a material. Analysis techniques are used to. magnify the specimen, to visualize its internal structure, and to gain knowledge of the distribution of elements within the specimen and their interactions. This chapter presents the information about the theoretical concepts and relevant background for the characterization techniques employed to characterize the prepared ceramic. materials and techniques used for the measurements of various properties. Characterization of the material is the most important task to check the formation of a desired material, homogeneity, and other parameters. This chapter contains the detail information about characterization techniques which includes mainly,

2.5.1. XRD investigations of raw materials

The identification of mineral phases of the raw materials in dried powder form was conducted via the XRD technique. The used X-ray equipment was Miniflex II, Rigaku X-ray diffractometer equipped with a monochromator and operated in Bragg-Brentano geometry as shown in Figure 6. The samples were scanned in a broad range of diffraction angles (2θ) intervals (5-90 °) using CuKα radiation with a wavelength ($\lambda = 1.54184$ Å) at operating voltage and current of 40 kV and 25 mA, respectively. The scan rate was maintained at 1°/min with a step size of 0.0101 °. The existence of different phases in the tested samples was determined by comparing their XRD patterns to the PDF (Powder Diffraction File) Database of the International Center for Diffraction Data (ICDD) using X'Pert HighScore Plus software.

Figure 6. A Rigaku Miniflex II X-ray diffractometer setup in ceramic's laboratory at the University of Miskolc

2.5.2. Thermal analysis of raw materials using thermal analyzer

The thermal characteristics, including simultaneous differential and thermogravimetric analysis, were evaluated using MOM derivatograph, Setsys evolution thermal analyzer (Figure 7) at a heating rate of 10 °C min^{-1} in a static oxygen atmosphere in a temperature interval of 40-1200 °C. In this test, the sample and the reference holders are located on a common rod in a small-size tube furnace. This rod is connected to a four-decimal precision micro-balance. 15 mg of the samples were loaded in platinum crucibles. The data collection mechanism of the test identifies temperature and mass changes in the sample compared to annealed alumina (reference material).

Figure 7. MOM DErivatograph, Setsys evolution thermal analyzer

2.5.3. SEM and EDS investigations of the raw materials

The microstructural features and the morphology of the raw materials were examined via Carl Zeiss EVO MA10 scanning electron microscopy and Helios G4 PFIB CXe DualBeam SEM (Figure 8) equipped with Bruker microprobe, run at an operating voltage of 20 kV. The samples were coated with layers of gold using a sputter coater to create better conduction prior to SEM imaging. Secondary electron mode was used to capture the photos at various magnifications. Qualitative analysis of the elemental composition of the raw materials was obtained using an energy-dispersive X-ray spectrometer (EDAX Genesis). The combination of these analytical procedures supplies rapid and accurate interpretations for qualitative and quantitative investigation of the samples.

Figure 8. Helios G4 PFIB CXe DualBeam SEM setup in University of Miskolc

2.5.4. FT-IR analysis

The samples' infrared (IR) spectra were captured via Bruker Tensor 27 FT-IR (Fourier transform infrared spectroscopy) equipment (Figure 9). An average resolution of 4 cm^{-1} was used to capture 400–4000 cm^{-1} spectra. Prior to IR inspection, the sample powders were mixed with a small amount of KBr powder and ground to produce a homogenous mixture. The functional group's analysis was performed on all samples using the transmittance technique.

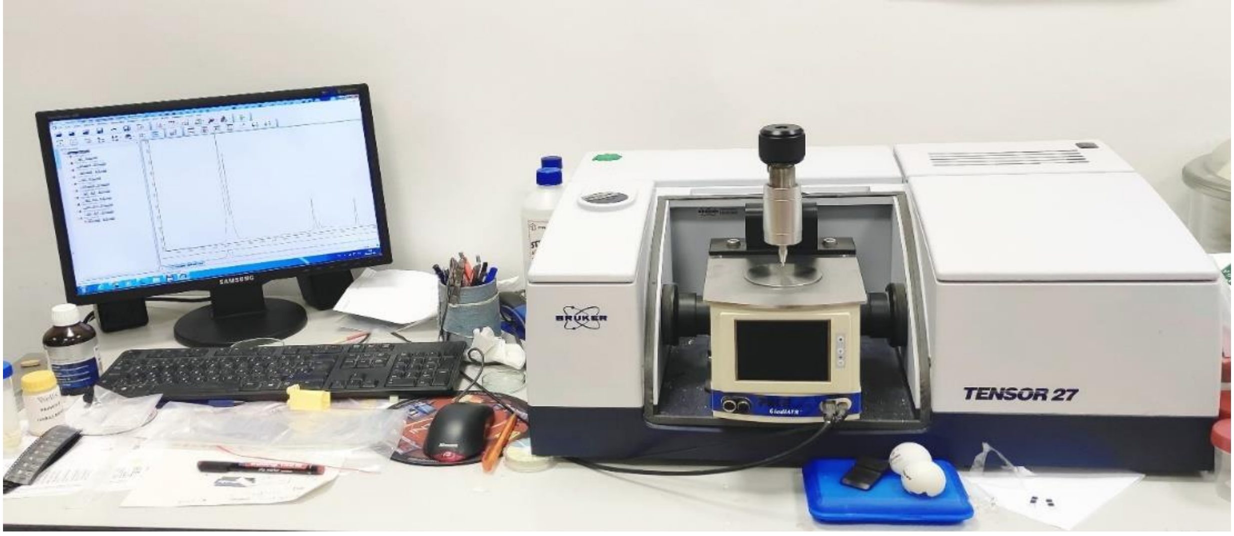

Figure 9. FT-IR analysis device

2.5.5. Thermal conductivity measurement

The default C-Therm TCi Thermal Conductivity Analyzer (Figure 10) employs the modified transient plane source (MTPS) technique used in characterizing the thermal conductivity and effusivity of materials. It employs a one-sided, interfacial heat reflectance sensor that applies a momentary constant heat source to the sample. Thermal conductivity and effusivity are measured directly at room temperature, providing a detailed overview of the heat transfer properties of the samples.

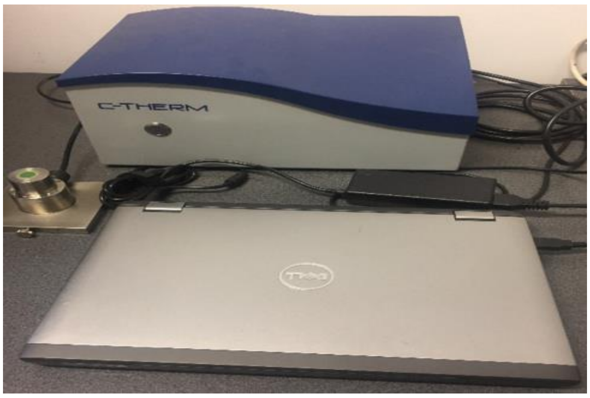

Figure 10. Thermal conductivity analyzer (TCi C-THERM)

2.5.6. Compressive strength test

The compressive strength was determined based on ASTM C67 using hydraulic universal testing equipment, as shown in Figure 11. The compressive strength test is performed on cylindrical samples. 5 compressive strength measurements are used to determine the average value of the compressive strength.

Figure 11. INSTRON 5566 universal testing equipment

2.5.7. UV-VIS spectroscopy

The UV photoreactor applied was equipped with a fluorescent lamp (Vilber-Lourmat T-6L UV-A, 6 W power, radiation maximum at 365 nm). Changes in the concentrations were followed with gas chromatograph (Agilent 6890 N) using a HP-PLOT Q column, equipped with thermal conductivity (TC) and flame ionization (FI) detectors and an Agilent 5975C VL MSD mass spectrometer.

2.5.8. Electrical measurements

Before applying electrodes to conduct dielectric measurements, the upper and lower surface layers of the compacted composites were eliminated by grinding with SiC paper. Subsequently, the prepared samples underwent coating with In-Ga to serve as electrodes for assessing their electrical properties. The Agilent impedance analyzer (Model: E4980A, Agilent Tech., Penang, Malaysia) was employed at room temperature to evaluate the complex impedance, dielectric loss, and frequency-dependent permittivity across a frequency range of $10^2 – 10^6$ Hz, varying the copper content. The direct current resistance of composites with different copper content was determined from room temperature to 200°C, with a heating rate of 3°C/min, utilizing a R–T measurement system (Model: ZWX-B, Huazhong University of Science and Technology, Wuhan, China). The temperature-dependent permittivity analysis was conducted under an electric field of 1 V/mm (Model: HP4284A, Agilent Tech.) over the temperature range from room temperature to 160°C, with a heating rate of 2°C/min.

3. Results and Discussion on $Ba_{1-x}Sr_xTiO_3$ (x=0-0.3) Ceramics

3.1. Thermal analysis (DTA/TGA)

Figure 12 shows the curves of the thermal degradation of $BaTiO_3$ and BSr5%T xerogel using TGA and DTA techniques. The raw powders were subjected to thermal decomposition at the temperature range of 22–1000 °C in the air with a heating rate of 5°C/min. The thermal analysis reveals that the total weight loss is approximately 37% divided into 4 stages of decomposition which are clearly seen in the TGA curves. The first mass loss (about 5% for pure $BaTiO_3$ and 6% for BSr5%T) recorded at approximately 26-229°C, corresponding to an endothermic process that attributed to the vaporization of water and lactic acid excess. The second step of mass loss, where the significant mass loss occurred. Indeed, TG-curve suggested a weight loss of approximately 25% in the temperature range from 229 to 557°C and 23.9% in the range of 229-550°C for $BaTiO_3$ and BSr5%T respectively, the weight loss in this stage can be due to the deformation of gel structure and to the decomposition of the Ba-Ti organic matter. Moreover, this step could be also due to the further combustion of organics, such as $(Ba,Sr)_2Ti_2O_5CO_3$ [115]. The endothermic peaks in the DTA curves at 307-389 °C corresponded to the decomposition of acetate compounds that exist in the samples and the vaporization of residual organic compounds. The third stage with a weight loss of 3% (557–783°C), and 5 % (550–763°C) for $BaTiO_3$ and BSr5%T respectively, are attributed to the formation of the carbonate phases (intermediate phases). The last step of weight loss is noticed in the range of 783 to 938°C (about 3%) and 763–874°C (2%). Furthermore, this range of temperature is attributed to the formation of $BaTiO_3$ and BSr5%T ceramic compounds. This step corresponds to exothermic peaks located at 923°C and 878°C in the DTA curves that are directly related to carbonate phase decomposition and can be attributed to the completion of polymorphic transformation of the samples which has no weight loss change. This study revealed that the phase temperature formation of present ceramic samples is around 950°C.

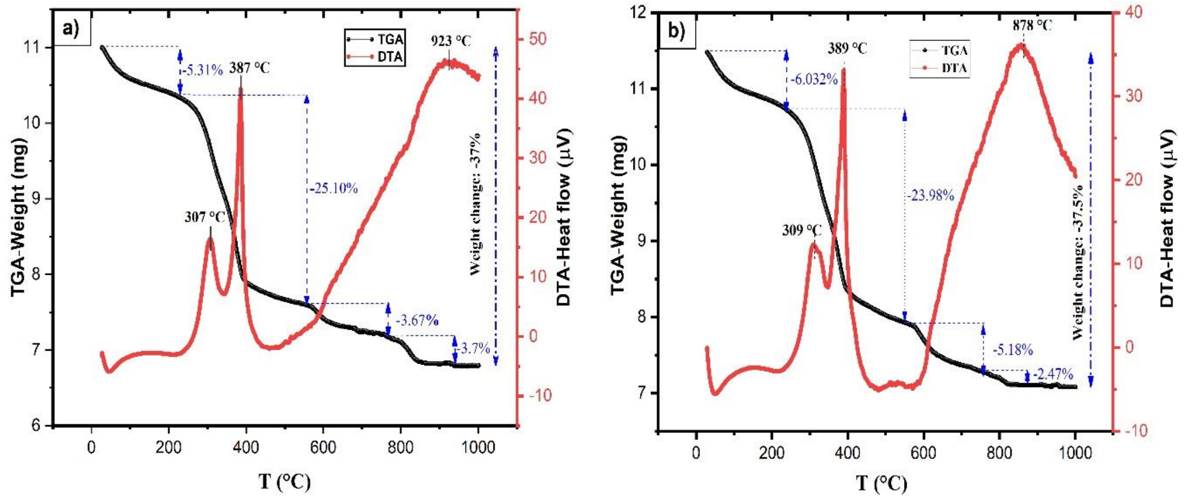

Figure 12. DTA and TGA curves of the uncalcined a) $BaTiO_3$ b) BSr5%T

3.2. Phase analysis

Figure 13a shows the X-ray diffractograms (XRD) patterns of $Ba_{1-x}Sr_xTiO_3$ ceramic powders (BSrxT, x = 0, 5, 12.5,15, 20 and 30%) calcined at 950 °C for 3h. It can be clearly seen that all

the presented diffraction peaks correspond to perovskite crystal structure with tetragonal phase for x = 0, 5, 12.5, 15, 20% samples, On the other hand, x = 30% sample, revealed the presence of cubic crystal structure phase. M. Arshad et al [62] produced BSrxT powders that are obtained via solid-state reaction process after calcination at 1100 °C for 3 h, but with the existence of the secondary phases, $SrTiO_2$ and SrO. Figure 13a also indicates that no secondary phase showing the presence of contamination or impurities is observed for up to 30 % of the Strontium dopant. As a result, the solubility limit of Sr into $BaTiO_3$ could be more than 30%.
The lattice constant (a and c) for BSrxT, where x = 0.0–0.3 prepared samples were estimated from XRD analysis taking into account tetragonal and cubic phases using relations (3) and (4) respectively [112];

Tetragonal structure

$$\frac{1}{d^2} = \frac{h^2 + k^2}{a^2} + \frac{l^2}{c^2} \tag{2}$$

Cubic Structure

$$\frac{1}{d^2} = \frac{h^2 + k^2 + l^2}{a^2} \tag{3}$$

Where a and c are the lattice parameters, (hkl) are Miller indices and d is inter-planar spacing.

The lattice parameters obtained from XRD data analysis for varying Sr^{2+} x substitution are exhibited in Table 3. The Lattice constant of $BaTiO_3$ (a = 3.9904 Å and c = 4.0418 Å) are in a good argument with the described values [116]. As shown in Table 3, the peaks shift to the higher angles (Figure 3b) suggest decreasing in the volume (V) of the unit cell. Indeed, a Barium substitution modified by Strontium in $BaTiO_3$ compounds (Ba is surrounded by 12 oxygen atoms) results in a reduction in the unit cell volume and lattice constant of the unit cell, the substitution is expected to decrease the lattice constant by increasing the substitution of Sr^{2+} which conforms and in a good argument with the Vegard's regulation [117]. Whilst Titanium is substituted by Strontium, causes an insignificant increase in the volume of the unit cell since the ionic radius of Sr^{2+} (1.18Å) is smaller than Ba^{2+} (1.35Å) however is although bigger than Ti^{4+} (0.6Å). Thus, the peak displacement to lower angles (x = 12.5%) is due to the occupation of Sr^{2+} ions of both Ba and Ti sites but with a preponderance of occupation of the Ba site. The plots of the lattice parameters a, c, and of the unit cell volume are exhibited in Figure 13c. Figure 13d shows the opposite influence of the (101) shifting peak and the unit cell volume as functions of x content. It can be concluded that the occupation of Ti-sites (octahedral) by Sr^{2+} creates vacancies of oxygen to compensate for the unbalance of charge. Furthermore, if the oxygen vacancies are predominantly located along the C axis [118], this contributes to a relatively greater reduction degree in the c lattice.

The variation of the crystallite size (D) was determined using the Debye Scherrer formula [119];

$$\mathrm{D} = \frac{\mathrm{k}\lambda}{\beta \cos \theta} \tag{4}$$

Where λ denotes the X-ray wavelength, θ is the Bragg diffraction angle, and β is the full width at half maximum (FWHM) of the XRD peak; k is a dimensionless shape factor, with a typical value of 0.9, D is the crystallite size, the estimated crystallite size was found to be in the range of 15-30 nm as given in Table 3 and shown in Figure 13e, on which this parameter is frequently decreasing.

The strain parameter was determined using the Wilson formula [120] and the calculated values are presented in Table 3,

$$\beta \cos\theta = \frac{0.9\lambda}{D} + 4\varepsilon \sin\theta \tag{5}$$

Where ε is the strain, β is the full width at half maximum (FWHM), D is the crystallite size, λ is the wavelength of CuKα, and θ is the peak position. The obtained strain is increased with increasing the Sr content due to the change in the shrinkages of the unit cell volume as Sr^{2+} concentration increases.

The other structural parameter such as X-ray density (ρ_x) was determined using the following formula [121];

$$\rho_x = \frac{ZM}{N_A V} \tag{6}$$

Where Z is the number of formula units in the unit cell (Z = 1), N_A is the Avogadro's number and M is the molecular mass of the as-prepared samples. The estimated X-ray density (as shown in **Table 3**) is in the range of 6.02 g/cm^3-5.793 g/cm^3. The obtained results indicated that Sr^{2+} ions have successfully doped into Ba^{2+} in a BSrxT lattice for (x=5, 15, 20, 30%) and both Ba^{2+} and Ti^{4+} but, with a predominance of occupation of the Ba-site in the case of x=12.5%.

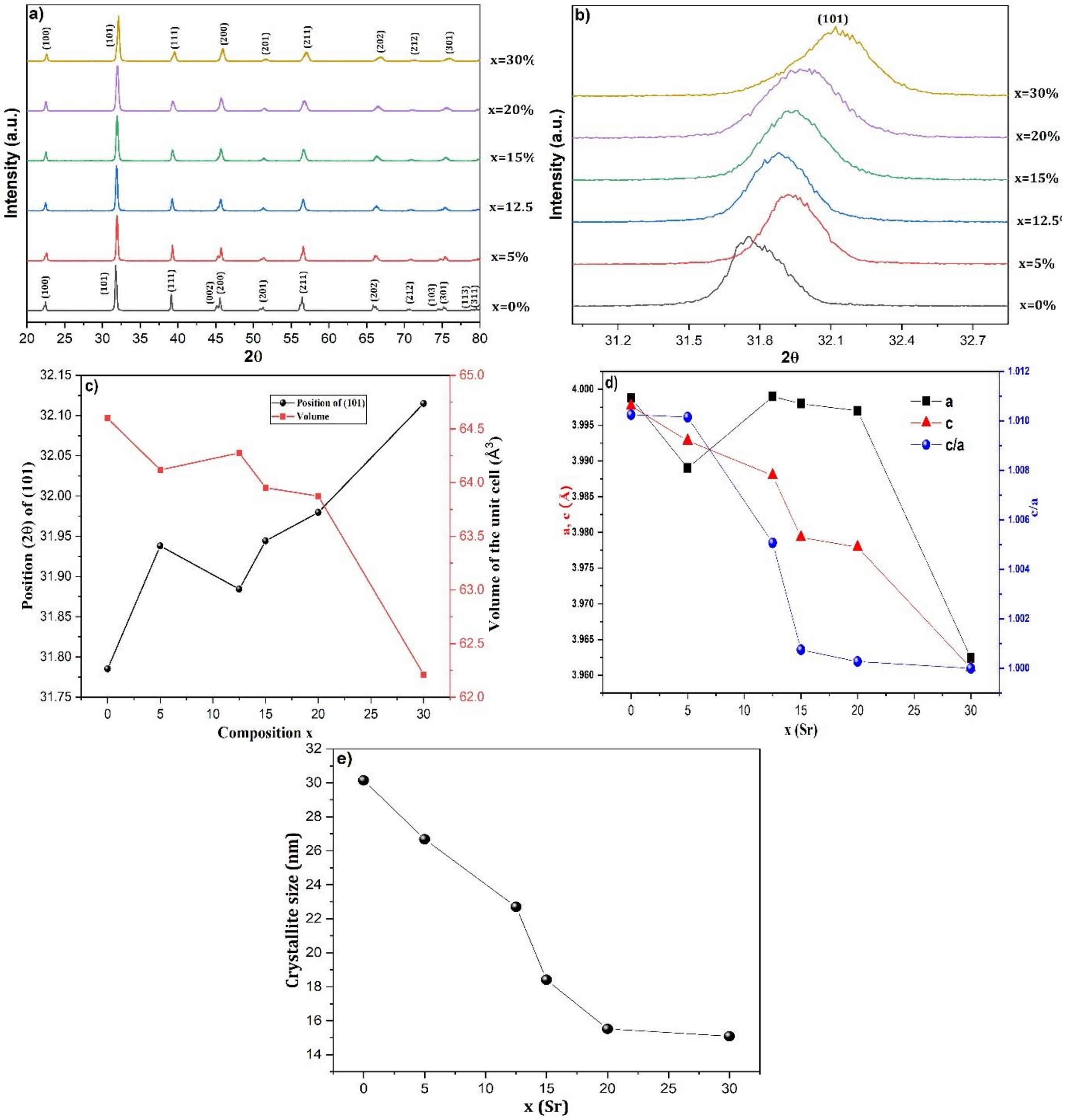

Figure 13. a) XRD patterns of BSrxT samples, b) shifting of the peak position (101), c) position of (101) peak and unit cell volume evolution of BSrxT in terms of x(Sr), d) Evolution of the cell parameters (a,c and tetragonality) of the as-produced BSrxT powders

Table 3. Physical parameters of BSrxT (x=0, 5, 12.5, 15, 20 and 30%) samples

Sample	a (Å)	c (Å)	c/a	V (Å^3)	2θ (101) (degree)	Crystallite size (nm)	Density (gm/cm^3)	Lattice strain (×10^{-3})
BSr0%T	3.9988	4.0398	1.010253	64.59802	31.78535	30.14602	6.020	1.27
BSr5%T	3.989	4.0295	1.010153	64.11789	31.93801	26.68294	6.001	1.32
BSr12.5%T	3.999	4.0193	1.005076	64.27665	31.88431	22.69694	5.891	2.13
BSr15%T	3.998	4.001	1.00075	63.952	31.9443	18.40822	5.835	2.19
BSr20%T	3.997	3.9981	1.000275	63.87368	31.97956	15.52299	5.793	3.56
BSr30%T	3.9624	3.9624	-	62.21211	32.11495	15.09129	5.539	4.09

The XRD results are confirmed by FT-IR spectra, as illustrated in Figure 14 Indeed, the presence of the band at 509 cm^{-1} to 533 cm^{-1} can be attributed to the stretching vibrations of Ti–O octahedra in the crystal lattice [122]. Moreover, this band is related to Ti^{4+} in octahedron geometry of coordination and anti-symmetric stretching of TiO_6 octahedra structure into $BaTiO_3$ lattice [112]. The absorption wavenumber of Ti–O bond was shown to shift to the higher side with increasing of the Sr^{2+} content. As mentioned earlier, the peak is shifted from around 509.75 cm^{-1} to 533.20 cm^{-1} when the amount of Sr^{2+} ranges from 0.0 to 30% which suggests as mentioned in the XRD analysis the shrinkage of the elementary cell volume. Furthermore, the Ti-O band could be also attributed to the phase transition from tetragonal to a cubic structure.

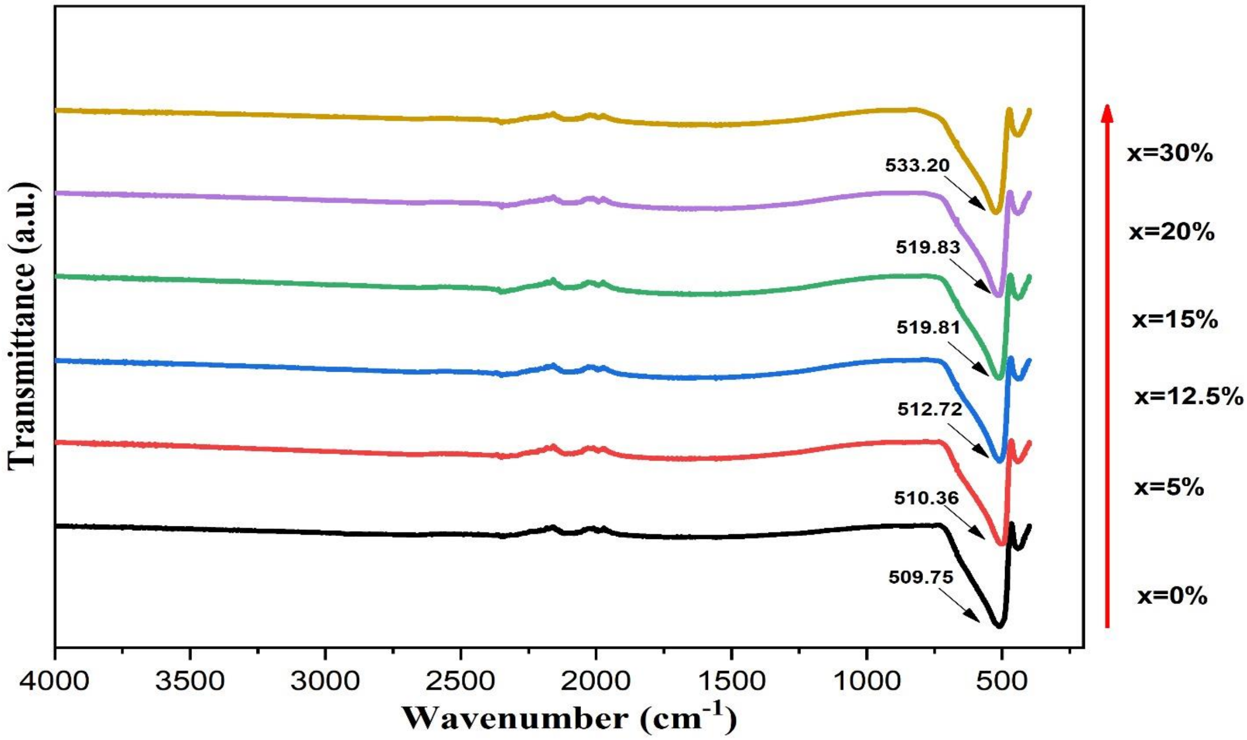

Figure 14. FT-IR spectrums of $Ba_{1-x}Sr_xTiO_3$ at different concentrations (x=0-0.3)

3.3. SEM and EDS analysis

The surface and morphology of the ceramic samples were observed through SEM. The SEM micrographs of BSr0%T, BSr20%T, and BSr30%T samples sintered at 1100 °C/4 h are depicted in Figure 15a, Figure 15b and Figure 15c respectively. The SEM micrographs revealed that the prepared ceramics are relatively dense, containing irregularly oriented grains in the form of flat blocks. The average grain size measurement was estimated with the help of ImageJ software and found to be approximately 4.6, 6.3 and 8.2 µm for x= 0, 15% and 30% respectively, showing that with increasing the Sr concentration, the grain size increases which is in a good agreement with the above XRD results. Besides, the pores observed in the ceramic images, especially those observed in Figure 15c, could be due to the fast cooling by ventilation as was reported by Niesz et al. [123].

EDS spectrum of $Ba_{1-x}Sr_xTiO_3$ (x = 0, 0.15 and 0.3) ceramics is presented in Figure 15d, Figure 8e and Figure 15f respectively. The obtained spectra from EDS show that all the representative peaks of chemical elements Ba, Sr, Ti, and O exist, which indicated that the $Ba_{1-x}Sr_xTiO3$ (x=0.0-0.3) have been successfully produced without any contamination. However, the intensity of Sr increases with the increase in Strontium concentration which indicates that Sr is completely incorporated into Barium titanate. On the other hand, the evolution of the intensity of the characteristic peaks of Ba and Ti are in the energy range of 4.36 to 4.5 KeV which precludes the possibility of clearly observing the change in intensity of these peaks.

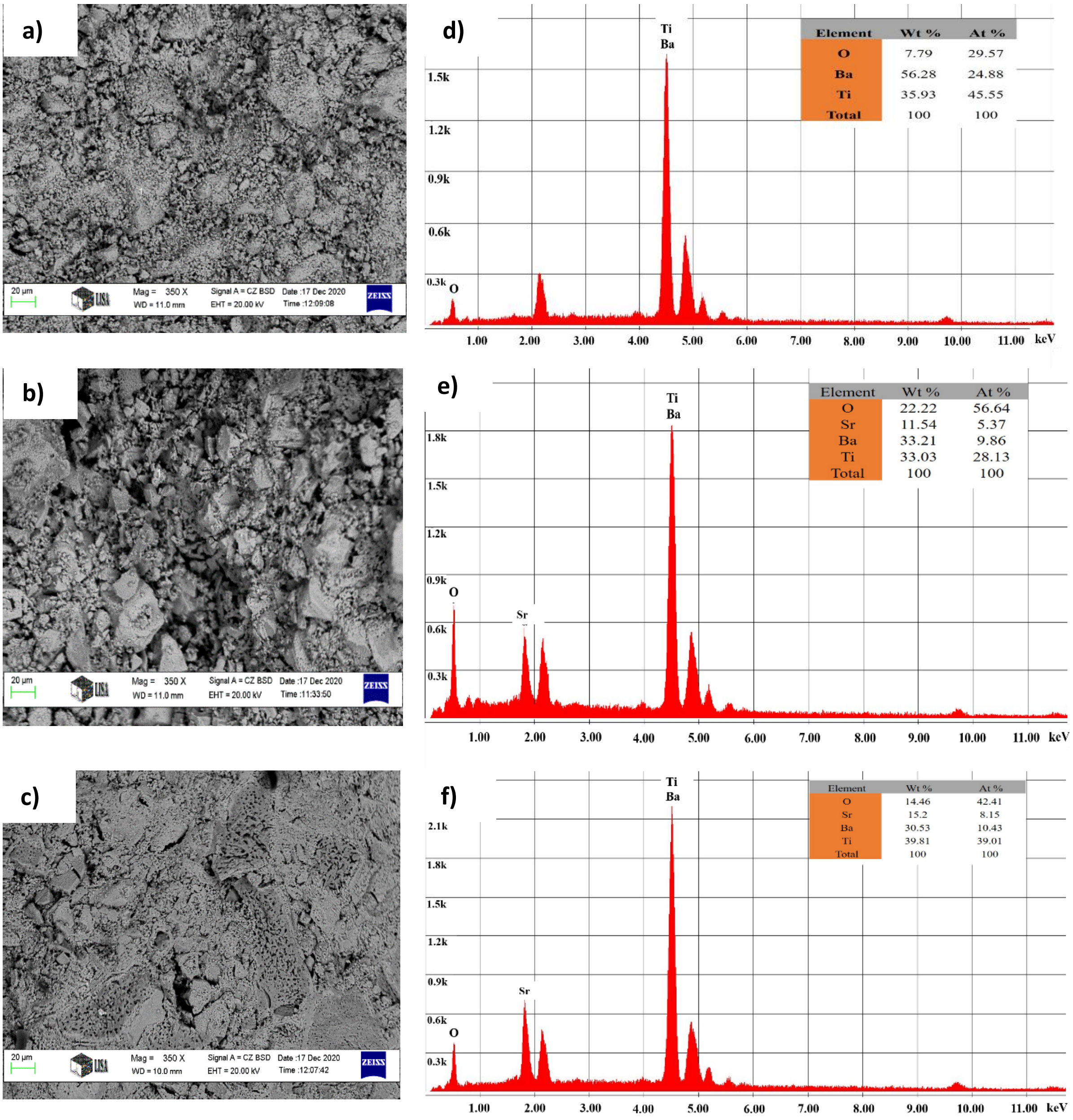

Element	Wt %	At %
O	7.79	29.57
Ba	56.28	24.88
Ti	35.93	45.55
Total	100	100

Element	Wt %	At %
O	22.22	56.64
Sr	11.54	5.37
Ba	33.21	9.86
Ti	33.03	28.13
Total	100	100

Element	Wt %	At %
O	14.46	42.41
Sr	15.2	8.15
Ba	30.53	10.43
Ti	39.81	39.01
Total	100	100

Figure 15. SEM micrographs and corresponding EDS spectra of (a,d) 0%, (b,e) 20% and (c,f) 30%.

3.4. Thermal conductivity

Figure 16 depicts the room temperature thermal conductivity of the produced samples as a function of the composition, x (0, 5, 12.5, 15, 20 and 30%) of the BSrxT. Pure Barium titanate room temperature thermal conductivity data described in the literature are found to be in the range of 1.3 to 6 $Wm^{-1}K^{-1}$ [124]. The variation of the heat conductivity can be due to different synthesis methods used to produce $BaTiO_3$ ceramic, the nature of the dopants substituted into this material, and various techniques used for the measurement of the thermal conductivity. In the present paper, the average thermal conductivity performed on $BaTiO_3$ ceramics is 2.24 $Wm^{-1}K^{-1}$, with a standard deviation of 0.02 $Wm^{-1}K^{-1}$, which is within the range of the reported data [88], [125]. The presented value of the thermal conductivity is increased with increasing Sr content and found to be in the range of 2.24-6.98 $Wm^{-1}K^{-1}$ (Table 4). This augmentation is due to the change in the strength of the bond between the atoms [126]. Moreover, the increase in the distance between Ti and O makes the bond relatively weak. In the system, these modifications in the strength of the bond tendency are more efficient for thermal conductivity than the scattering of the point defect.

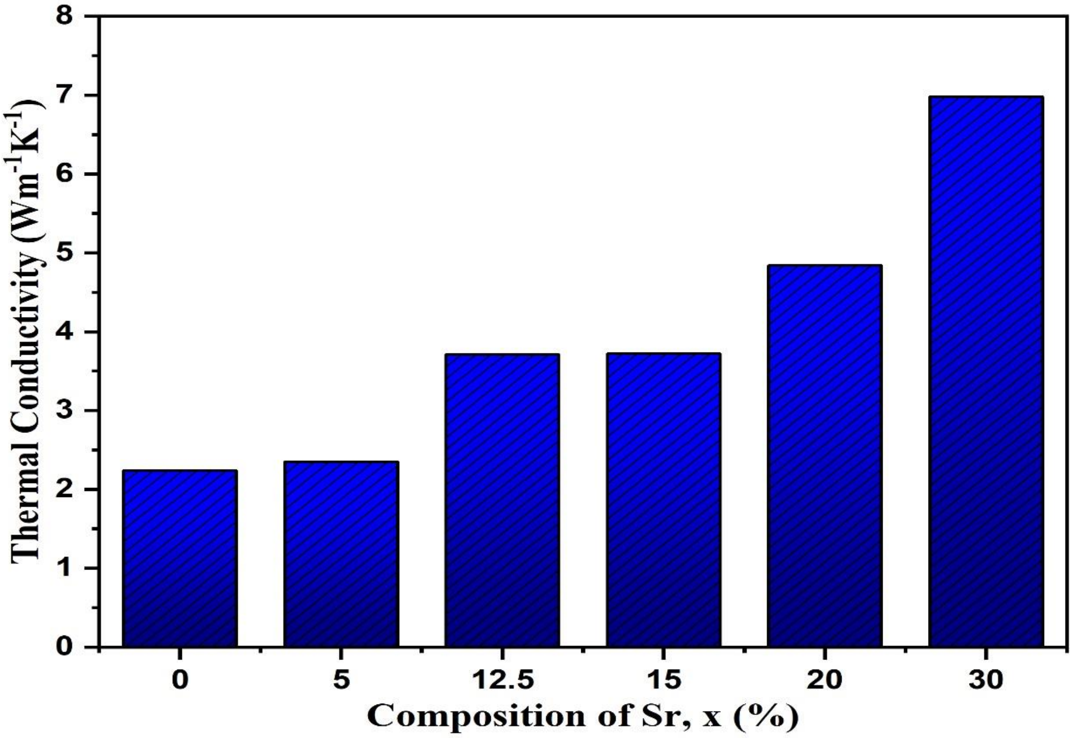

Figure 16. Thermal conductivity of BSrxT (x=0, 5, 12.5, 15, 20 and 30%) at room temperature

3.5. Mechanical properties

Figure 17 shows the variation of the compressive strength of the Sr modified Barium titanate ceramics recorded at room temperature. The values of modulus and the compressive strength of all the samples are given in Table 4. It can be seen from Figure 17 that the compressive strength of the as-produced ceramics was in the range of 31.03-32.91 MPa, therefore the obtained values of compressive strength showed an insignificant decrease when Sr concentration increase. The strength of the cohesion between the grains of the ceramic as well as the size and shape of the particles depending on the shrinkage, pores, and distance of the particles. The more grains that form near a irregular shape, the more nearly they are to attach the particles together, resulting in high compressive strength [127]. The higher compressive strength seen in this study was likely attributed to more grains forming the irregular flat blocks shape, which made the bonding much weaker. Besides, it can be observed from the SEM analysis there is an important difference in the microstructure between the pure $BaTiO_3$ and BSr30%T. For flat blocks of $BaTiO_3$ and BSr30%T which have an average grain size in the range of 4.6 µm to 8.2 µm, the estimated values of pores diameter have almost the same size and shape of pores, which, in the two cases, are in flat blocks shape. Furthermore, for the pure $BaTiO_3$ showing a smaller grain size (4.6 µm), the pores also have a lower size and consist of a flat block shape. The highest compressive strength of $BaTiO_3$ corresponds to the smaller grain size, in contrast, the lowest value was 31.14 MPa for the composition BSrxT (x=30%).

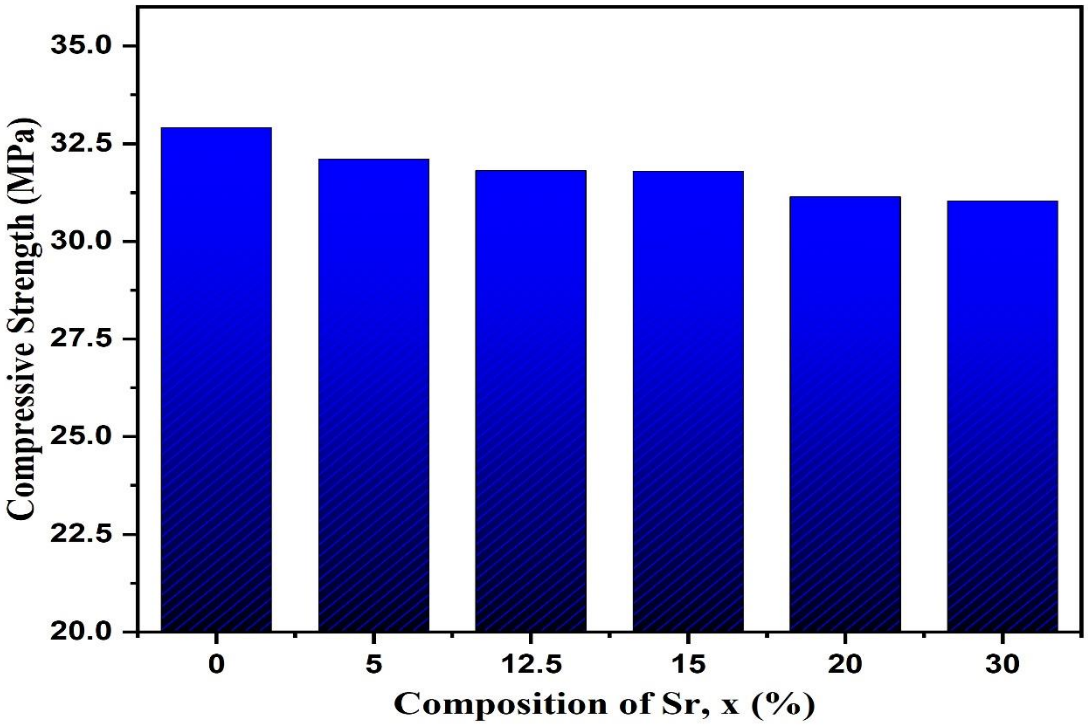

Figure 17. Compressive strength histogram of the as-prepared BSrxT ceramics samples (x=0, 5, 12.5, 15, 20 and 30%)

Table 4. The thermal conductivity value and mechanical properties of BSrxT (x=0-30%) ceramic materials after sintering at 1100°C/4h.

Samples	Parameter Thermal conductivity ($Wm^{-1}K^{-1}$)	Compressive strength (MPa)	Young Modulus (MPa)
BSr0%T	2.24	32.91	188.28975
BSr5%T	2.35	32.1	213.91143
BSr12.5%T	3.71	31.81	177.37345
BSr15%T	3.72	31.79	183.26072
BSr20%T	4.84	31.14	137.13244
BSr30%T	6.98	31.03	167.68385

4. Results and Discussion on Yttrium-Doped $BaTiO_3$ for Next-Generation Multilayer Ceramic Capacitors

4.1. Structural analysis using XRD

The XRD analysis was conducted to determine the phase purity and crystallinity of yttrium doped barium titanate ($Ba_{1-x}Y_xTiO_3$) at various doping concentrations (x = 0.00, 0.05, 0.125, 0.15, 0.2, and 0.3). The study used XRD spectra between 20 and 90-degree scan angles, and the samples were heated to 950 °C. The results showed that the powdered samples had a perovskite structure, as indicated by the diffraction pattern in Figure 18(a). The diffraction peaks observed at 2θ° = 22.23°, 31.41°, 38.74°, 44.96°, 45.42°, and 50.79° matched with those reported in the previous studies [15], [128]. The XRD analysis revealed that the average diffraction peaks of the samples were consistent with JCPDS card no. 00-005-0626, which indicates a tetragonal formation of $BaTiO_3$ ceramic for all the samples except x = 0.03, which shows a pseudocubic structure. This is likely due to the fact that yttrium is dissolved up to a certain depth in the BT particles [129], which leads to a reduction in tetragonality. A similar outcome was reported by Kim et al., who found that the ferroelectricity of BT decreases significantly when the grain size is below 7μm and the structure changes from tetragonal to pseudocubic [130]. The phase changes observed in the samples are a combination of tetragonal and cubic phases, which are presented as a pseudocubic phase. The XRD pattern of BT powder shows a pure tetragonal phase, but as the concentration of Y_2O_3 increases, there is a decrease in tetragonality. This result is consistent with our previous studies [14], [131], [132]. The XRD diffractogram revealed a double peak at around 2θ ≈ 45°, as shown in Figure 2(a), which indicates the presence of a tetragonal ferroelectric phase with (002) and (200) planes. The peaks at (002) and (200) show a minor distortion and shift towards a higher angle, as well as an increase in lattice parameters. This is believed to be caused by the incorporation of Y^{3+} ions at the Ba sites, which leads to an enlargement of the crystal cell volume. The structural properties can be inferred from the characteristic peaks (002, 200) at around 45°.

To obtain more accurate structural parameters, the Rietveld refinement was conducted using the FullProf software on the XRD data of the synthesized samples. Figure 18(b) presents a comparison of the experimental and fitted XRD patterns for the BY20%T composition.

The variation of the crystallite size (D) was determined using the Debye Scherrer formula [119];

$$D = \frac{k\lambda}{\beta \cos\theta} \tag{7}$$

The Rietveld refinement was used to determine various parameters such as the lattice parameters (a, b, and c), tetragonality (c/a), and crystallite size from the XRD data of the synthesized samples. The Rietveld refinement was performed using Eq. (7) and the X-ray wavelength (λ), Bragg diffraction angle (θ), and the full width at half maximum (FWHM) of the XRD peak were considered. Table 1 shows the results of these calculations.

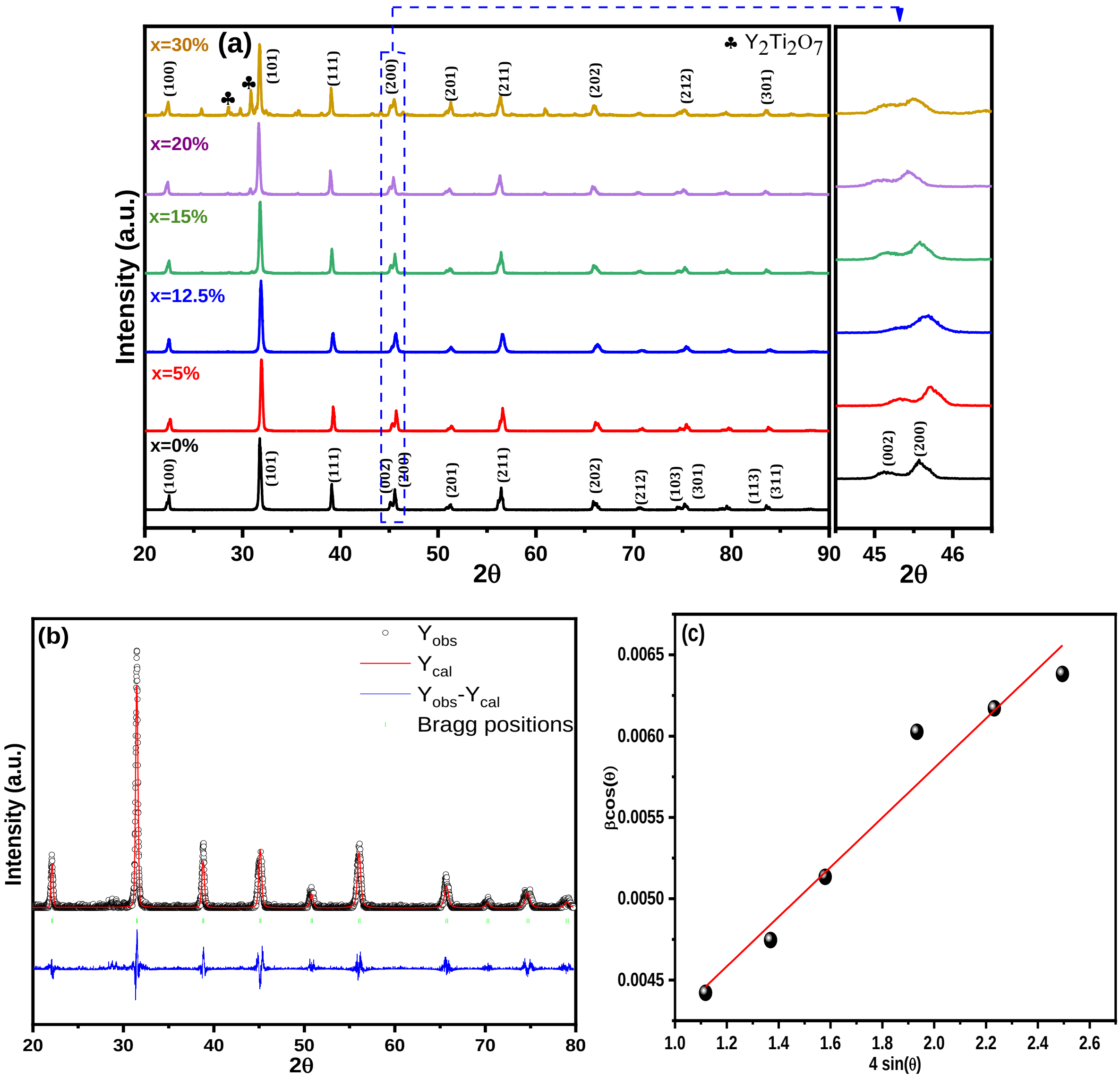

Figure 18. (a) XRD patterns of Y-BaTiO3 ceramics, (b) Rietveld refinement plot of BY20%T, and (c) W–H plot of BY20%T

Table 5. Structural parameters of BYxT, x = 0, 5, 12.5, 15, 20, and 30% samples

Sample $Ba_{1-x}Y_xTiO_3$	a=b (Å)	c (Å)	c/a	V (Å^3)	Space group	Crystalline size, D (nm)		Strain, Ɛ	
						Deby-Shearer	Williamson-Hall method	Deby-Shearer (×10^3)	Williamson-Hall method (×10^3)
x=0.00	3.9988	4.0398	1.0102	64.598	P4mm	30.14	29.36	5.287	1.27
x=0.05	3.9911	4.0293	1.0102	64.182	P4mm	27.52	28.20	4.356	1.35
x=0.125	3.9989	4.0291	1.0075	64.43	P4mm	29.89	29.99	5.015	1.25
x=0.15	3.9901	4.0185	1.0071	63.978	P4mm	34.78	33.53	7.581	3.47
x=0.2	3.9976	4.0021	1.0011	63.956	P4mm	33.12	31.41	6.125	1.52
x=0.3	4.0027	4.0051	1.0005	64.168	P4mm	25.03	23.16	4.030	2.24

The crystalline size of BT decreases initially for a doping concentration of x = 5% wgt. of yttrium, but then increases with further doping; for x =12.5%wgt., the cell volume also increases. The tetragonality or grain lattice parameters can be affected [133] by defects and impurities when sintering at a low temperature of 1200 °C. The XRD analysis suggests the formation of a perovskite phase with improved crystallinity in BYT. The change in the lattice parameters c values shows the incorporation of the dopant metal Y^{3+} into the Ba-site. However, it is also possible that the yttrium is integrated into the titanium site as it can occupy either the Ba or Ti site [14]. The formation of oxygen vacancies, grain growth, and grain boundary diffusion can depend on the sintering temperature and can also be influenced by temperature, impurities, and crystal orientation. The volume of the unit cell was calculated by multiplying a^2*c, and the results are presented in Table 5. The addition of Y^{3+} significantly enhances the tetragonal matrix of BYT, increasing the unit cell volume from 64.598 Å^3 (x = 0.0) to 63.956 Å^3 (x = 0.07). The lattice parameters (a, c) of the samples increase as the yttrium content increases, as a result of the variation in electronic density and ionic radii of Y^{3+}. This type of enlargement has also been observed for zirconium doping in a tetragonal matrix of $BaTiO_3$ [134].

The broadening of diffraction peaks in a material is mainly caused by lattice-strain that is initiated by crystallite defects and distortions, according to the suggestion of Williamson and Hall (W–H) [134].

$$W_{hkl} = W_{crystalite} + W_{strain} \qquad (8)$$

The W-H method states that the full width at half maxima intensity (W_{hkl}) is related to the lattice strain and crystalline sizes. The broadening that is attributed to the lattice strain can be denoted as Wstrain, which is calculated using the following equation [135];

$$W_{strain}=4\varepsilon\tan\theta \qquad (9)$$

Rearranging W–H Eq. (8) we get.

$$W_{hkl}\cos\theta=0.9\lambda C_s+4\varepsilon\sin\theta \tag{10}$$

The W-H method plots the W_{hkl} cosθ versus 4sinθ for Y-BT samples, as shown in Figure 2(c). The lattice strain and the average crystalline size can be determined from the slope and the y-intercept of the linear line. These values are obtained using Eq. (9, 10) and are presented in Table 1. Both the Debye-Scherrer and W-H analyses indicate that the crystalline size and strain of all the samples follow the same trend [135].

The perovskite (ABO_3) structure is relatively stable due to the large difference in ionic radius between the A-site and B-site ions, which makes it difficult for them to jump positions and produce corresponding resistance drift. The most prominent feature of the perovskite structure is that it has strong doping ability on both A-site and B-site, and other elements are often doped in experiments to enhance their original properties. The tolerance factor t of the perovskite structure was proposed by Goldschmidt in 1926, and the expression for ABO_3 is as follows [136]:

$$t=\frac{(r_A+r_O)}{\sqrt{2}(r_B+r_O)} \tag{11}$$

where r_A is the ionic radius of the A-site cation, r_O is the ionic radius of the oxygen ion, and r_B is the ionic radius of the B-site cation, which is a semi-empirical formula, which can roughly explain the stability of perovskite materials, and the tolerance factor of stable perovskite is between 0.77 <t <1.10.

The tolerance factor for pure BT ceramic is t =1.07, which suggests a slight deformation of the crystal structure, where $r_A(Ba^{2+})$ = 1.61 Å, $r_B(Ti^{4+})$ = 0.605 Å, and $r_O(O^{2-})$ = 1.4 Å. The incorporation of Y^{3+} (r (Y^{3+}) = 0.9 Å) into BT causes a reduction in Goldschmidt's tolerance factor. The values of t for $Ba_{1-x}Y_xTiO_3$ samples are calculated and presented in Table 6, which ranges from 1.07 to 1.051, similar to the results in ref [137]. Here it is expected that the A-site and B-site will be occupied by large and small ions respectively, and both A and B sites with different partitioning for each ion will be occupied by intermediate ions. However, using tolerance factors to assess the ions in different sites is simply a qualitative measure [137].

Table 6. Tolerance factor(t), Bulk density (ρb), X-ray density, (ρx), and Porosity (P) of BYT.

Sample $Ba_{1x}Y_xTiO_3$	Tolerance factor(t)	Bulk Density, ρ_b (g.cm^{-3})	X-ray density, ρ_x (g.cm^{-3})	Porosity, P (%)
x=0.00	1.070	2.490	6.033	58.72
x=0.05	1.068	2.398	6.175	54.52
x=0.125	1.061	1.229	5.879	40.15
x=0.15	1.056	2.783	5.778	40.08
x=0.2	1.055	1.691	5.745	39.25
x=0.3	1.051	1.613	5.695	35.90

The X-ray density of the synthesized samples have determined by the equation.

$$\rho_x = \frac{ZM}{N_A a^3} \tag{12}$$

where Z is the number of atoms per unit cell, M is the molar mass, N_A is Avogadro's number and a is the lattice constant of the samples respectively. The bulk density has been calculated by following formula [138].

$$\rho_b = \frac{m\pi}{tr^2} \tag{13}$$

Where m is the mass, t is the thickness, and r is the radius of the prepared pallet samples respectively. The porosity of synthesized BYT samples was estimated using the following relation [139].

$$P = (1 - \rho_b \rho_x) \times 100\% \tag{14}$$

ρ_x, ρ_b are the X-ray density and bulk density of the prepared samples, and porosity is measured using Eqs. (6), (7), and (8), respectively. The thickness of the BYT pellets was ~0.50 cm for all studied samples. The calculated values of X-ray density, bulk density, and porosity of the BYT samples are summarized in Table 6. With an increase in doping concentration, the X-ray density, porosity, and bulk density decrease.

4.2. FT-IR spectroscopy

FT-IR spectroscopy was used to study the functional groups present in ceramic powders. The results, shown in Figure 19(a), demonstrate the FT-IR spectra of Y-doped $BaTiO_3$ ceramic materials. The bands at 870 cm^{-1} and 1428 cm^{-1} are attributed to the O-H stretching vibration and deformation vibration, respectively, caused by the hygroscopic nature of the KBr used in the analysis. Two bands at 449 cm^{-1} and 479 cm^{-1} are present in all samples, the band at 438 cm^{-1} is associated with the Ti-O bending vibration along the polar axis, and the band at 479 cm^{-1} is assigned to Ti-O stretching vibration [140]. These bands indicate that all of the synthesized samples have a pure tetragonal phase. From Figure 19(b), the wavenumber position of the Ti-O bond stretching and bending vibrations changes smoothly as the amount of yttrium increases, this is due to the distortion of the unit cell when yttrium atoms are introduced into the $BaTiO_3$ lattice structure. However, the wavenumber position remains constant for the bending vibration as the Y content in the $BaTiO_3$ matrix changes.

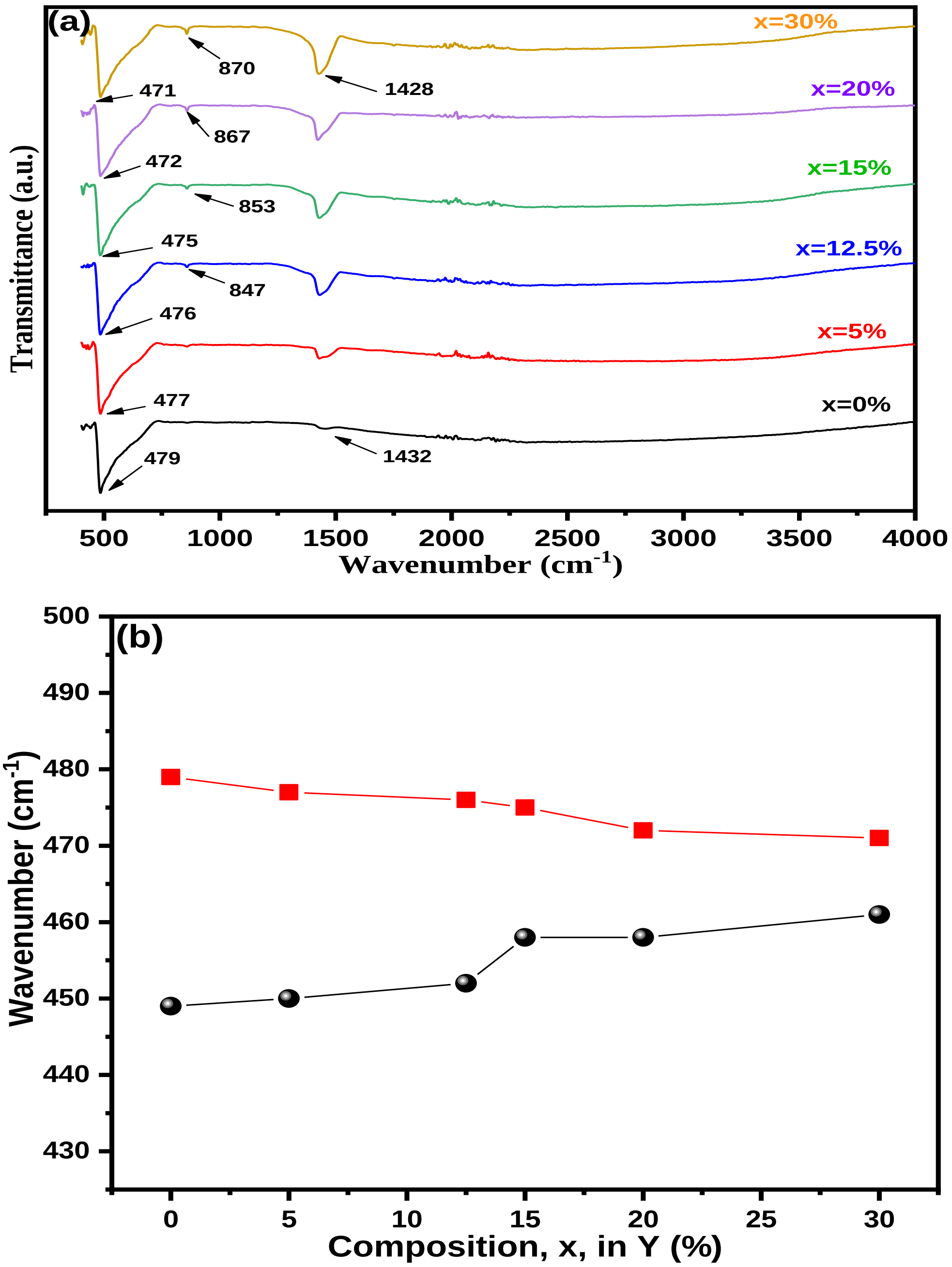

Figure 19. (a) FT-IR spectra of Y-doped $BaTiO_3$ ceramic powders and (b) absorption frequency Ti-O bond as a function of the Y content

4.3. Surface structure measurement using FESEM

Figure 20(a-c) shows FESEM micrographs of the BT, BY20%, and BY30%T pellets. The FESEM micrographs of the BT sample reveal an assortment of non-uniform grains with some coalescence. The interiors of the fleshy grains are clearly visible in the BT sample. Noticeable changes in the texture of the grains are observed with yttrium doping. It can be observed that each composition exhibits a dense microstructure, which can provide favorable electrical properties and improve the electrical stability of ceramics [141]. Furthermore, the grain size decreases with an increase in yttrium content, accompanied by a transition from surface grains with a porous structure to a nanoporous structure. A closer examination of Figures 20(b) and

20(c) shows that the surface layers of the pellets are covered with a large number of smaller grains, as well as larger grains of various shapes. Interestingly, sharp-edged hexagonal-shaped grains are embedded within the matrix of smaller grains in the A-site Y-doped samples. This structure is less pronounced in the simultaneously and B-site doped materials, where sedimentary growth patterns are observed. The irregular surface morphology in Y-doped samples may be attributed to the interaction between granular surfaces facilitated by the dopant cation.

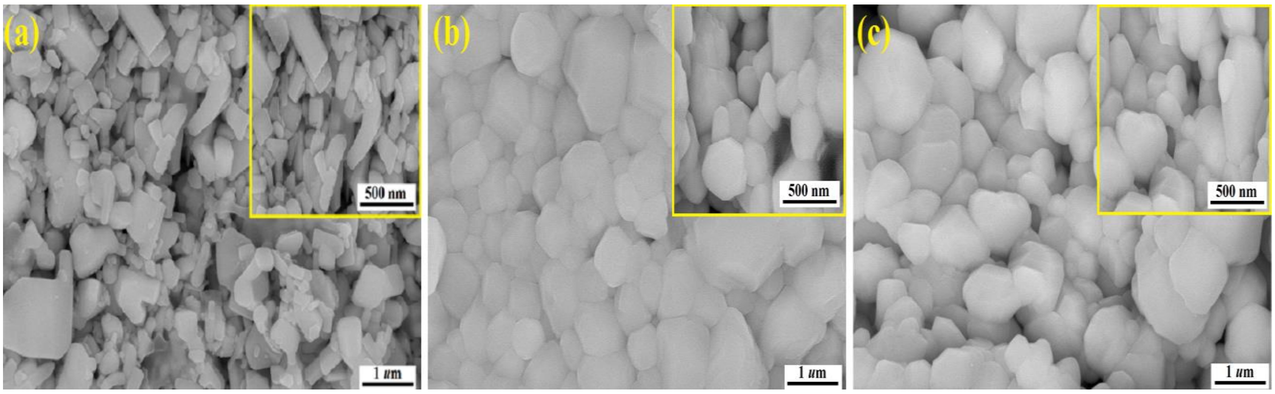

Figure 20. FESEM micrographs of $Ba_{1-x}Y_xTiO_3$ (where a, b, and c are x=0.00, 0.2, and 0.3 respectively)

An energy-dispersive X-ray spectrometer EDAX Octane Elect-Plus was used to check the distribution of individual elements within the grains. The EDS investigations show that the obtained ceramics contain only the elements introduced as substrates, with no other impurities detected in the spectrum. The content of barium and titanium elements slightly differs from the theoretical stoichiometry, whereas the content of yttrium is encumbered by a small uncertainty, which is related to their small participation in the whole mass of the sample, smaller than the threshold of device detection (Table 7).

Table 7. Theoretical and experimental contents of elements for BT, BY20%T, and BY30%T ceramics

Element	Content of element from EDS (wgt. %) (Measurement)	Theoretical Content (wgt. %)	Accuracy (wgt. %)
BT ceramics			
BaL	50.36	50.21	0.29
TiK	31.26	31.76	1.57
O K	18.38	18.03	1.94
BY20%T ceramics			
BaL	41.63	41.27	0.87
TiK	22.96	23.10	0.60
O K	15.47	15.63	0.88
Y L	19.95	20.00	0.25
BY30%T ceramics			
BaL	28.71	29.57	2.9
TiK	24.20	23.8	1.67
O K	17.06	16.63	2.58
Y L	30.03	30.00	0.10

The surfaces of the samples were checked in terms of element distribution homogeneity (Figures 21(a), 21(b), and 21(c)). The presence of each element is shown on the mapping in the form of points, where density informs about its concentration. The obtained results indicate that the element distribution is homogeneous in all samples, with some places characterized by lower concentrations due to the microstructural features of the material.

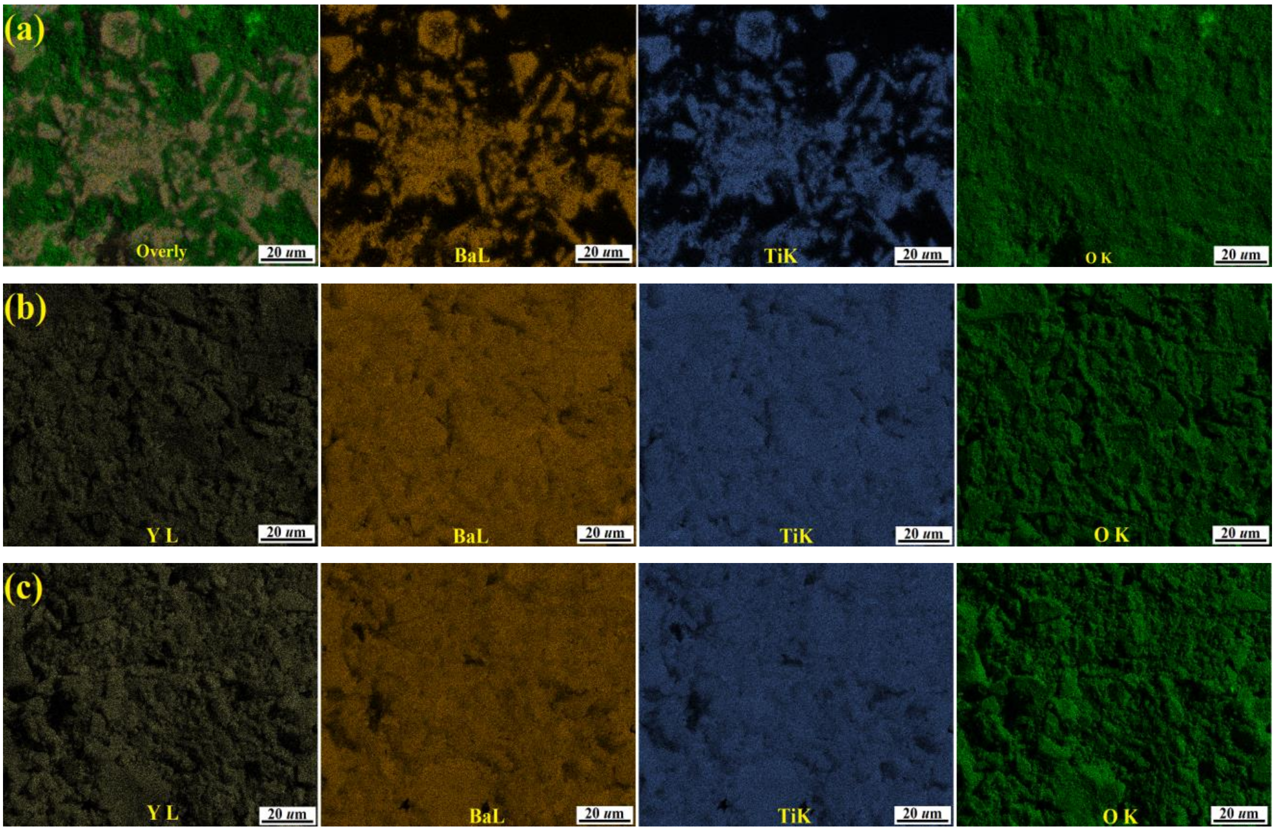

Figure 21. Mapping images for (a) BT, (b)BY20%T, and (c) BY30%T

4.4. Optical properties

The relationship between the crystalline structure and physical properties in perovskite materials is delicate, meaning that small changes in the structure can lead to significant variations in their physical and optical properties. To analyze the optical behavior of the materials, UV-Visible absorption spectroscopy was used. The results, shown in Figure 22, display the diffused reflectance UV-vis spectra of pure and Y-doped BT ceramics in the range of 350-800 nm. The doped samples exhibit an interesting behavior by absorbing visible photons in the region above 400 nm with a maximum absorption of 45% for highly doped BT. This absorption causes a drop in the UV spectra of yttrium-doped samples. Regardless of the Y site occupancy, all doped samples show three distinct peaks in the visible region of the spectra. The preference of Y in BT lattice has a slight effect on the absorption of photons.

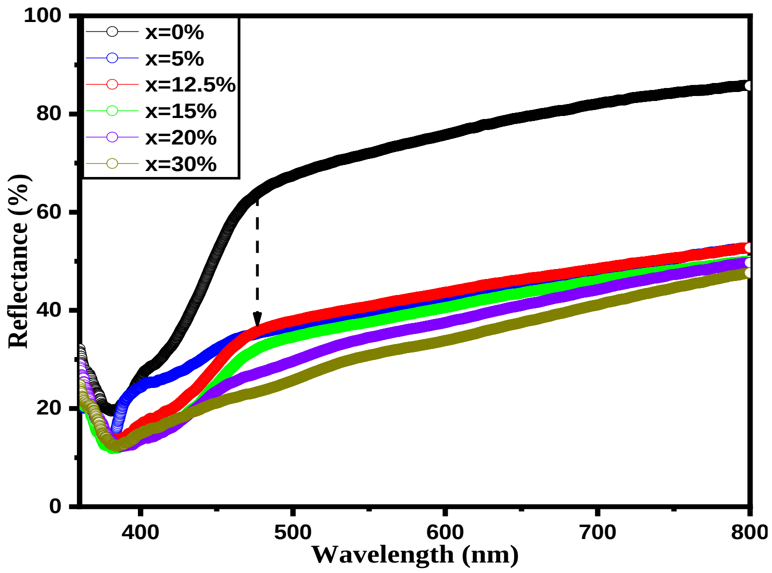

Figure 22. Diffused reflectance spectra of BYxT (x=0-30%) samples

The optical band gap energy (Eg) of $Ba_{1-x}Y_xTiO_3$ (x = 0-0.3) samples was calculated using the Kubelka-Munk (K-M) method. This method was chosen because it allows for accurate extraction of Eg values as well as the stimulation of the measured diffuse reflectance [142]. The Kubelkae-Munk equation at any given wavelength is represented by the equation:

$$F(R)=\frac{(1-R)^2}{2R}=\frac{k}{S} \qquad (15)$$

where K, S, and R parameters represent the absorption coefficient, scattering coefficient, and diffuse reflectance respectively. The F(R) function which is proportional to the absorbance coefficient is proposed by P. Kubelka and F. Munk [142]. This function was used to analyze the type of inter-band transitions by applying the McLean analysis [142]. The Tauc plot relation was then used to calculate the optical band gap (Eg) as shown in Figure 23;

$$F(R)h\nu = C_1(h\nu - E_g)^n \qquad (16)$$

where $F(R)=\alpha(\lambda)=\frac{k}{S}$ is the absorption coefficient, and C_1 is a constant dependent on the transmittance, called the band tailing parameter. The coefficient $\nu=c/\lambda$ is the light frequency, and h is Plank's constant h =6.626×10^{-34} J sec. The possible values for the index n are equal to 1/2, 2, 3/2, or 3 and each describes respectively direct allowed, indirect allowed direct forbidden and indirect forbidden transition types. From Eq. (16), the extrapolation of the tangential line from high photon energy gives the optical band gap value. So, in order to get the optical band gap value, the Tauc functions were used for BYT with the assumption that n=2. As shown in Figure 23 and listed in Table 8, the Eg values of BYxT (x=0, 5, 12.5, 15, 20, and 30%) obtained by extrapolating the linear part to the horizontal axis are in the range of 3.10 to 2.21 eV, which are considerably lower than that of the pure BT (3.10 eV). The band gap reduction of BY30%T (Figure 23(f)) is the most evident, and it's even more significant than those of other photovoltaic perovskite ceramics [143], [144]. The optical behavior of the materials can be explained by the electronic states of the highest energy band that is occupied by electrons (VBM) and the next highest energy band above the valence band that is unoccupied (CBM) generated by Y^{3+} cation doping. In BT, the VBM is around the O 2p orbital, which has a slight interaction with the Ti 3d and Ba 6p orbitals, whereas the CBM is around the Ti 3d orbital [145]. The position of the conduction band is affected by the electronegativity of the doping ions, the more electronegative the ions, the lower the conduction band position [146]. When a doping element is introduced, the VBM is localized around the Y 3d orbital. As the Y cations are more electronegative than Ti, the energy of the Y 3d orbital is lower than that of the Ti 3d orbital. This results in a downward shift of the conduction band edge into the band gap, leading to a reduction in the Eg. Moreover, according to a report by Choi [147], the optical band gap may also be related to the lattice distortion caused by the ion substitution. The lattice distortion increases as the radius of the doping ions decreases, resulting in a rearrangement of the molecular orbital and a decrease in the band gap. Yttrium is the preferred element to reduce the band gap of BT material according to the experimental data analysis. These results indicate that the band gap of BT ceramic can be effectively reduced by Y doping to improve its properties for visible and ultraviolet absorption. Optimizing the doping concentration can further modify the band gap of BT ceramic material. All these results suggest that the optical properties of BYxT (x=0-30%) ceramics can be regulated and the synthesized ceramics are good candidates for high-performance multilayer ceramic capacitors.

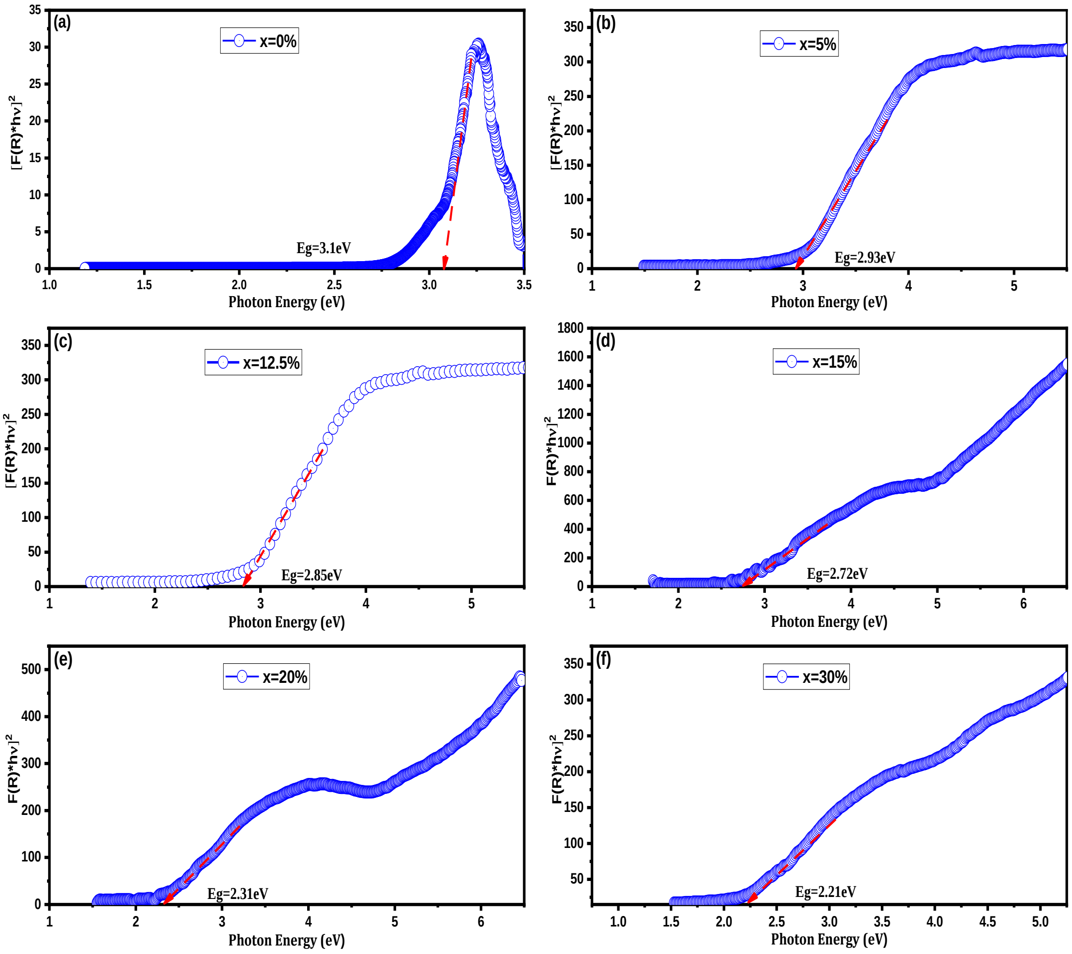

Figure 23. Band gap energy from Tauc plot of (a) BT, (b) BY5%T, (c) BY12.5%T, (d) BY15%T, (e) BY20%T, and (f) BY30%T

Table 8. Band gap value of $Ba_{1-x}Y_xTiO_3$, (x=0-0.3)

Sample	Band gap value (eV) This work	Band gap value (eV) Literature
$Ba_{1-x}Y_xTiO_3$, x=0.00	3.10	3.26[148], 3.2[149]
$Ba_{1-x}Y_xTiO_3$, x=0.05	2.93	3.11[150]
$Ba_{1-x}Y_xTiO_3$, x=0.125	2.85	2.91 [149]
$Ba_{1-x}Y_xTiO_3$, x=0.15	2.72	-
$Ba_{1-x}Y_xTiO_3$, x=0.20	2.31	3.14[150]
$Ba_{1-x}Y_xTiO_3$, x=0.30	2.21	-

As previously discussed, the band gap estimated from the reflectance results is influenced by both the structure parameters and the composition. The new optical band gap obtained for the compositions is a result of the displacement of the valence and conduction band edges. To visualize this shift, the conduction band minimum (CBM) and the valence band maximum (VBM) were calculated using the following equation:

$$E_{CB} = \chi - E_e - 0.5E_g \qquad (17)$$

$$E_g = E_{VB} - E_{CB} \qquad (18)$$

The equation used to calculate the CBM and VBM is where ECB and EVB are respectively the conduction band and the valence band potentials. Eg is the band gap estimated from the UV-vis results. Ee is equal to 4.5 and represents the energy of the free electrons vs hydrogen. χ is the electronegativity of the semiconductor and can be calculated as follows:

$$\chi = [\chi(A)^a \chi(B)^b \chi(C)^c \chi(D)^d \chi(E)^a]^{\frac{1}{a+b+c+d+e}} \qquad (19)$$

The parameters a, b, c, d, and e are the number of atoms in each composition, and χ(y) is the electronegativity of each element of the compound. The new optical band gap obtained for the compositions is a result of the displacement of the valence and conduction band edges. To visualize this displacement, the conduction band minimum (CBM) and the valence band maximum (VBM) were calculated using an equation that takes into account the conduction band and valence band potentials, the band gap estimated from the UV-vis results, the energy of free electrons, and the electronegativity of the semiconductor. The equation also includes parameters such as the number of atoms in each composition and the electronegativity of each element of the compound. Figure 24 illustrates the shift of the CBM and VBM which is in line with the shrink of the band gap. Both bands are affected as the amount of substitution increases, a downward shift is observed for the conduction band minimum while the valence band maximum shifts upwards.

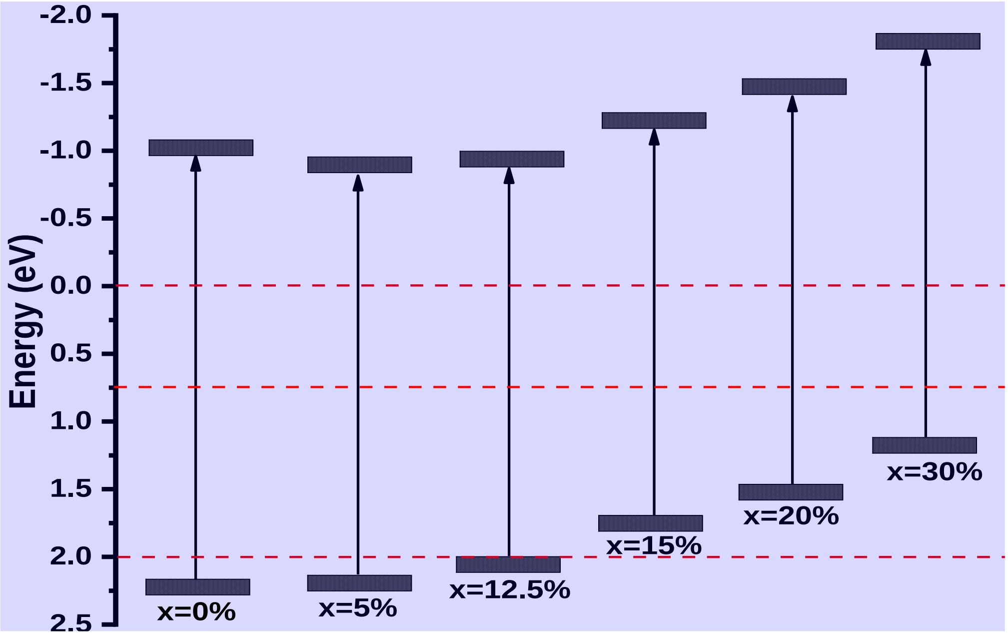

Figure 24. Schematic representations of the calculated conduction band minimum and the valence band maximum for the perovskite series $Ba_{1-x}Y_xTiO_3$ ($0 \leq x \leq 0.3$).

4.5. Thermal and electrical properties

The thermal and electrical conductivities of $Ba_{1-x}Y_xTiO_3$ ceramic samples (BYxT) were examined as a function of yttrium content at room temperature and 180°C, as illustrated in Figure 25. $BaTiO_3$ has lower thermal and electrical conductivity compared to Y, thus the addition of Y in $BaTiO_3$ system will lead to a percolation behavior. As the concentration of Y increases, the thermal and electrical conductivities follow a power law pattern, as demonstrated in equations (20) and (21) [151],

$$k \propto (V_T - V)^{-q} \quad \text{for } V<V_T \tag{20}$$

$$\sigma \propto (V_E - V)^{-t} \quad \text{for } V<V_E \tag{21}$$

The thermal and electrical conductivities of $Ba_{1-x}Y_xTiO_3$ ceramic samples (BYxT) were studied as a function of yttrium content. Equations (20) and (21) were used to estimate the thermal and electrical conductivities as a function of Y content, and the percolation threshold (V_T and V_E) was calculated. When the Y content is low, the heat conduction is mainly dependent on the vibration of phonons and the electrons play a minor role. The phonon scattering effect makes it difficult to improve thermal conductivity significantly. As the Y content increases, the Y phase becomes interconnected, allowing electrons to move freely and carry heat, resulting in a percolation behavior. The thermal percolation threshold V_T is 12.5% and the electrical conductivity of the compounds increases sharply when Y content increases from 12.5 to 30 %. The electrical percolation threshold V_E is calculated to be 12.5%. Although V_T is very close to V_E, BYxT samples with 12.5 % of Y content show a high thermal conductivity and relatively low electrical conductivity. The electrical conductivity of all the samples increases with measurement temperature which is typical of semiconducting behavior as shown in Figure 25(b). The sample 30%Y BT has a notably higher electrical conductivity when compared to other samples. This suggests that the carrier concentration and mobility in this sample are in an ideal doping range. It was also observed that there is a significant improvement in the electrical conductivity of $BaTiO_3$ samples when Y is added in greater than 20%. However, adding more than 30% Y to $BaTiO_3$ may decrease the conductivity because $BaTiO_3$ is a Mott insulator and in alloy form reduces the conductivity. The electrical conductivity is directly proportional to carrier concentration and mobility. Although it would be beneficial to use Hall effect measurements to measure carrier concentration and mobility separately, it is not possible for these samples due to their low conductivity. The sample BY5%T has a lower conductivity in comparison to BY30%T which has the same Y doping. This difference in conductivity is likely due to the presence of nanostructured pores which impede carrier mobility [152]. Our research aimed to investigate the impact of yttrium doping on the electrical properties of $BaTiO_3$ for use in MLCCs. Since $BaTiO_3$ is naturally insulating, adding Y in atomic percentage improves the electrical conductivity and converts it into an n-type semiconducting material through electron doping. Other dopants have also been shown to improve the electrical conductivity of $BaTiO_3$ in previous studies [153], [154].

The thermal conductivity of all the samples increases with temperature, as shown in Figures 25(a) and 25(b). The sample BY30%T BT has the highest thermal conductivity, which is likely due to the charge compensation of defects in the crystal structure near the Y atoms, which improves the electronic conductivity. Notably, the thermal conductivity of the sample with nanostructured pores (BT sample) is significantly lower compared to the sample BY30%T which has less nano porosity. This is likely caused by the phonon boundary scattering by the nanostructured pores of the sample in addition to phonon defect scattering by the Y atoms [155], [156]. Multiple theoretical studies have indicated that structures containing pores within the range of a few nanometers to a few tens of nanometers can effectively scatter phonons of various wavelengths [157]. The thermal conductivity for the porous sample is less than 2.24 W/K.m at room temperature and around 2.02 W/K.m at 180 °C. Thermal conductivity can be broken down into two parts: κel, which is the thermal conductivity caused by the movement of electrons or holes, and κph, which is the thermal conduction by lattice vibration, also known as phonon thermal conductivity. The κph can be expressed as $\kappa ph = 1/3 * C_V * V$, where the heat capacity (Cv) at constant volume and the phonon velocity (V) are constant, and thus the κph primarily depends on the phonon mean free path (MFP) (l). The mean free path of phonons in $BaTiO_3$ is on the order of 10^{-8} m, which is close to the nanometer scale, thus it is possible to scatter the phonons with nanoscale pores [158]. The mean free path of the phonons is increased due to the nanostructured pores in the sample BY30%T, resulting in a low phonon thermal conductivity. To isolate the role of phonon thermal conductivity, the electronic contribution must first be subtracted. According to the Wiedemann-Franz law, κel is directly proportional to the electrical conductivity and temperature, T. $\kappa el = LT\sigma$, where L is the proportional constant known as the Lorenz number which is an experimental value, and σ is the electrical conductivity. Normally, L is treated as a universal factor with the value of 2.44×10^{-8} $W\Omega K^{-2}$ for a degenerate semiconductor. In the samples of Y-doped $BaTiO_3$, the presented data show that the contribution of κel to the total thermal conductivity is insignificant. Furthermore, the increase in thermal conductivity with increasing yttrium content is likely because yttrium is a good heat conductor. Yttrium has a relatively high melting point and a relatively low atomic mass, which can contribute to its ability to conduct heat. Additionally, yttrium has a relatively low lattice thermal conductivity, meaning it does not transfer heat efficiently through vibrations of the atomic lattice. It is also possible that the increase in thermal conductivity with increasing yttrium content is due to the formation of a solid solution between the yttrium and $BaTiO_3$. When yttrium is added to $BaTiO_3$, it may form a solid solution in which the yttrium atoms are distributed randomly throughout the $BaTiO_3$ lattice. This can lead to an increase in the number of conduction electrons in the material, which can in turn increase its thermal conductivity.

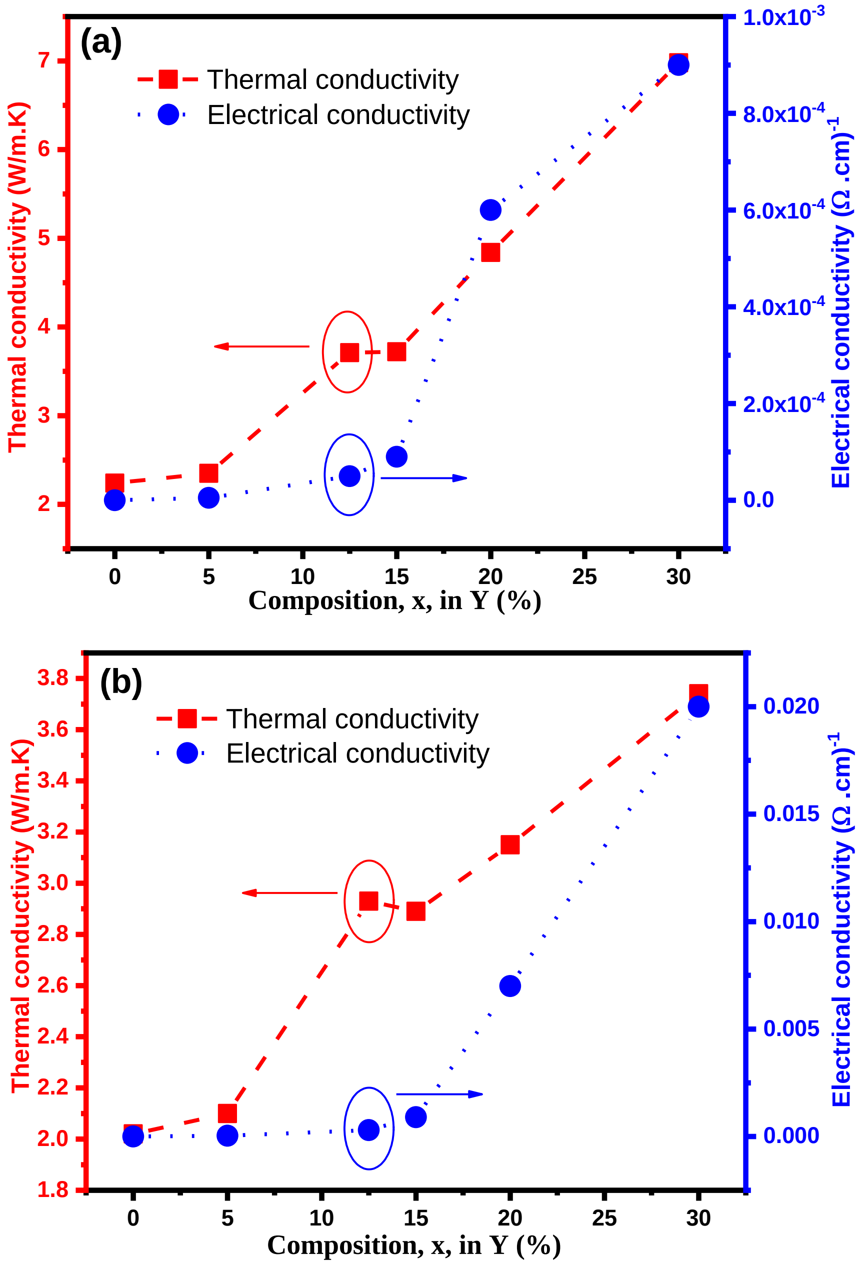

Figure 25. Thermal conductivity and electrical conductivity of BYT as a function of Y content at (a) Room temperature and (b) 180°C

To investigate the electrical behavior of $Ba_{1-x}Y_xTiO_3$ (x=0.05-0.3) ceramic samples, impedance analysis of the prepared sample was conducted at 180 °C. The V-I polarization plots, shown in Figure 26, consisting of three distinct regions: the activation loss (MN), ohmic loss (NP), and concentration loss regions (PQ). The loss that occurs near low values of currents is known as the activation loss and is likely caused by the electrostatic potential that overcomes the energy barrier [159], [160]. The activation energy is the minimum energy required to cross the energy barrier at the interface to initiate a reaction (electrochemical) at electrodes. The region NP indicated in the entire graphs of Figure 26(a-e) is the ohmic loss, when the energy barrier is crossed, ion transport occurs through the nanopores, which generates appreciable resistance, this is because of the resistance generation while the transport of the ions through the nanopores of the prepared materials towards the electrodes. The Ohmic loss region is a linear region, which is also evident from Figure 26(a-e). It is noted that pure BT ceramic has a nearly linear curve, while Y-doped BT ceramics exhibit curves with nonlinear regions. This reveals that Y-doped BT samples have varistor-like nonlinear current-voltage properties. The insufficient ions available for the electrodes in the highly reactive state may be responsible for the concentration loss as indicated by the PQ region of Figure 26(a-d). In the case of BYT, the presence of nanopores can affect the I-V characteristics in several ways. For example, the presence of nanopores may increase the surface area of the material, which can increase the number of charge carriers available to contribute to the current. This leads to an increase in the conductivity of the material (Figure 26(a,b)) and a corresponding decrease in the resistance. This can be seen as a decrease in the flattening of the I-V curve. The FESEM analysis (Figure 26(a-c)) of the prepared samples reveals that the pure BT sample has many nanopores, whereas the samples BY20%T and BY30%T have reduced porosity. The samples BY20%T and BY30%T do have some porosity, but less than the BT sample. On average, the porosity of the prepared barium titanate has been reduced with the increase in Y^{3+} content. The XRD analysis also confirms the reduced porosity of doped samples. The above optical analysis confirms the reduced band gap energy and defect states of the higher doped samples BYxT (x=5-30 wgt.%)), which indicates the generation of oxygen vacancies and unsaturated surface cations [161]. Additionally, the decrease in porosity results in a weak electrostatic potential which dissociates physisorbed atom bonds to a lesser extent, thereby reducing the offload current and output power. A systematic decrease in offload current and output power has been observed with the increase in Y^{3+} content. Thus, the present study shows that structural, optical, and voltage-current properties can be tuned using yttrium metal.

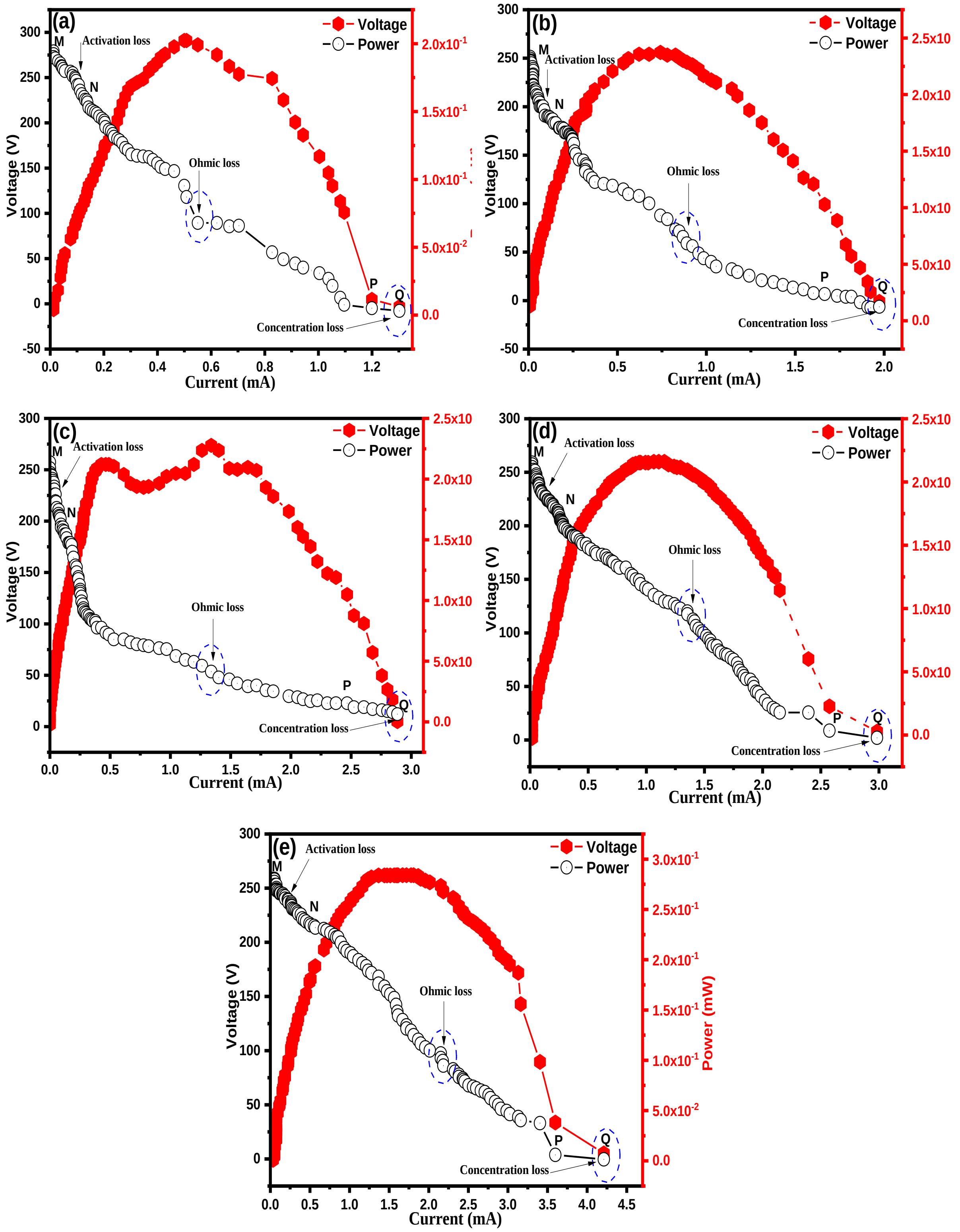

Figure 26. V–I characteristics measured at 180 °C of (a) BY5%T, (b) BY12.5%T, (c) BY15%T, (d) BY20%T, and (e) BY30%T

5. Results and Discussion on Role of A-site (Sr), B-site Y, and A, B sites (Sr, Y) Substitution in Lead-free $BaTiO_3$ Ceramics

5. 1. TGA and DTA study

Figure 27 illustrates the TGA and DTA-based thermal decomposition graphs of BT and BSrTY xerogel. The uncalcined samples were exposed to thermal degradation at temperatures between 22 to 1000 °C under a rate of 5°C/min. According to the thermal study, the overall mass loss was around 37 %, subdivided into 4 steps. The initial weight loss (about 5% for undoped $BaTiO_3$ and ~6% for BSrTY) was found at approximately 26-229°C, related to an endothermic mechanism associated with lactic acid excess and vaporization of water. In the next stage of weight loss, where the largest weight loss was observed. Although TG-curve predicted that the mass of BT and BSrTY would decrease by around 25% and 23.9%, respectively, in the range of temperatures of 229 to 557°C and 229-550°C, the mass loss in this step can be due to the degradation of the Ba-Ti organic matter and to the deformity of the gel structure. Additionally, this process may also be brought on by the continued combustion of organic materials like $(Ba, Sr)_2Ti_2O_5CO_3$ [162]. The presented endothermic peaks in the DTA spectra at the temperature range of 307-389 °C are related to the vaporization of leftover organic matter. The third step (557–782°C) ~3% of mass loss and(550–764°C) ~5 % for BT and BSrTY respectively, are due to the creation of the intermediate phases. The final stage was found between 782 to 938°C (about 3%) and 764–874°C (2%). This step is corresponding to the crystallization of BT and BSrTY, ceramic samples. Furthermore, the observed exothermic peaks at ~878°C and ~923°C in the DTA spectra are attributed to the decomposition of the carbonate phase. The present study found that the ceramic samples' phase formation temperature is around 950°C.

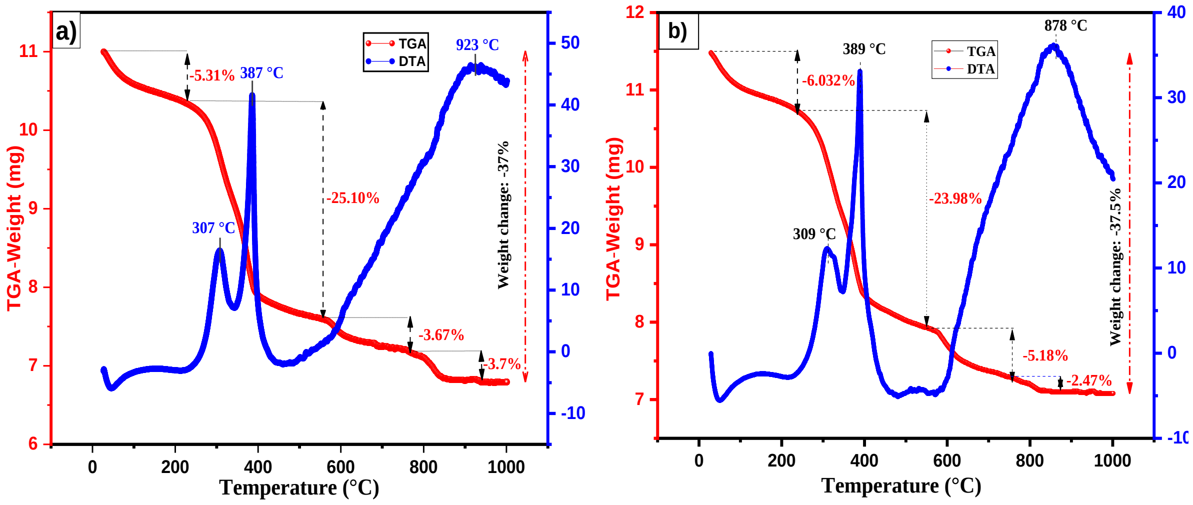

Figure 27. TGA and DTA curves of the uncalcined (a) BaTiO3 and (b) BSrTY

5.2. X-ray diffraction

The phase formation and the crystallinity are discussed using X-ray diffraction (XRD) analysis. The XRD patterns of BT, BSrT, BYT, BTY, BYTY, and BSrTY are presented in Figure 28a. No additional peaks were observed in the XRD patterns, which confirms the entire incorporation of 7.5%Sr and 7.5%Y as dopant ions in the $BaTiO_3$ system. Wang et al. [163]

produced $BaTi_{1-x}Y_xO_3$ (x =0-0.03) ceramics through a solid-state reaction process and identified the appearance of $BaTi_2O_5$ as an impurity phase. The secondary phase $Y(OH)_3$ was also seen in the XRD patterns of sol hydrothermally treated Y-modified $BaTiO_3$ powders (Y content such as x =0-0.03) [164]. The close observation of the XRD pattern by zooming in on the peak (101) (Figure 28(b)) over a range of $30° < 2\Theta < 34°$; displays a shift of the peak (101) initially to lower angles for BSrT, BYT, and BTY. A displacement of Ba^{2+} by Y^{3+} ions into $BaTiO_3$ lattice leads to a decrease in the volume (V), while the substitution of Y^{3+} into Ti^{4+} ions increases the volume of the unit cell. Therefore, this shift of the peaks to lower angles (BSrT, BYT, and BTY) can be attributed to Y^{3+} ions occupying both Ba^{2+} and Ti^{4+} lattice sites, especially with a preference for the occupation of Ti sites, which may lead to the generating of oxygen vacancies. In the case of BYTY and BSrTY, where a shift of the peaks to the higher 2θ angles was detected, this tendency is reversed; Both Ti and Ba sites are still occupied by Y^{3+}. However, Ba-sites are now more frequently occupied, which in this case results in a significant decrease of the oxygen vacancies as Y behaves as a donor [165]. Moreover, in both cases, barium substituted by strontium in $BaTiO_3$ ceramic (twelve oxygen atoms surround the Ba atom) caused a decrease in the volume(V) and lattice parameters. This outcome demonstrated that Sr^{2+} ions are properly incorporated into Ba^{2+} sites in BSrT and BSrTY systems [166]. Furthermore, the shrinkage within the lattice parameters could be justified by the substitution of Ba^{2+}, which has a higher ionic radius (1.61 Å) by the lower ionic radius Sr^{2+} (1.44 Å). This also unequivocally demonstrates the substitution of Ba^{2+} sites by Sr^{2+} ions without having the option of doing so in Ti^{4+} sites, since Ti^{4+} has an ionic radius of 0.61 Å, which is significantly lower than that of Ba^{2+} and Sr^{2+}.

In XYO_3 perovskite structure, X ions and Y ions are surrounded by 12 and 6 oxygen ions, respectively. Indeed, the modification of Ti^{4+} ions by Y^{3+} ones leads to an expansion of the cell volume (V) and to the generation of oxygen vacancies to balance out the charge imbalance. As a result of the valence state of the doped atoms, two cases can be taken into consideration.

(i) The charge imbalance is compensated by oxygen vacancies in the acceptor dopants because their ionic charge is lower than that of the substituted ion [167], [168].

(ii) Higher-ionic-charge donor dopants. In this regard, X- and/or Y-vacancies ($4X^{2+}+Y^{4+} \Rightarrow 4Y^{3+}V_Y$; $3X^{2+} \Rightarrow 2Y^{3+}+V_{X,}$ where X=Ba and Y=Ti) are created to maintain the charge balance. This behavior of the cell volume and lattice constants, specifically the shrinkage in parameter c, in the 3 cases BYT, BTY, and BSrTY can be interpreted by the generation of oxygen vacancies along the C axis [169].

The Fullprof program was used to carry out the structural refinement. Hence, R values (R_{Bragg}, R_p ,R_{wp}, Rexp, R_F and χ^2) are typically used to evaluate the quality of structural refinement [170]. After these samples were refined, the numbers of χ^2 and R values were obtained (see Table 9). Figure 29 shows the Rietveld refinement of BT BSrT and BYT, BTY, BYTY, and BSrTY ceramics powders calcined at 950°C for 3h. The results from X-ray diffraction for all compositions demonstrate the existence of only a single-phase perovskite structure, as clearly seen from the sharp diffraction peaks. In addition, the Refinement parameters confirmed that the BT, BSrT, and BYT compositions belong to tetragonal symmetry, while the BTY, BYTY, and BSrTY compounds confirmed they have cubic structure and a space group of Pm3m with no apparent secondary phase is detected.

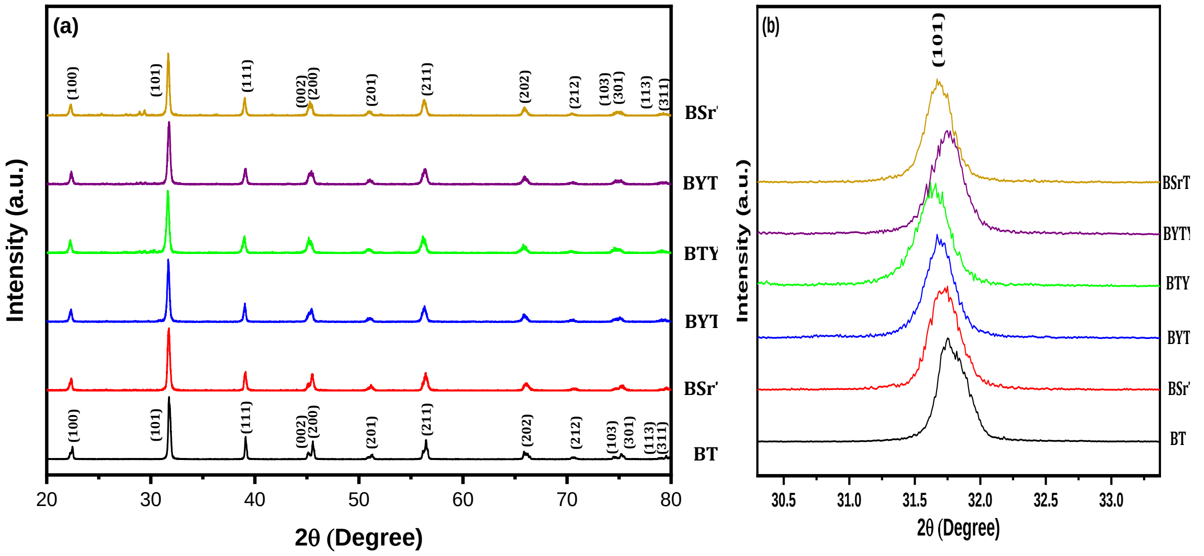

Figure 28. (a) XRD pattern of BT, BSrT, BYT, BTY, BYTY, and BSrTY ceramics heat-treated at 950°C for 3h (b) Shifting of the peak (101)

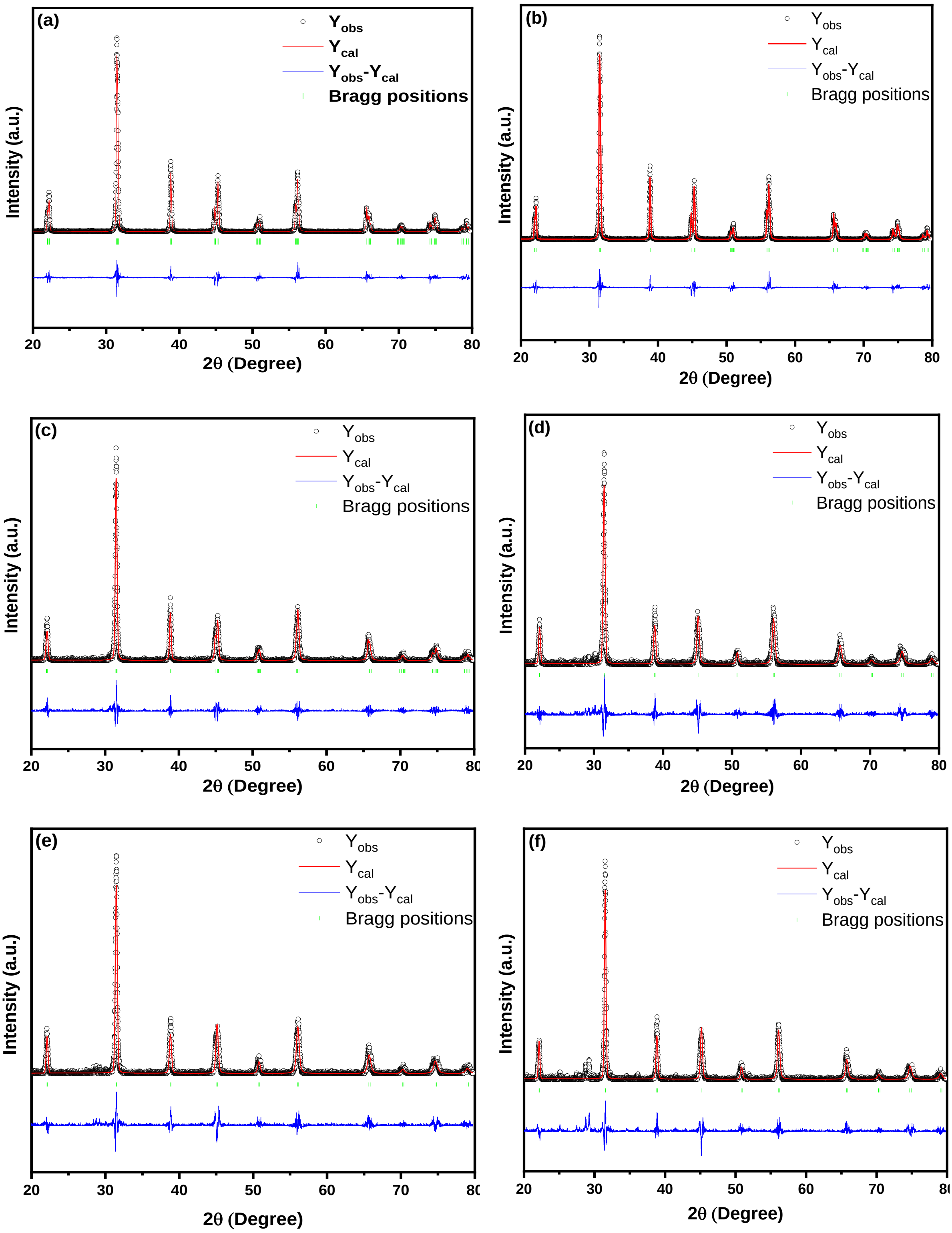

Figure 29. Structural refinement using the Rietveld method of (a) BT, (b) BSrT, (c) BYT, (d) BTY, (e) BYTY, and (f) BSrTY ceramics.

The estimated crystallite size was found to be in the range of 14–31 nm (Table 1), on which this parameter frequently decreases compared to pure $BaTiO_3$.

The lattice strain was calculated by means of Wilson's equation [120], [171];

$$\beta \cos\theta = 4\varepsilon \sin\theta + 0.9\lambda\, D \tag{22}$$

Where λ is the wavelength of Cu Kα, D is the crystallite size, β is the full width at half maximum (FWHM), θ is the peak position, and ϵ is the strain. The obtained strain value is increased with Y and Sr dopants due to the shrinkage changes in the volume cell.

5.3. FT-IR investigation

The Fourier transform infrared spectroscopy (FT-IR) spectrum of BT, BSrT, BYT, BTY, BYTY, and BSrTY powders in the wavenumber range from 450 to 4000 cm^{-1} are displayed in Figure 30. These spectra show two sets of absorption bands. The first one is characterized by a wide band in the low-frequency range from 460 cm^{-1} to 723 cm^{-1}, associated with the vibrations of the TiO_6 octahedron. Moreover, all the samples show the molecular fingerprint of $BaTiO_3$, as revealed by the Ti-O-Ti and Ti-O bonds in the range of 460 cm^{-1} to 723 cm^{-1}. The absorption peaks for the same mode of BT, BSrT, BYT, BTY, and BYTY, were obtained at around 460, 463, 465, 467, 470, and 470 cm^{-1}, respectively. The incorporation of Sr or/and Y into the $BaTiO_3$ lattice moved the characteristic peak of Ti-O to higher energy values. In our samples, the incorporation of Sr^{2+} and Y^{3+} ions into Ba^{2+} and Ti^{4+} sites influenced the binding distance between Ti^{4+} and O^{2-} ions resulting in a high binding strength [172], [173]. In addition, the observed bands in the range of 1430 cm^{-1} to 1550 cm^{-1} could be contributed to the symmetrical and antisymmetric vibrations (stretching of carboxyl groups bound to barium and/or titanium (COO^{-})). The presented results are therefore, in good accordance with the reported analysis in the literature [172]. The observations made on infrared spectra agree well with those revealed by XRD analysis.

Table 9. Crystallographic data of BT, BSrT, BYT, BTY, BYTY, and BSrTY ceramics using the Rietveld refinement method.

	BT	BSrT	BYT	BTY	BYTY	BSrTY
a (Å)	4.002410	3.995282	4.006745	4.020604	4.019073	4.015099
b (Å)	4.002410	3.995282	4.006745	4.020604	4.019073	4.015099
c (Å)	4.039425	4.024120	4.033381	4.020604	4.019073	4.015099
Volume (Å^3)	64.7087	64.23412	64.75192	64.9941	64.91988	64.72749
Structure	Tetragonal	Tetragonal	Tetragonal	Cubic	Cubic	Cubic
Space group	P4mm	P4mm	P4mm	Pm3m	Pm3m	Pm3m
x (Ba)	0			0.5		
y (Ba)	0			0.5		
z (Ba)	0			0.5		
x (Ba, Sr)		0				0.5
y (Ba, Sr)		0				0.5
z (Ba, Sr)		0				0.5
x (Ba, Y)			0		0.5	
y (Ba, Y)			0		0.5	
z (Ba, Y)			0		0.5	
x (Ti)	0.5	0.5	0.5			
y (Ti)	0.5	0.5	0.5			
z (Ti)	0.48347	0.47010	0.51980			
x (Ti, Y)				0	0	0
y (Ti, Y)				0	0	0
z (Ti, Y)				0	0	0
x (O1)	0.5	0.5	0.5	0.5	0.5	0.5
y (O1)	0.5	0.5	0.5	0	0	0
z (O1)	0.05854	0.02015	0.02323	0	0	0
x (O2)	0.5	0.5	0.5			
y (O2)	0	0	0			
z (O2)	0.51642	0.51500	0.53198			
R_{Bragg}	5.027	6.786	7.30	12.31	11.66	10.52
R_p	17.3	23.80	24.5	31.80	30.2	33.4
R_{wp}	26.5	32.20	33	39.70	37.8	42
R_{exp}	22.15	40.95	39.3	40.18	38.47	38.69
R_F				7.89	7.64	7.32
χ^2	1.43	0.61	0.70	0.97	0.96	1.18
Crystallite size (nm) (D)	14	17	18	21.0	26	31
Strain (ϵ)	1.27	1.33	1.85	2.21	4.19	4.56

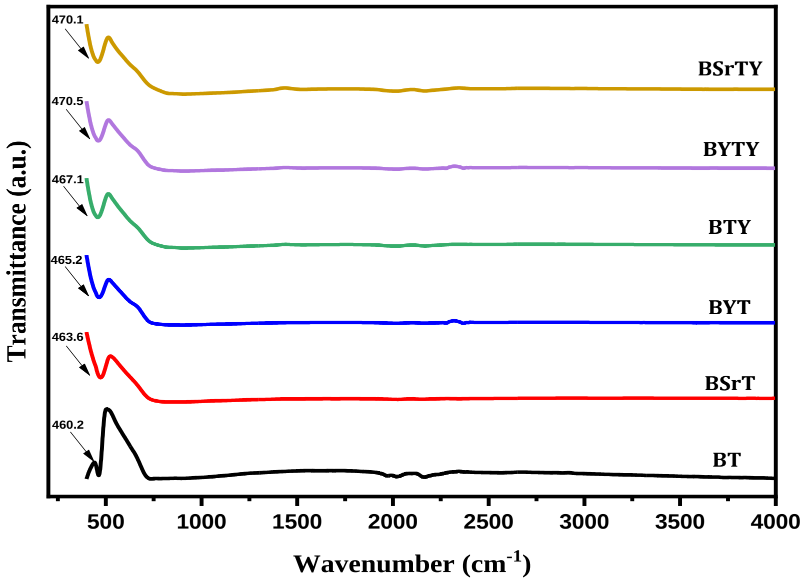

Figure 30. FT-IR spectra of the BT, BSrT, BYT, BTY, BYTY, and BSrTY ceramic samples

5.4. SEM and EDS analysis

The morphology and the microstructure of the obtained samples were analyzed using SEM. The micrographs provided by the scanning electron microscopy of BSrT, BYT, BTY, BYTY, and BSrTY sintered at 1100°C for 4 hours are given in Figure 31. They show that the ceramics are slightly dense, homogenous, and have irregularly shaped grains in flat block form (BSrT, BYT, BTY, BYTY) and with fine size and almost spherical shaped particles in the case of BSrT. The average grain size decreased under doping from around 4.6 µm (pure sample) [15] to around 0.51 µm (sample with BSrTY) (Table 10). It can be noticed that the above-recorded values relative to the sintered pellets are higher than those of the crystallite sizes of the calcined powders due to the sintering process, which enhances the mechanical resistance of the samples. The observed pores in the ceramic images could be attributed to the rapid cooling as was studied by Niesz et al.[123].

The characterization by X energy dispersive spectroscopy (EDS) of the sintered samples is given in Figure 31. These results confirm the presence of Ba, Sr, Y, Ti, and O elements, which indicate that the BSrT, BYT, BTY, BYTY, and BSrTY ceramics are compositionally homogeneous and have been successfully produced without any contamination. However, It is unable to see the change in the intensity of the distinctive peaks of Ti and Ba since their evolution occurs in the energy region from 4.37 to 4.49 KeV.

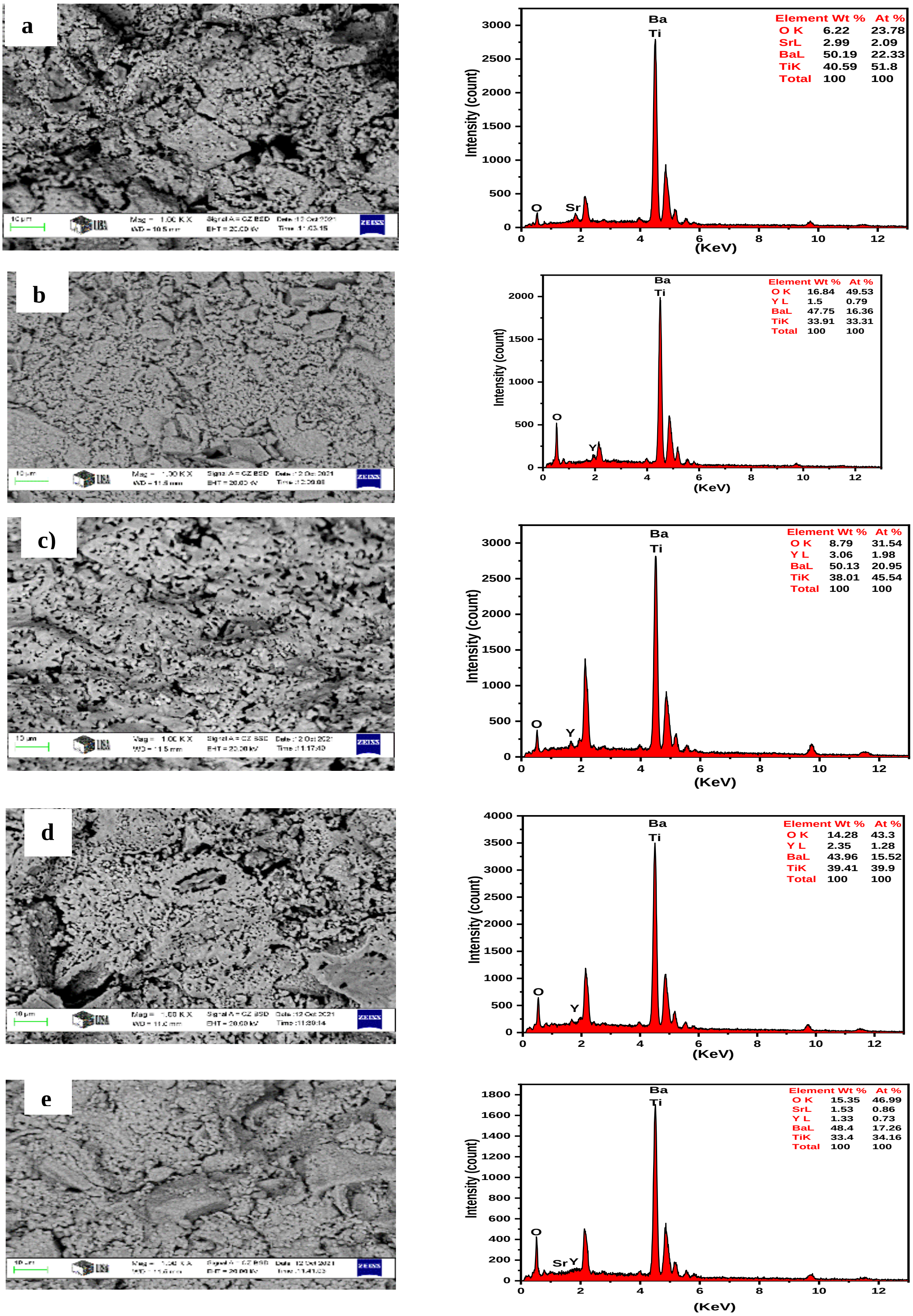

Element	Wt %	At %
O K	6.22	23.78
SrL	2.99	2.09
BaL	50.19	22.33
TiK	40.59	51.8
Total	100	100

Element	Wt %	At %
O K	16.84	49.53
Y L	1.5	0.79
BaL	47.75	16.36
TiK	33.91	33.31
Total	100	100

Element	Wt %	At %
O K	8.79	31.54
Y L	3.06	1.98
BaL	50.13	20.95
TiK	38.01	45.54
Total	100	100

Element	Wt %	At %
O K	14.28	43.3
Y L	2.35	1.28
BaL	43.96	15.52
TiK	39.41	39.9
Total	100	100

Element	Wt %	At %
O K	15.35	46.99
SrL	1.53	0.86
Y L	1.33	0.73
BaL	48.4	17.26
TiK	33.4	34.16
Total	100	100

Figure 31. SEM micrographs and corresponding EDS spectra of a) BSrT, b) BYT, c) BTY, d) BYTY, and e) BSrTY accordingly.

Table 10. The average Grain size of the BSrT, BYT, BTY, BYTY, and BSrTY compounds

Samples	Grain size (µm)
BSrT	4.1
BYT	3.7
BTY	3.3
BYTY	0.9
BSrTY	0.5

5.5. Optical study

UV–Visible Diffuse reflectance spectra of BSrT, BYT, BTY, BYTY, and BSrTY ceramics recorded in the range of 300–1000 nm are shown in Figure 32. The ceramic samples show an important behavior of visible photons absorption with an absorption maximal of 40% in the wavelength region above 400 nm for the BSrTY sample. The UV spectra of the BSrTY ceramic sample suddenly decrease as a result of the absorption of the visible photons. All the ceramic samples exhibit three separate peaks in the visible region of the spectra, regardless of the Sr and Y sites' occupancy. Moreover, the preference of Sr and Y sites in the BT lattice has a small impact on photon absorption. Indeed, the K-M (Kubelka-Munk) mode monitoring of the diffuse reflectance data was also employed to estimate the optical band gap of the prepared samples.

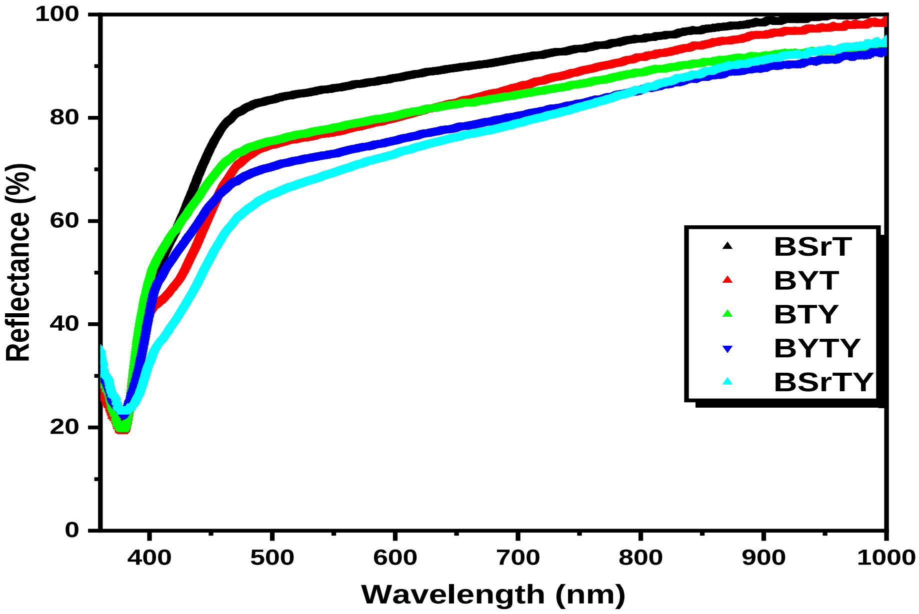

Figure 32. Reflectance spectra of the as-prepared ceramic samples

The optical band gap energy (E_g) of BSrT, BYT, BTY, BYTY, and BSrTY ceramic samples was determined with the help of the Kubelkae-Munk method [142]. The Kubelkae-Munk equation is assigned by the following formula:

$$F(R) = \frac{(1-R)^2}{2R} = \frac{k}{S} \tag{23}$$

Where F(R) is the Kubelkae-Munk function or the diffuse reflectance of the low-absorbing standard and $R = R_{sample}/R_{reference}$, S is the scattering coefficient, and k is the coefficient of molar absorption of each ceramic sample. The optical band gap Eg of a semiconductor is estimated by;

$$\alpha h\nu = C_1(h\nu - E_{gap})^n \tag{24}$$

Where hν is the photon energy, E_{gap} is the band gap, α is the linear absorption coefficient of a material, n is a constant (n = 1/2 for indirect allowed and n = 2 for direct allowed), and C_1 is a proportionality constant. In this case, photon absorption may stimulate an indirect electronic transition from the bottom of the valence band to a top state in the conduction band. This approach takes place in any region of the Brillouin zone. According to this fact, the optical band gap of all the ceramic samples was calculated and estimated using n = 1/2 in Eq. (24). Finally, using Eq. (23) and with k=the chan2α, we obtain the Kubelkae-Munk modified equation as presented below;

$$[F(R)h\nu]^2 = C_1(h\nu - E_{gap}) \tag{25}$$

Eg values of BSrT powders can be determined with better precision from the plotting of $[F(R)h\nu]^{1/2}$ vs. $h\nu$. The optical band gap energy (Eg) values are 2.97 eV, 3.04 eV, 3.01 eV, 3.03 eV, and 2.74 eV for BSrT, BYT, BTY, BYTY, and BSrTY, respectively (see Figure 33). In BSrTY material, the conduction band's bottom may gradually be narrow with doping 7.5%Sr in Ba-site and 7.5%Y in Ti-site, resulting in a significantly low band gap energy value compared to the other materials that are doped with only one element (Sr or Y but not both). Moreover, this variation may be due to the changes in the lattice parameters. Tian et al. [174] demonstrated that the BO6 octahedron controls both the top-lying of the valence band and the bottom-lying of the conduction band. The lower-lying conduction states in the structure are influenced by other ions, but these hypotheses typically have only a small impact on the optical characteristics of a certain material. Hence, it may be noted that Ba/Sr ratio has a significant role in the unit cell distortion process. This distortion induces a defect in the band structure, which lowers the intermediate levels in the band gap region which can be observed from the samples that are mainly doped with Sr content (BSrT and BSrTY). Urbach energies (Eu) have also been estimated for each prepared sample. The sample disorder, which may result from chemical, thermal, polar, or structural flaws, is reflected by the parameter Eu. The relationship between the photon energy and the absorption coefficient at the Urbach edge is given by the following equation [175]:

$$\alpha(E) = \alpha_0 . \exp\,(\frac{E}{E_u}) \tag{26}$$

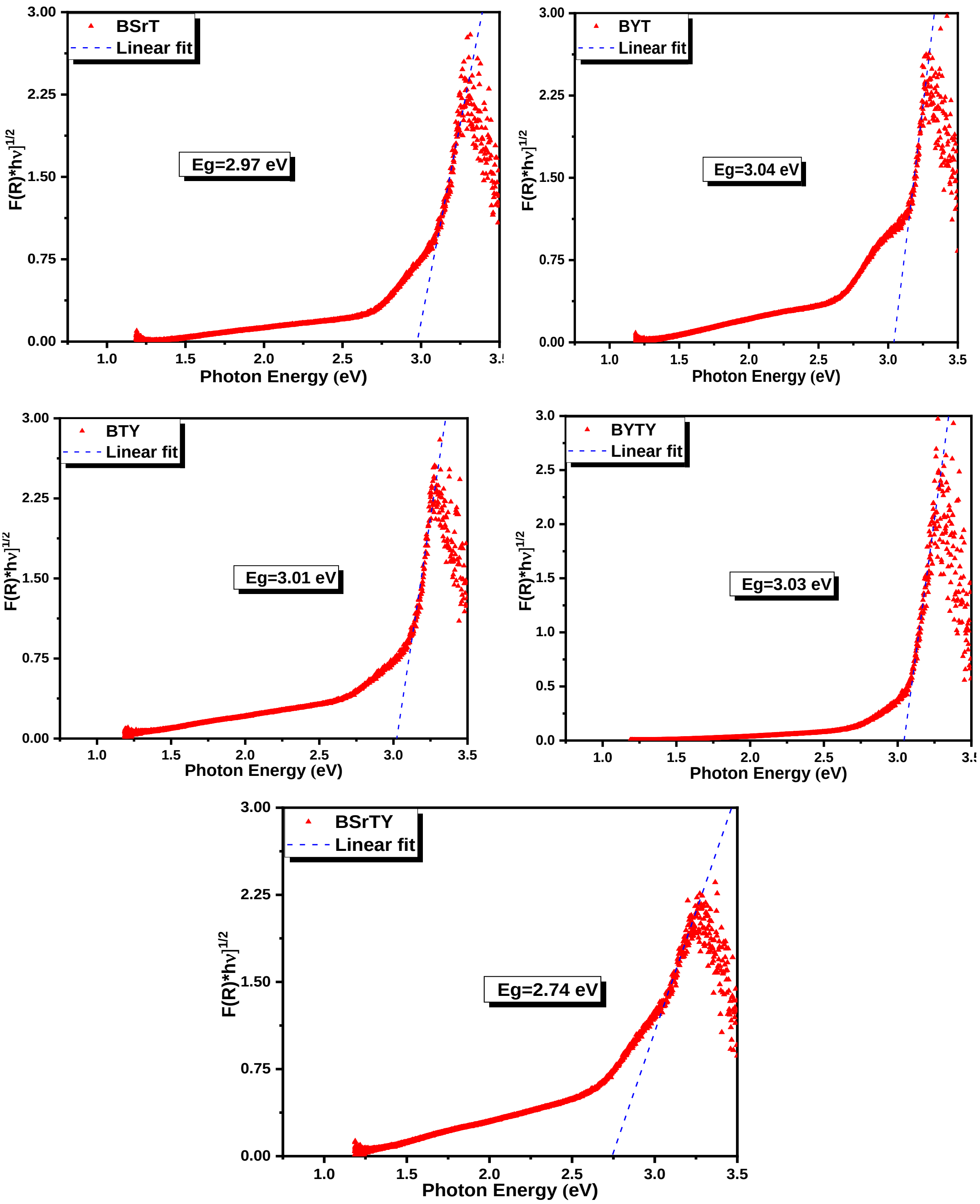

Figure 33. The plot of [F(R)hν]1/2 vs. (hν) for estimating the optical band gap of BSrT, BYT, BTY, BYTY, and BSrTY samples.

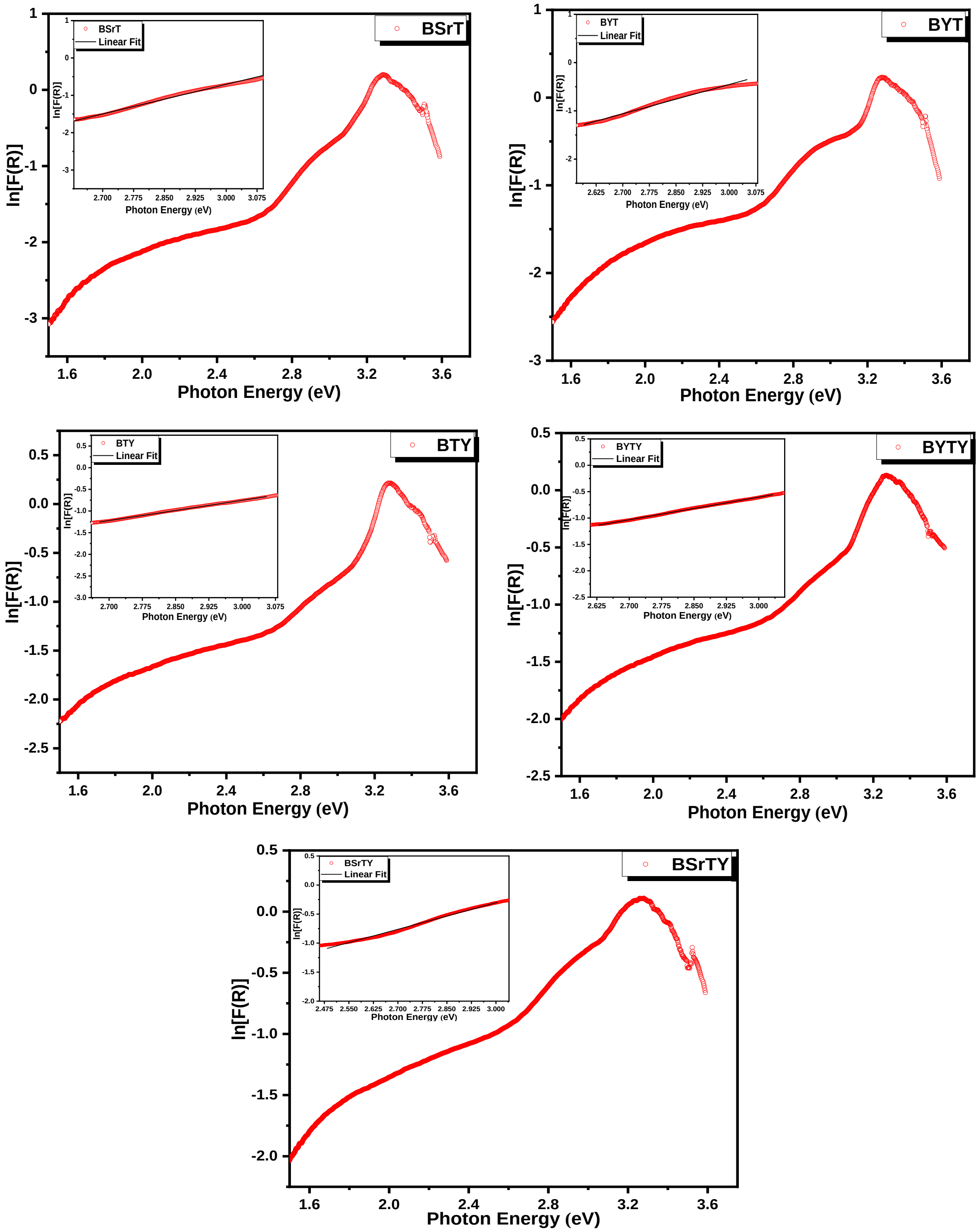

Figure 34. The plot of ln αvs. hν for determination of the Urbach energy (Eu) for BSrT, BYT, BTY, BYTY, and BSrTY ceramics

Where E_u is the Urbach energy, hν is the photon energy, α_0 is a constant, and which is weakly affected by temperature.

Since the absorbance is proportional to the absorption coefficient and F(R), accordingly, α can be replaced by F(R). Consequently, we can generally write $F(R) \sim \exp\left(\frac{E}{E_u}\right)$. The Urbach energy is determined by extraction lnF(R) vs. (hν). The value of Urbach energy is determined by the fitted lines of the linear slope using the provided equation;

$$\ln F(R) = C + \frac{E}{E_u} \qquad (27)$$

The Urbach energy value was estimated by projecting the linear portion of the curve ln(α) as a function of hν; the Urbach energy was determined and plotted as shown in Figure 34. It can be observed from the figure that The Urbach energy E_u varies inversely to the behavior of the optical band gap and hence noting the important role played by Y^{3+} and Sr^{2+} ions in generating disorder in the presented ceramic samples. The relationship of the Urbach energy with the band gap and the schematic illustration of the Urbach energy for the as-prepared samples are shown in Figure 35.

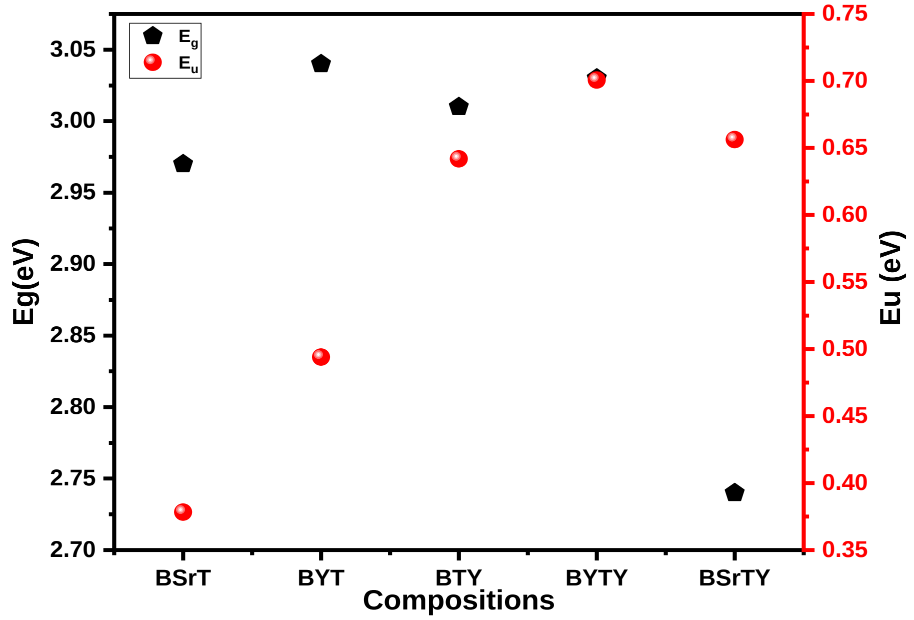

Figure 35. Urbach energy (Eu) and Band gap energy (Eg) variations for different ceramic compounds

5.6. Thermal conductivity

Table 11 presents a summary of the thermal conductivity measurements of the BT, BSrT, BYT, BTY, BYTY, and BSrTY ceramics recorded at 25 °C and 180 °C. The reported values of the thermal conductivity for undoped $BaTiO_3$ were found to be in the region of 1.2 to 6.5 $Wm^{-1}K^{-1}$ at ambient temperature [124]. The variation in the behavior of thermal conductivity can be due to different synthesis processes used to prepare perovskite ceramics, different measurement techniques, and the type of dopants modified in a given material. Typically, the contributions of lattice thermal conductivity and electrical thermal conductivity are added to determine the overall thermal conductivity. [178] In this work, the standard thermal conductivity at room temperature carried out on undoped barium titanate ceramic is 2.23 $Wm^{-1}K^{-1}$ which is exactly along the region of the obtained results from the literature [24], [88]. Therefore, when materials' thermal conductivities are tested in powdered form, they are much lower than in bulk form-by up to an order of magnitude. The heat transfer efficiency in powders is highly reliant on the packing density, interface, contacts, porosity, and composition of the particles. The thermal conductivity for undoped BT is decreased with Sr and Y dopants content and found to be in the range of 085-2.23 W.m^{-}1. K^{-1} at room temperature and decreases slightly with increasing temperature from 0.73-2.02 W.m^{-}1. K^{-1}. This change is due to the variation in the strength of the atoms' bonds [126]. Indeed. Sr and Y doped samples show a systematic decrease of the thermal conductivity with doping and increasing temperature, indicating that the phonon–phonon scattering is dominant in the considered temperature range. The thermal conductivities of the Sr, Y co-doped samples are lower and become less dependent on the temperature. This is caused by the relative increase of the temperature-independent phonon–impurity scattering. The amount of the thermal conductivities is, BSrTY<BYTY<BTY<BYT<BSrT for the doped samples, which is the same sequence as that of the lattice parameters. Abeles showed that the reciprocal of relaxation time of phonon–impurity scattering is proportional to the difference between the dopant and matrix ion of both the ionic radius and the mass [179]. The Y ion has a slightly smaller ionic radius than Sr [180] and has less than half of the atomic mass of Sr, which indicates the phonon–impurity scattering is mainly produced by the lattice distortion caused by the difference in ionic radii, not by the mass difference Therefore, thermal conductivity decreases with the decrease of ionic radius, and then, reaches a lower limitation when the ionic radius is small enough. The ionic radii of all these doped elements are smaller than that of the Ba ion (1.61Å). The smaller the ionic radius is, the larger the difference between the doped ion and Ba and/or Ti ion would be, which might introduce larger distortion into the lattice and thus reduce the lattice thermal conductivity. To retain the lattice structure, such distortion cannot be introduced infinitely, resulting in the lower limitation of the thermal conductivity value which is the case for BYTY and BSrTY co-doped samples. Further, the reduction between Ti-O bonds made the bond slightly strong. These variations in the bond tendency's strength are more effective for thermal conductivity in the system than the scattering of the point defect. In addition, from the SEM micrographs (Figure 31), the surface of the analyzed samples showed a structure unavailable to small pores. The thermal conductivity decreases as the surface complexity of the particles increases. All the samples have sizable micropores, which resulted in low heat conductivity values.

Table 11. Thermal conductivity of the as-prepared samples

Sample	Thermal Conductivity (W/mK)	
	25 °C	**180 °C**
BT	2.23	2.02
BSrT	1.32	1.05
BYT	0.90	0.90
BTY	0.95	0.85
BYTY	0.60	0.35
BSrTY	0.85	0.73

5.7. Mechanical properties

Figure 37 displays the compressive strength of the BT, BSrT, BYT, BTY, BYTY, and BSrTY ceramics recorded. It can be observed from Figure 37 that the compressive strength value of the as-prepared ceramic samples is 32.91, 30.2, 30.2, 30.01, 29.6, and 28.09 MPa for BT, BSrT, BYT, BTY, BYTY, and BSrTY, respectively, however, the compressive strength results revealed irrelevant changes when using Sr and Y dopants in $BaTiO_3$. The strength of the cohesion between the grains of the ceramic compounds, in addition to the shape and the particle sizes, mainly depends on the pores, the separation of the particles, and shrinkage. High compressive strength results from the irregular grain shape distribution that is nearly attached to the particles [127]. The higher compressive strength value observed (32.91 MPa) was probably due to the shape of the irregular flat block grains forming, which greatly weakened the atom bonds. Additionally, based on the scanning electron microscopy examination, the microstructure of Sr, Y doped-co-doped $BaTiO_3$ samples differs significantly. For flat blocks of BSrTY (0.5 µm average grain size), the measured values of the pores' diameter have pores that are barely identical in shape and size, which are in both cases in flat block form. Further, the pores in undoped $BaTiO_3$, which has a larger particle size, are likewise larger and have a shape of a flat block. The highest value of the compressive strength was found for undoped $BaTiO_3$ material corresponding to the higher grain size, whereas, the minimum value was 28.09 MPa for BSrTY compound.

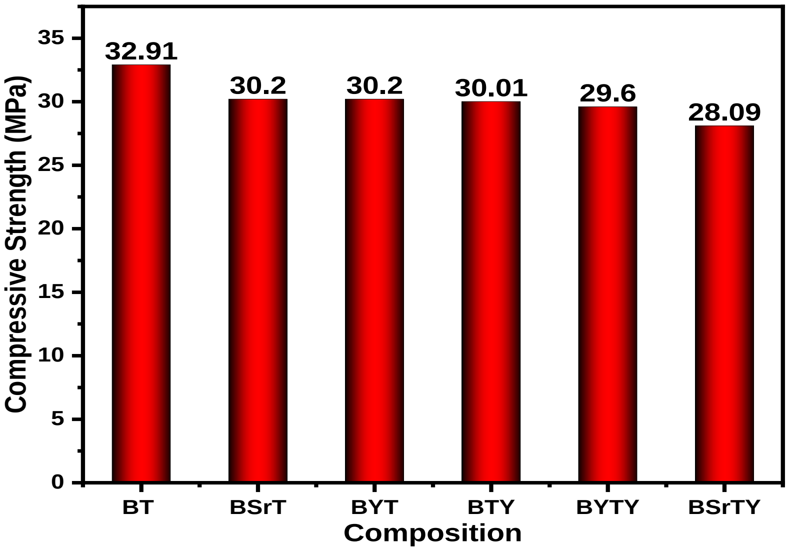

Figure 36. Histogram of the compressive strength of the as-prepared BSrT, BYT, BTY, BYTY, and BSrTY samples

6. Results and Discussion on $Ba_{0.85}Sr_{0.15}TiO_3$/Cu new composites: via sol-gel and spark plasma sintering

6.1 Phase analysis using XRD

The XRD patterns tested at room temperature of BST-Cux (x=0, 5, 12.5, 15, 20, 30, and 40%) composites sintered at a low temperature of 950 °C are shown in Figure 37a. All peaks were attributed to either the BST phase or Cu without any impurities being observed, suggesting that no reaction took place between BST and Cu during the SPS sintering process. Furthermore, the diffraction peaks of BST in the composites did not shift, indicating that the copper was not incorporated in the perovskite structure. As expected, the relative diffraction intensities of the Cu reflections compared to the ones of BST increased with the increase of Cu content (Figure 37b). The evolution of the XRD-peaks confirms the successful composition control during sintering. Additionally, the crystal structure of BST-Cu samples has been proved to be multiphase coexistence of cubic and tetragonal phases at room temperature [181], while the phase of BST as mentioned above is a tetragonal structure.

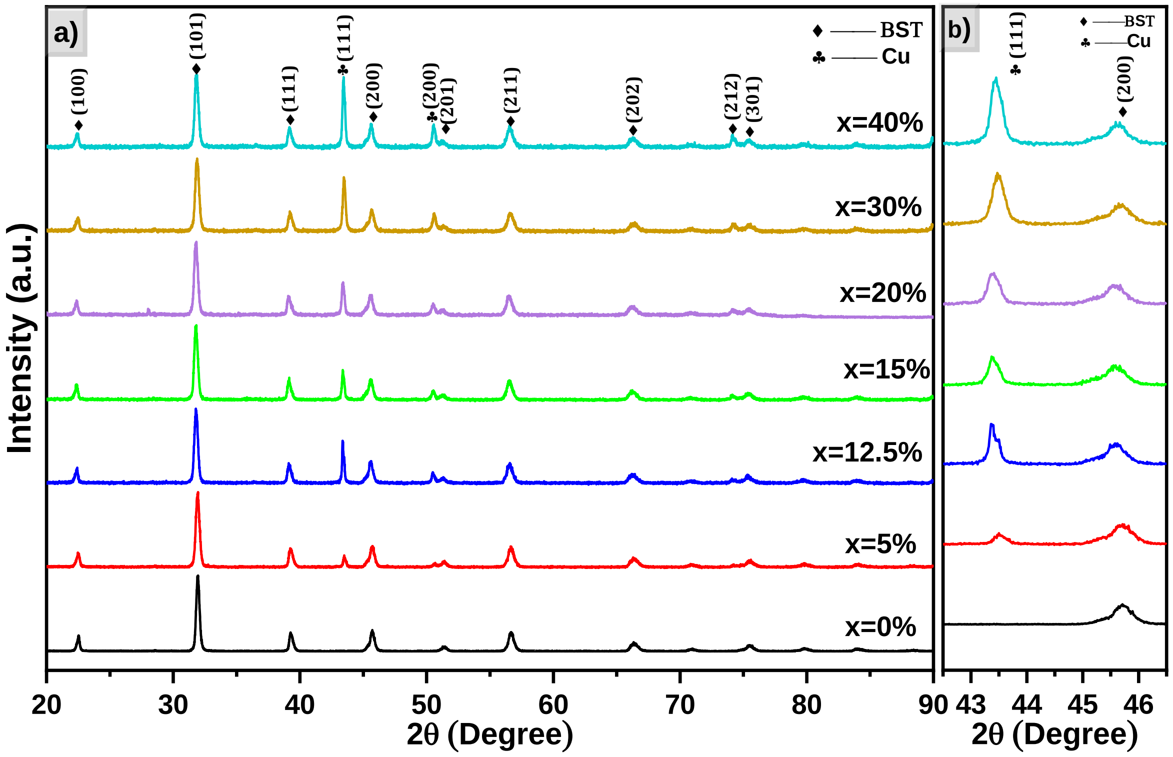

Figure 37. (a) XRD pattern of BST-Cux (x=0-40%) ceramic-metal composites (b) Shifting of the peaks BST (200) and Cu (111)

6.2 FT-IR analysis

The Fourier transform infrared spectroscopy (FT-IR) spectra of BST-Cux (x=0, 5, 12.5, 15, 20, 30, and 40%) composites in the wavenumber range from 450 to 4000 cm^{-1} are displayed in Figure 38. These spectra show three sets of absorption bands. The first one is characterized by a wide band in the low-frequency range from 460 cm^{-1} to 723 cm^{-1}, associated with the vibrations of the TiO_6 octahedron. Moreover, all the samples show the molecular fingerprint of BST as revealed by the Ti-O and Ti-O-Ti bonds between 460 cm^{-1} and 601 cm^{-1}. The absorption peaks for the same mode BST-Cux (x=0, 5, 12.5, 15, 20, 30, and 40%) were obtained at around 470-480 cm^{-1}. The incorporation of Sr into the BaTiO$_3$ lattice moved the characteristic peak of Ti-O to higher energy values. In our samples, the incorporation of Sr^{2+} ions into Ba^{2+} and Ti^{4+} sites influenced the binding distance between Ti^{4+} and O^{2-} ions resulting in a high binding strength [172], [173]. On the other hand, a clear band absorption was observed at around 1061 cm^{-1} which is due to bond characteristics related to ceramic-metal bonding in our case BST ceramic with copper metal, Ba-Cu, and Ti-Cu as well as Ti-O-Ti-Cu. In addition, the bands observed in the region from 1430 cm^{-1} to 1550 cm^{-1} could be attributed to symmetrical and antisymmetric vibrations (stretching of carboxyl groups bound to barium and/or titanium (COO^{-})). The results we obtained are therefore in good agreement with those of the literature [172]. The observations made on infrared spectra agree well with those revealed by XRD analysis.

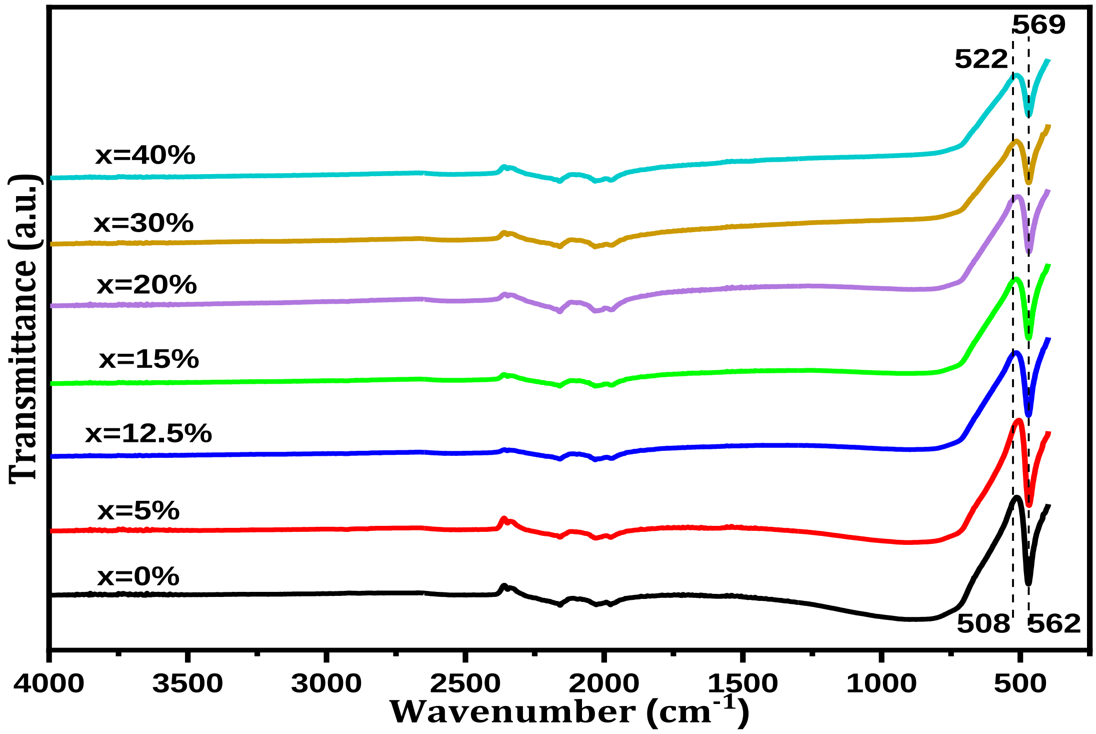

Figure 38. FT-IR spectra of the BST-Cu$_x$ (x=0, 5, 12.5, 15, 20, 30, and 40%) composite sample

6.3 SEM Investigation

The SEM micrographs of the BST-Cux composites with different content of Cu (x = 0, 5, 12.5, 15, 20, 30, and 40 wt.% are shown in Figure 39. The shapes of the grains were also irregular. With increasing the Cu content, the reaction between BST and Cu increased, and consequently the amount of intermediate phases increased. It was seen in Figure 39(d-g) that abnormal grain growth was clearly observed. The normal grain size of pure BST was about 3.1µm, while the abnormal grain size of BST-Cu composites was about 3.1-5.2µm. Abnormal grain growth was generally known to occur when particle shape was angular in the presence of a liquid phase during sintering [182]. It is indicated that the low eutectic liquid phase formed between Cu and BST during sintering promoted grain growth [183]. In Figure 39(c), lots of big spheroidal copper particles stood in the BST matrix. That is the Cu agglomerated with an increasing amount of Cu. The coalescence of Cu may be caused by pores, which also contributes to the decrease of relative density of BST-Cu composites with the increasing amounts of Cu. And the spheroidal copper particles on the surface of BST matrix (Figure 39(d-g)) were identified as Cu by EDS analysis. Figure 39a shows an agglomeration with a high degree of porosity in the synthesized sample. This agglomeration may have resulted due to the high surface-to-volume ratio. Similarly, Figure 39b shows SEM micrographs of BST-Cu5% material, where round-shape grain size distribution of the prepared ceramics has been noticed. Table 12 contains the grain size variation with different amounts of Cu metal. The grain size has increased with the increase in the copper content, which is also consistent with the XRD observations of this research. SEM micrographs of the prepared materials indicate the decreasing porosity with the increase in Cu content, which is also evident from the XRD measurements. The porosity of the prepared samples may be susceptible for hydroelectric cells application.

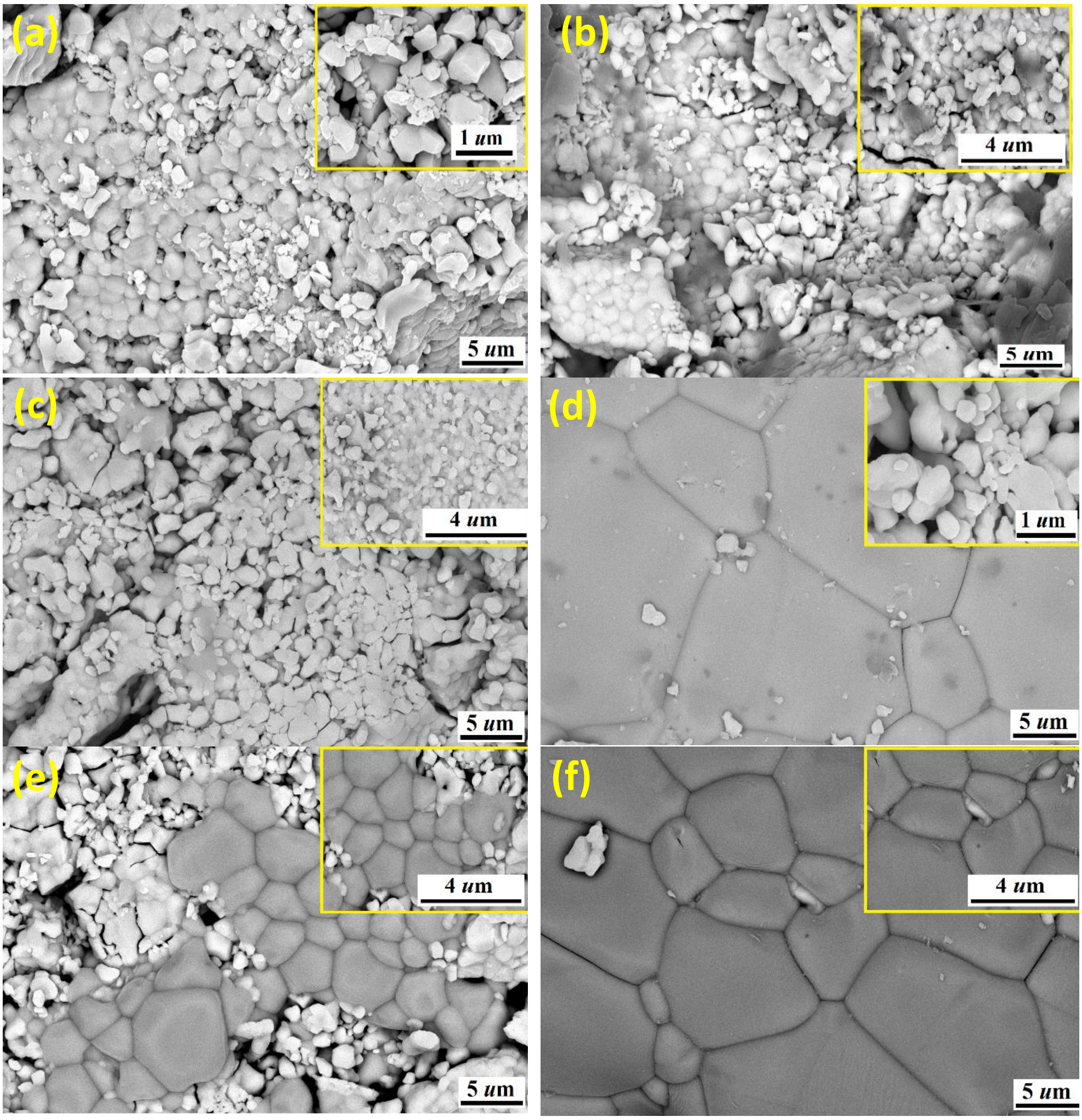

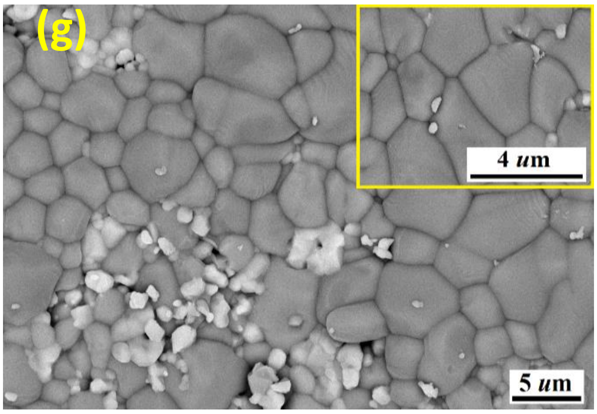

Figure 39. FESEM micrographs of the ceramic samples (a) BST, (b) BST-Cu5%, (c) BST-Cu12.5%, (d) BST-Cu15%, (e) BST-Cu20%, (f) BST-Cu30%, (g) BST-Cu40%

The EDS spectra and elemental mapping images for BST-Cu composite ceramics with the marked spectral positions of the individual elements are displayed in Figure 40. It can be seen that qualitative EDS examination confirms the lack of any traces of contaminants (secondary carbon, etc.) in analyzed samples. Thus, the EDS analysis, together with the elemental mapping, confirmed the good stoichiometry of the ceramics and the uniform distribution of the elements. The elemental mapping and EDs were carried out, which confirms the existence of elements like Ba, Ti, O, Cu, O, and Ti in the selected samples (Figure 40).

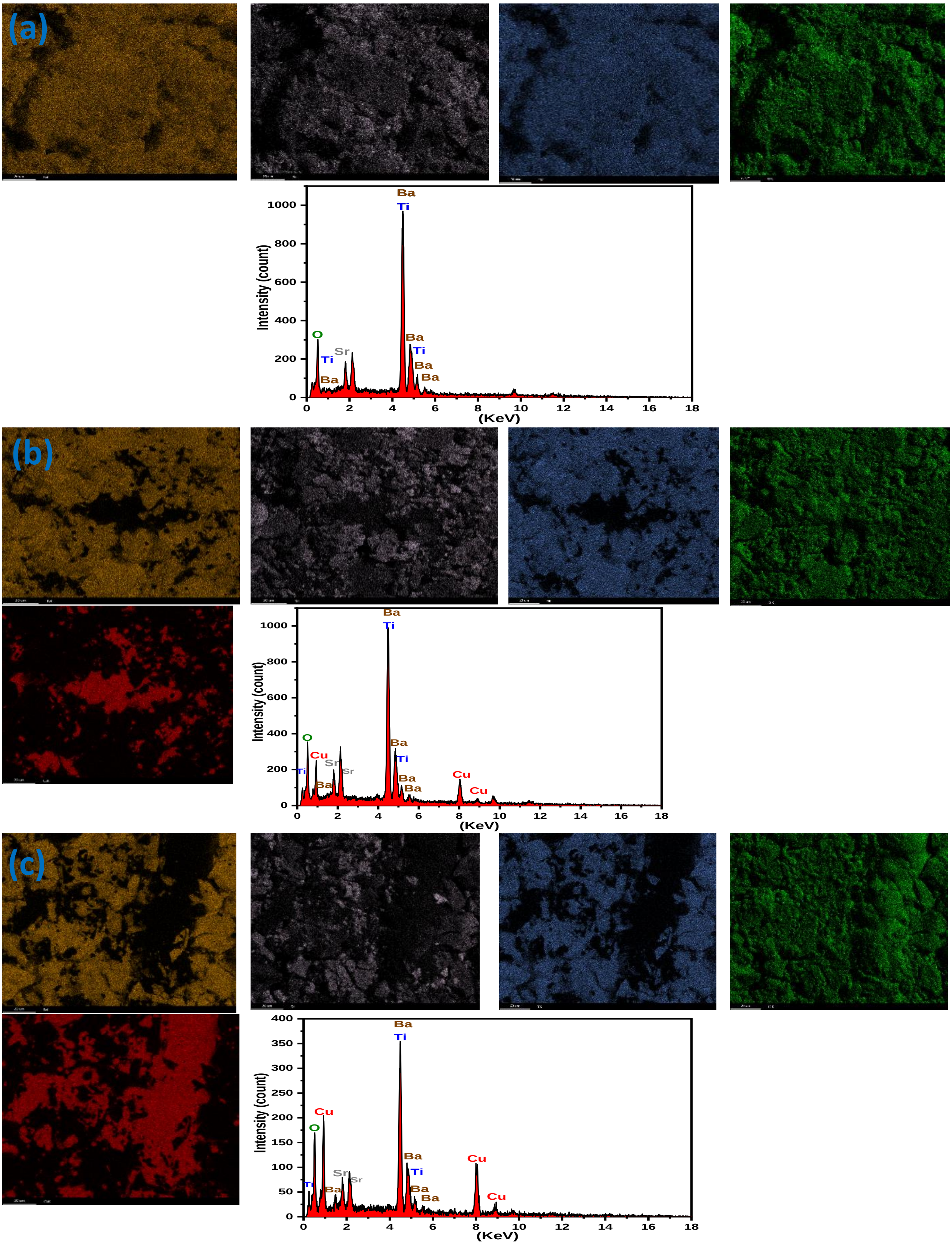

Figure 40. EDS and elemental mapping of (a) BST, (b) BST-Cu15%, (c) BST-Cu40%

Table 12. The average Grain size of the as-prepared composites

Samples	Grain size (μm)
BST	3.1
BST-Cu5%	3.4
BST-Cu12.5%	3.9
BST-Cu15%	4.1
BST-Cu20%	4.5
BST-Cu30%	4.7
BST-Cu40%	5.2

6.4 Optical characteristics

The correlation between crystalline structure and physical properties in perovskite materials is very delicate. Small changes in the structure can induce major variations in their physical and optical properties. The optical behavior is analyzed employing UV Visible absorption spectroscopy. Diffused reflectance UV–vis spectra of pure and BST-Cu composites measured in the range of 350–800 nm are shown in Figure 41. Samples with copper content exhibit inquisitive behavior of absorbing the visible photons in the region above 400 nm with maximum absorption of 45% for highly Cu content. This absorption of visible photons results in a sudden fall in the UV spectra of BST-Cu samples. Irrespective of the Sr site occupancy all the doped samples show three distinct peaks in the visible region of the spectra. Site preference of Cu in BST lattice has a slight influence on the absorption of photons.

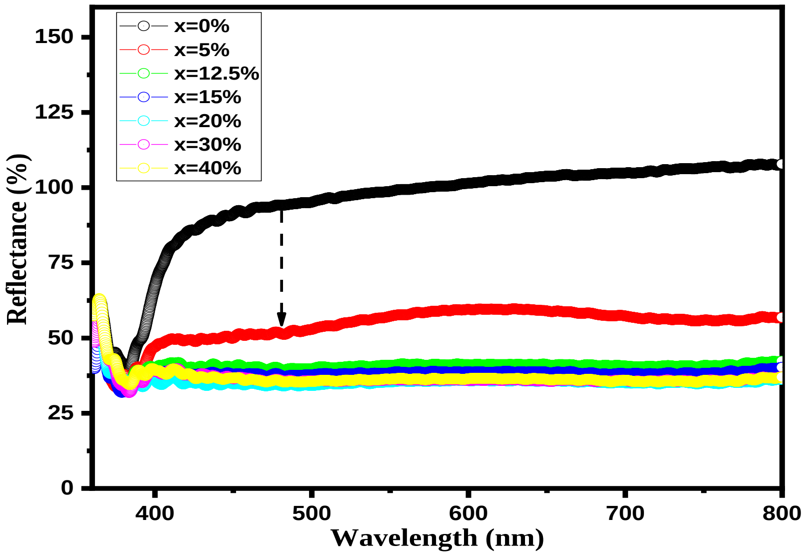

Figure 41. Diffused reflectance spectra of BST-Cux (x=0-40%) samples

The optical band gap energy (E_g) of BST-Cux (x = 0-40%) samples was determined using the Kubelkae-Munk (K–M) method, the latter was used to extract E_g values, as well as the stimulation of the measured diffuse reflectance at a high accuracy [142].

As demonstrated in Figure 42 and listed in Table 13 the Eg values of BST-Cux (x=0, 5, 12.5, 15, 20, 30, and 40%) obtained by extrapolating the linear part to the horizontal axis are in the range of 3.10 and 2.01 eV which are considerably lower than that of the BST (3.10 eV). Among them, the band gap reduction of BST-Cu30% (Figure 42(f)) is the most evident and is even more significant than those of other photovoltaic perovskite ceramics [143], [144].

These optical behaviors can be explained by the newly emerging electronic states of the highest energy band that is occupied by electrons (VBM) and the next highest energy band above the valence band that is unoccupied (CBM) generated by Sr^{2+} cation doping. In BST, the VBM is around the O 2p orbital, which has a slight interaction with the Ti 3d and Ba 6p orbitals, whereas the CBM is around the Ti 3d orbital [145]. The position of the conduction band depends on the electronegativity of the doping ions; the greater the electronegativity of the ions, the lower the conduction band [146]. When the doping element is introduced, the VBM is localized around the Ti 3d orbital. As the Ti cations are more electronegative than Ti, the energy of the Cu 3d orbital is lower than that of the Ti 3d orbital. Hence, there is a downward shift of the conduction band edge into the band gap, resulting in the reduction of Eg. Moreover, according to Choi's report [147], in addition to electronegativity, the optical band gap may be related to the lattice distortion caused by the ion substitution. The lattice distortion increases as the radius of the doping ions decreases, which leads to a rearrangement of the molecular orbital and a reduction in the band gap. According to the experimental data analysis, copper may be the preferred element to reduce the band gap of BST material. These results indicate that we can effectively reduce the band gap of BST ceramics via copper reinforcement to improve their properties for visible and ultraviolet absorption. We believe that optimizing the Cu concentration can further modify the band gap of BST ceramic material. Consequently, all the above-presented results indicate that the optical properties of BST-Cux (x=5, 12.5, 15, 20, 30 and 40%) ceramics can be regulated, demonstrating that the synthesized ceramics are good candidates for high performance multilayer ceramic capacitors.

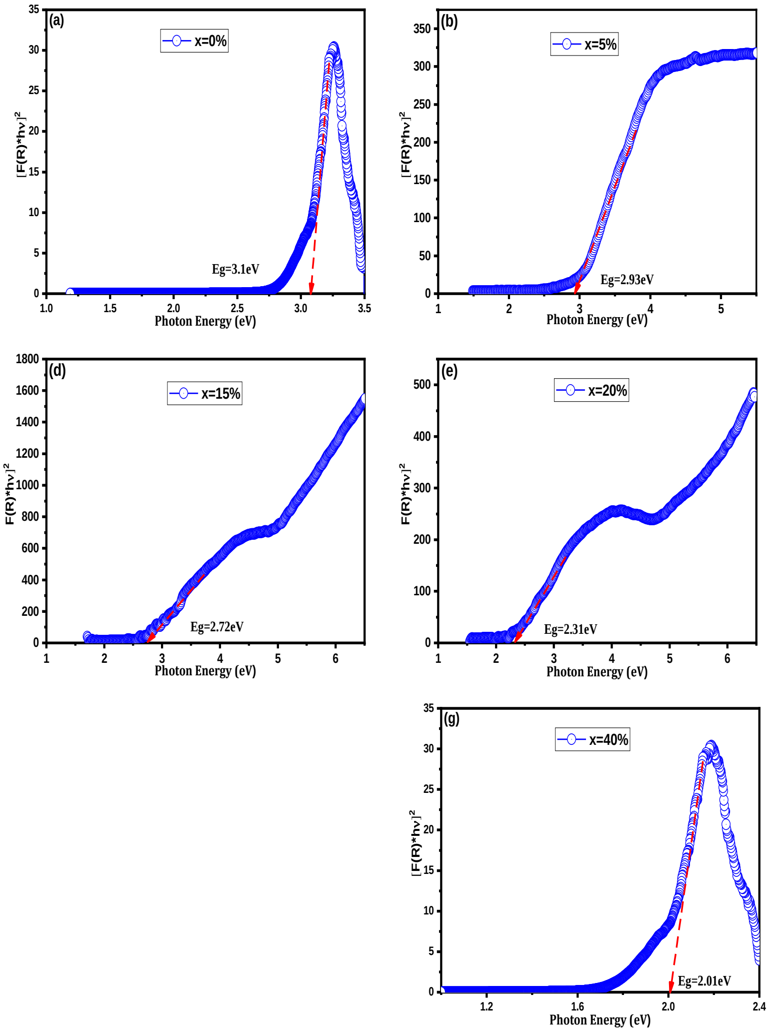

Figure 42. Band gap energy from Tauc plot of (a) BST, (b) BST-Cu5%, (c) BST-Cu12.5%, (d) BST-Cu15%, (e) BST-Cu20%, (f) BST-Cu30%, and (g) BST-Cu40%

Table 13. Band gap value of BST-Cu$_x$, (x=0-40%)

Sample (% wt.)	Band gap value (eV)
x=0.00	3.10
x=5	2.93
x=12.5	2.85
x=15	2.72
x=20	2.31
x=30	2.21
x=40	2.01

6.5 Electrical conduction mechanism in BaTiO$_3$–Cu composites

The graph in Figure 43 illustrates the change in the real part of AC conductivity (σ′) concerning frequency at room temperature, considering various additions of Cu. The AC conductivity shows a gradual increase with rising Cu concentrations up to 30 wt%, followed by a decline as the Cu content continues to increase. This shift in conductivity is attributed to fluctuations in the concentration of charge carriers within the composites. As the Cu content surpasses a specific threshold (percolation threshold), the concentration of charge carriers decreases due to the emergence of the Cu liquid phase during sintering. This phenomenon aligns with the apparent density variations in the composites with different Cu contents. The percolation threshold for BST-Cux is identified at x = 30 wt%. At lower frequencies, a distinct plateau, more pronounced in samples with higher Cu contents than lower ones, reflects the direct current conductivity (σ_{dc}). Conversely, at higher frequencies, a dispersive region, known as the "universal dielectric response" (UDR), becomes evident. This can be approximately characterized as follows [184]:

$$f_m = \frac{1.8 \times 10^{12}}{\varepsilon \rho} \tag{28}$$

In this context, the dispersive frequency fm is defined as the point at which the transition from the plateau-type region of direct current conductivity σ_{dc} towards the dispersive region occurs. The permittivity (ε) represents the ceramic's ability to permit the flow of electric field at low frequencies, while the resistivity (ρ) indicates the resistance of the ceramic. Observations suggest that as the Cu content increases (resulting in a decrease in resistivity, ρ), there is a corresponding shift in the threshold frequency. This shift denotes the point at which the transition from the plateau-type region of σ_{dc} towards the dispersive region occurs, and it moves towards higher frequency values.

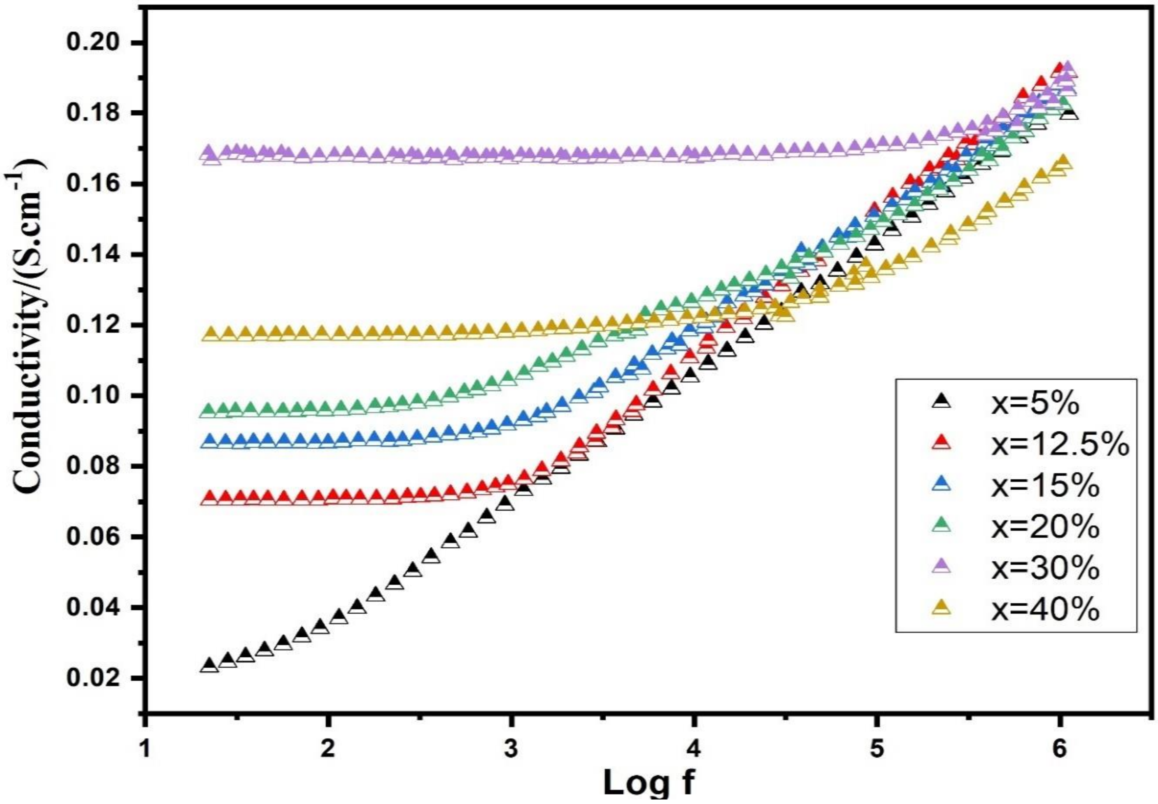

Figure 43. Frequency-Dependent modulation of AC Conductivity (σ′) with varying Copper additions at Room Temperature

The temperature dependence of conductivity in BST-Cu is illustrated in Figure 44 for different Cu additions. The graph further presents Arrhenius plots depicting the temperature dependency of conductivity specifically for BST-Cu composites with x = 30 wt%. Below the critical temperature (T_c) at 130°C, the conductivity exhibits an increase with rising measuring temperature, characteristic of semiconducting materials. Conversely, above Tc, the conductivity decreases, aligning with the behavior typical of conducting materials. This shift in conductivity is attributed to the distinct electrical conduction mechanisms inherent in semiconductors and conductors. As is widely known, semiconductors facilitate electrical conduction through the migration of electrons from the valence band across the forbidden energy band to the conduction band. An increase in temperature supplies the necessary energy for electrons to traverse the forbidden energy band, resulting in enhanced conductivity. In metals, electrons exhibit directional movement, forming electricity. However, at higher temperatures, the electrons experience more intensive scattering by metal atoms or ions, hindering their movement and causing a decrease in metal conductivity.

The transformation temperature, approximately at Tc, indicates a notable change in the composite's conductivity-temperature relationship, possibly linked to the ferroelectric-paraelectric phase transition. During this transition, a shift in carrier mobility occurs, leading to a transformation in conductivity around Tc. The significance of phase change, rather than adhering to a semiconductor-metal model, is emphasized in the BST-Cu composite. This perspective is supported by the well-known observation of conductivity abnormalities around Tc, a phenomenon also evident in pure BST. Consequently, the phase change holds greater importance than the semiconductor-metal model in understanding the behavior of the BST-Cu composite.

The relationship between conductivity and temperature below 130°C adheres to an Arrhenius-type correlation, as depicted in Figure 44,

$$\sigma = \sigma_0 \exp\left(-\frac{E_a}{K_{B.T}}\right) \tag{29}$$

Here, E_a represents the activation energy of conduction, k_B is Boltzmann's constant, T is the absolute temperature, and σ_0 is the pre-exponential factor. Consequently, the activation energy for conduction was determined to be 0.18 eV below 83°C and 0.13 eV between 83°C and 130°C. The points of inflection in the temperature-conductivity characteristic at 83°C and 130°C are denoted in Figure 4. It is noteworthy that the activation energy in all samples was significantly smaller than the band gap for intrinsic electronic conduction in BST (≈3.1 eV), indicating the dominance of extrinsic conduction mechanisms associated with defects. Berglund and Braun demonstrated that impurity states, approximately 0.2–0.3 eV below the conduction band, were linked to oxygen vacancies and band conduction[185] . The BST-Cu composites in our study were typically sintered in using spark plasma sintering. As a result, the sintering process under low oxygen partial pressure likely generated a certain amount of oxygen vacancies.

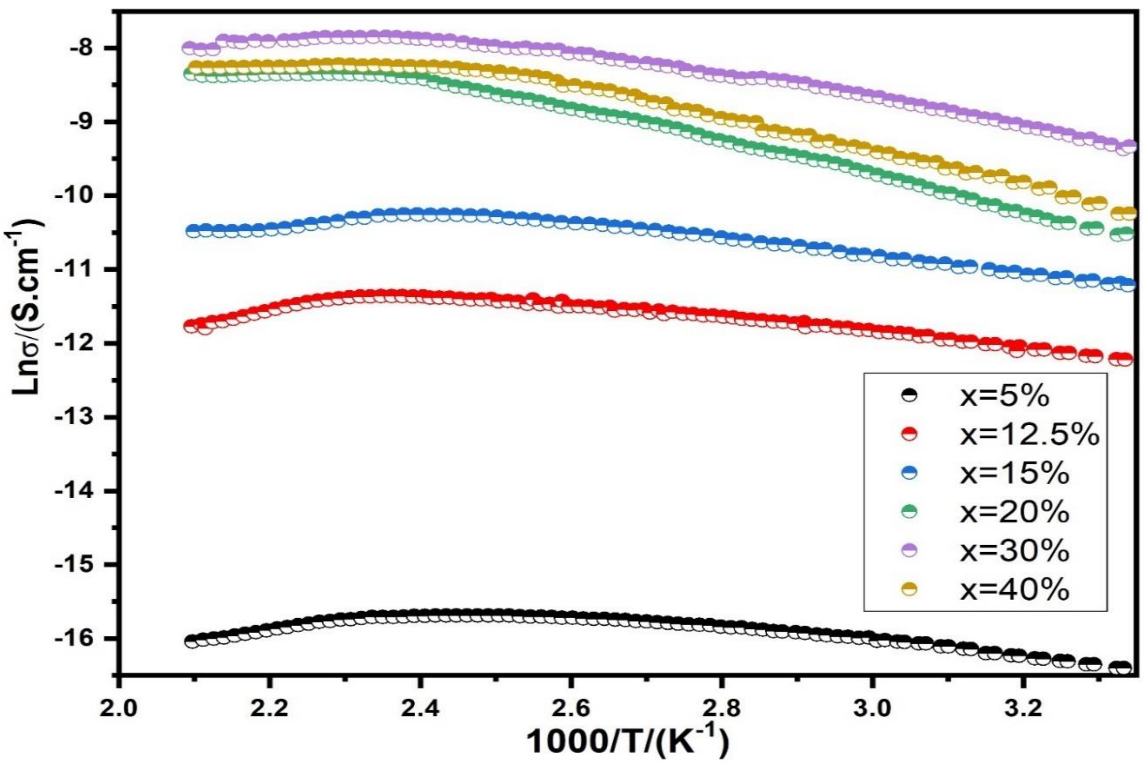

Figure 44. The temperature dependence of the conductivity for different Copper Content.

Figure 45 depicts complex plane plots for impedance, denoted as Z*, in the BST-Cux composites. These plots illustrate the relationship between the imaginary part (Z′′) and the real part (Z′). Typically, in the case of a flawless crystal, the resistance (R) and capacitance (C) values are examined using an equivalent circuit consisting of a single parallel RC element. On the complex plane, this RC element manifests as a semicircular arc with intercepts at zero and R on the Z' axis. Consequently, C, can be determined using the formula ω_{max}RC = 1 where ω_{max} = 2πf$_{max}$ and fmax and fmax represents the frequency at the maximum point of the arc. For BST-Cu composites, the equivalent circuit is conceptualized as two parallel RC elements connected in series, resulting in the appearance of two arcs on the complex plane. One arc corresponds to the grain, and the other corresponds to the grain boundary of the BST-Cu response. The impedance can be calculated using the following approach:

$$Z^{*} = \frac{1}{R_g^{-1} + i\omega C_g} + \frac{1}{R_{gb}^{-1} + i\omega C_{gb}} = Z' - iZ'' \tag{30}$$

Where

$$Z' = \frac{R_g}{1 + (\omega R_g C_g)^2} + \frac{R_{gb}}{1 + (\omega R_{gb} C_{gb})^2} \tag{31}$$

And

$$Z'' = R_g \frac{\omega R_g C_g}{1 + (\omega R_g C_g)^2} + R_{gb} \frac{\omega R_{gb} C_{gb}}{1 + (\omega R_{gb} C_{gb})^2} \tag{32}$$

Here, (R_g, R_{gb}) and (C_g, C_{gb}) represent the resistance and capacitance values for grains and grain boundaries, respectively. Utilizing Eqs. (31) and (32), the responses emanating from grains and grain boundaries are positioned at $1/(2\pi R_g C_g)$ and $1/(2\pi R_{gb} C_{gb})$, respectively. The peak value of Z'' is directly proportional to the associated resistance. As depicted in Figure 45, it is evident that the Z'' peak value attributed to grain boundary responses surpasses that of grain responses. Consequently, across all examined samples, R_{gb} is significantly greater than R_g, and the R_{gb} diminishes with escalating Cu content, aligning with the observations in Figures 43 and 46. These outcomes are elucidated through a two-layer model, postulating the existence of conducting grains isolated by poorly conducting grain boundaries.

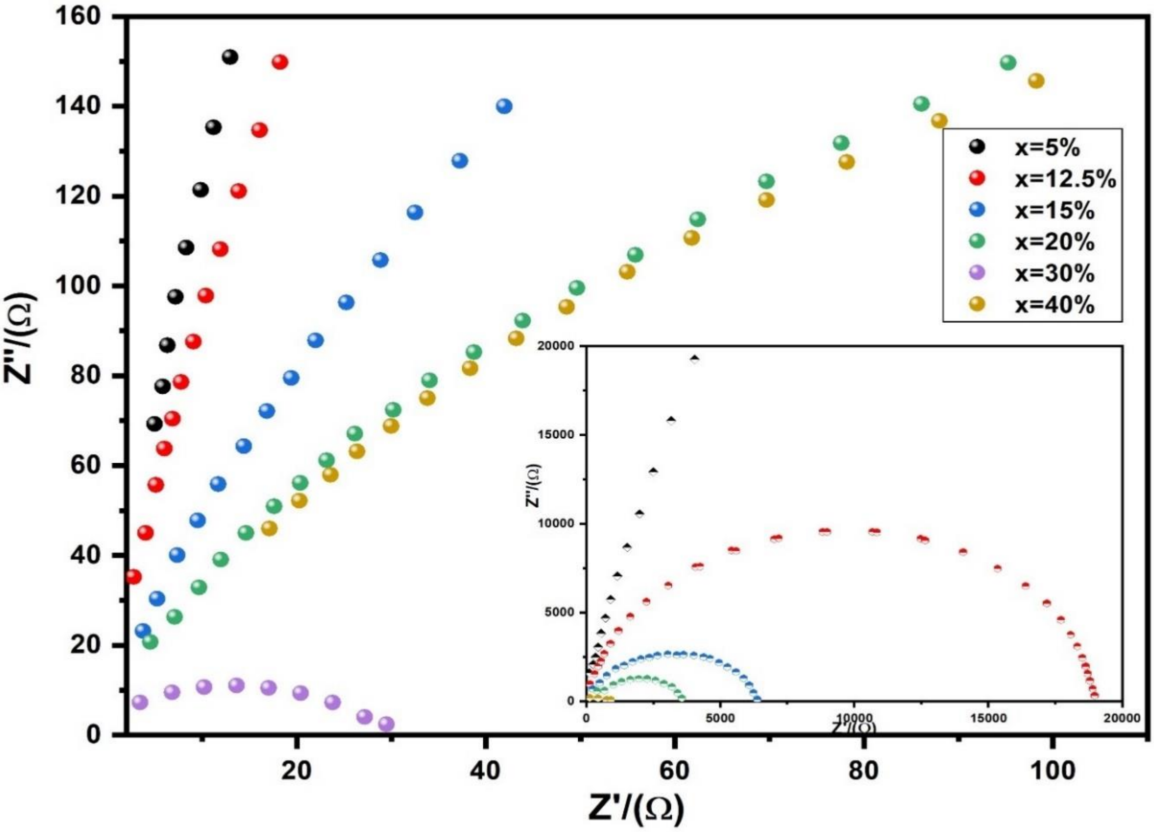

Figure 45. The expanded view of the low frequency and the equivalent circuit of the RC element. The inset represents the impedance complex plane plots for BST-Cux composites of x = 5, 10, 15, 20, 25, 30 wt%.

Figure 46 presents the frequency-dependent permittivity of BST-Cux composites at room temperature. For x = 5, 12.5, and 15 wt%, a subtle frequency dependency in permittivity was noted within the range of 100 Hz to 1 MHz, aligning with the observations in pure BST[186]. As Cu content increased, reaching x = 30 wt%, the maximum permittivity reached approximately 1.2×105 at 1 kHz. However, a noticeable decline in permittivity at low frequencies (around 104 Hz) emerged when x > 30 wt%, indicating a step decrease in permittivity at the frequency where tanδ exhibited a relaxation peak. This low-frequency behavior implies the potential influence of conduction mechanisms in the dielectric response of BST-Cu composites. Consequently, the results should be interpreted within the framework of the Maxwell–Wagner capacitor model. In this model, different phases are assumed to possess distinct conductivity, and the overall polarization effects are predominantly influenced by charge accumulation at noncontinuous interfaces within the dielectric. The real and imaginary components of relative permittivity and tan δ were computed using the following formula[187],

$$\varepsilon' = \varepsilon_{\propto} + \frac{\varepsilon_0 - \varepsilon_{\propto}}{1 + \omega^2\tau^2} \tag{33}$$

$$\varepsilon'' = \frac{(\varepsilon_s - \varepsilon_{\propto})\omega\tau}{1 + \omega^2\tau^2} + \frac{1}{\omega C_0(R_1 + R_2)} \tag{34}$$

$$tan\delta = \frac{(\varepsilon_s - \varepsilon_{\propto})\omega\tau}{\varepsilon_s + \varepsilon_{\propto}\omega^2\tau^2} + \frac{\sigma}{\omega\varepsilon_0}\left(\frac{1}{\varepsilon_0 + \frac{\varepsilon_s - \varepsilon_{\propto}}{1 + \omega^2\tau^2}}\right) \tag{35}$$

In the given equation, ε_s and $\varepsilon_{\propto}$ represent the static and high-frequency permittivity, respectively. τ denotes the relaxation time of the composites, ω is the angular frequency, C_0 signifies the capacitance of the empty cell, R_1 and R_2 stand for the resistances of the two dielectric components, r represents the conductivity of the composites, and ε_0 corresponds to the vacuum permittivity. Equation (33) mirrors the structure of the Debye relaxation equation, stated as follows [188],

$$\varepsilon' = \varepsilon_{\propto} + \frac{\varepsilon_0 - \varepsilon_{\propto}}{1 + \omega^2\tau^2} \tag{36}$$

$$\varepsilon'' = \frac{(\varepsilon_s - \varepsilon_{\propto})\omega\tau}{1 + \omega^2\tau^2} \tag{37}$$

$$tan\delta = \frac{(\varepsilon_s - \varepsilon_{\propto})\omega\tau}{\varepsilon_s + \varepsilon_{\propto}\omega^2\tau^2} \tag{38}$$

Evidently, ε'' and $tan\delta$ in the Maxwell–Wagner model deviate from Debye behavior. The examination of imaginary permittivity and tanδ in the composites reveals distinctions between Debye and Maxwell–Wagner behaviors. Debye relaxation solely accounts for the impact of relaxation polarization on dielectric loss, as evident in the inset illustration of Figure 46, where permittivity sharply diminishes with increasing frequency in the low-frequency range. Simultaneously, there is a peak in dielectric loss at this frequency, signifying the dispersion frequency. The onset of Maxwell–Wagner behavior in BST-Cu composites implies that the observed increase in measured permittivity is a result of heightened interfacial polarization rather than relaxation polarization. However, in the Maxwell–Wagner mechanism, the effect of conductance loss (the ε'' in Eq. (34), which comprises both relaxation polarization and conductance loss) on the dielectric loss of composites has been considered.

Furthermore, the conductivity of BST–Cu composites increases with a rise in Cu content. If Cu were to be integrated into the BST lattice as an acceptor, one would expect a reduction in the concentration of conduction electrons due to the additional trapping of electrons by the incorporated acceptor ions. However, our observations indicate the opposite. Instead of being trapped solely in singly ionized oxygen vacancies, electrons may also undergo capture by T^{i4+} in BST, leading to the formation of Ti^{3+}. A substantial presence of Ti^{3+} ions on Ti^{4+} sites could result in the hopping of small polarons. Nevertheless, the reported activation energy for the hopping of small polarons between Ti^{4+} and Ti^{3+} ions in reduced BST falls within the range of 0.068–0.074 eV[189], [190], values significantly lower than those observed in BST–Cu composites. Small polaron hopping could potentially serve as a conduction mechanism for analogous $BaTiO_3$–Ni composites[191]. The apparent contrast in electrical conduction between BST–Cu and –Ni composites might stem from differences in concentration of oxygen vacancies and electrons formed through distinct sintering conditions.

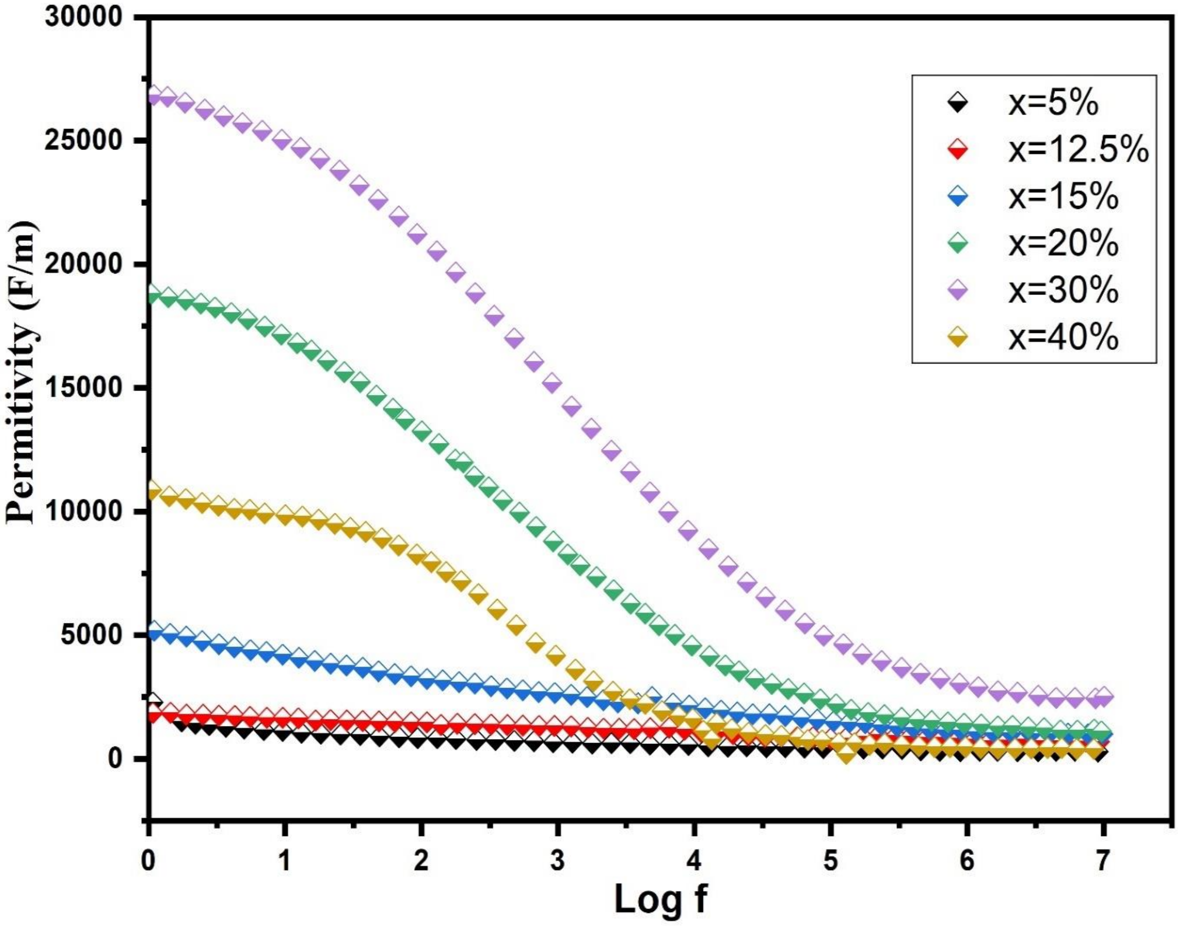

Figure 46. Permittivity of BST-Cu_x (x=5,12.5, 15, 20, 30 and 40%) composites

7. Conclusions

$BaTiO_3$, $B_{1-x}Sr_xTiO_3$, $Ba_{1-x}Y_xTiO_3$, $BaTi_{1-x}Y_xO_3$, $Ba_{1-x}Y_xTi_{1-x}Y_xO_3$, and $Ba_{1-x}Sr_xTi_{1-x}Y_xO_3$ (x=0.075) ceramics have been properly synthesized by sol-gel process. The structural, microstructural, chemical compositional stoichiometry, optical, thermal conductivity, and mechanical properties of the prepared samples were studied and described in detail. X-ray diffraction evaluation and Rietveld refinement have shown that BT, BSrT, and BYT ceramic compounds possess tetragonal structure and cubic structure for BTY, BYTY, and BSrTY samples. FT-IR investigations have supported the XRD analysis's results. The SEM analyses revealed that the particles are formed in the shape of flat blocks. EDS investigation revealed that the produced ceramic samples are in a high-purity material without any impurities. The changes in thermal conductivity with Y and Sr dopants can be ascribed to the increase in the distance within Ti-O bonds and due to the change in the strength of the bond between the atoms. UV-vis spectroscopy was used to identify the optical band gap of the ceramics, and it showed a decrease caused by the generation of oxygen vacancies and the introduction of lattice distortions. The examination of the mechanical strength properties indicated that the compressive strength of the BT, BSrT, BYT, BTY, BYTY, and BSrTY ceramics decreases with the Sr and Y dopant contents; this variation in the compressive strength behavior is related to the shape and the grain size of the latter. A higher compressive strength corresponded to the undoped barium titanate, demonstrating that the microstructure of the as-prepared ceramic compounds affects the compressive strength. Dense BST-Cux (x=5,12.5, 15, 20, 30 et 40%) ceramic composites were successfully fabricated and consolidated using spark plasma sintering. The AC conductivity of these composites exhibited a gradual increase with higher Cu content and temperature. The primary electrical conduction mechanism shifted from oxygen vacancy migration to band conduction involving trapped electrons within oxygen vacancies. The electrical conductivity showed an upward trend with increasing Cu content. Below the Curie temperature (T_c), conductivity rose with temperature, while above 130°C, it declined. This change was attributed to variances in the electrical conduction mechanisms between semiconductors and conductors.

- In micro-optical electro-mechanical systems, the studied materials could function as multipurpose, smart materials by fusing their exceptional physical and optical properties.
- The optical band gap energy was found in the semiconducting range of 3.1–2.21 eV. The thermal and electrical conductivity of $BaTiO_3$ has been improved by optimizing the doping of yttrium in weight percentages and causing the samples to become semiconductor materials. The electrical conduction mechanism in doped ceramics could be attributed to the passage of free carrier chargers through a material. The work in this paper is fundamental to the understanding of the defects associated with the crystal structure and thermoelectric behavior of Y-doped $BaTiO_3$ ceramics and can provide a reference for the application in the MLCC industry.
- The impedance plots revealed higher Z″ peak values at grain boundaries compared to grains, indicating a two-layer model with conducting grains separated by poorly

conducting grain boundaries. The grain boundary resistance (R_{gb}) decreased with elevated Cu content.

- The dielectric behavior of BST-Cu composites exhibited variability based on the phase ratio. Remarkably, composites with 30 wt% Cu content achieved a maximum permittivity of 1.0×10^5 at 1 kHz. Furthermore, these composites displayed elevated permittivity at low frequencies compared to high frequencies, attributed to Maxwell–Wagner polarization.

8. New scientific results

Based on the integrated experimental research studies of pure and doped Barium titanate synthesized using sol-gel method, the following new scientific findings were derived:

1st Claim. Low-temperature preparation of pure and doped barium titanate ceramics using modified sol-gel method.

It was demonstrated that doped barium titanate can be produced at low temperatures using a modified sol-gel method. Drawing from cutting-edge research and insights from prior published works, this innovative process integrates barium acetate trihydrate [$Ba(CH_3CO_2)2·3H_2O$] and titanium isopropoxide [$Ti[OCH(CH_3)_2]_4$] as primary precursors, while introducing lactic acid and acetic acid as pivotal stabilizing agents, a strategic evolution inspired by recent investigations into solution chemistry optimization. The process commences with the dissolution of titanium isopropoxide in a precisely calibrated mixture of water and acetic acid, maintaining a delicate equilibrium at 70°C while employing a novel agitation mechanism operating at 300rpm, a nuanced refinement inspired by computational modeling insights into fluid dynamics. This meticulous orchestration yields a stable solution, epitomized by the emergence of a transparent TiO_2 matrix, a characteristic emblematic of optimized nucleation kinetics uncovered through state-of-the-art spectroscopic analyses. Subsequently, the dissolution of barium acetate in distilled water at an elevated temperature of 90°C for a meticulously timed duration of 15 minutes signifies a strategic departure from conventional approaches, a paradigm shift informed by recent breakthroughs in reaction kinetics elucidated through advanced kinetic modeling algorithms. This transformative fusion of precursors sets the stage for gel formation, followed by a judicious drying regimen that exploits recent advances in controlled atmosphere processing, ensuring the preservation of critical structural features. The resultant xerogel undergoes a transformative process within an agate mortar, guided by insights gleaned from advanced particle engineering methodologies, aimed at mitigating powder agglomeration through precise control of mechanical forces. The process culminates in a meticulously orchestrated calcination phase, characterized by the application of temperatures reaching 950°C over a precisely optimized duration of 3 hours, facilitated by recent advancements in thermal profiling techniques that afford unprecedented control overheat transfer phenomena. This harmonious convergence of cutting-edge methodologies and insights from the forefront of materials research heralds a new era in the synthesis of doped barium titanate, offering tantalizing prospects for next-generation electronic devices and energy storage technologies.

2nd Claim. The Effect of Sr Dopants on the Thermal Conductivity of $BaTiO_3$

I have experimentally demonstrated that the thermal conductivity of $BaTiO_3$ samples can be altered by the addition of strontium (Sr) dopant during the low temperature sol-gel method. Increasing the strontium content increases the thermal conductivity from 2.24 (0 m/m% Sr content) to 6.98 $Wm^{-1}K^{-1}$ (30 m/m% Sr content), which is attributed to the strengthened atomic bonds and the altered crystal structural dynamics.

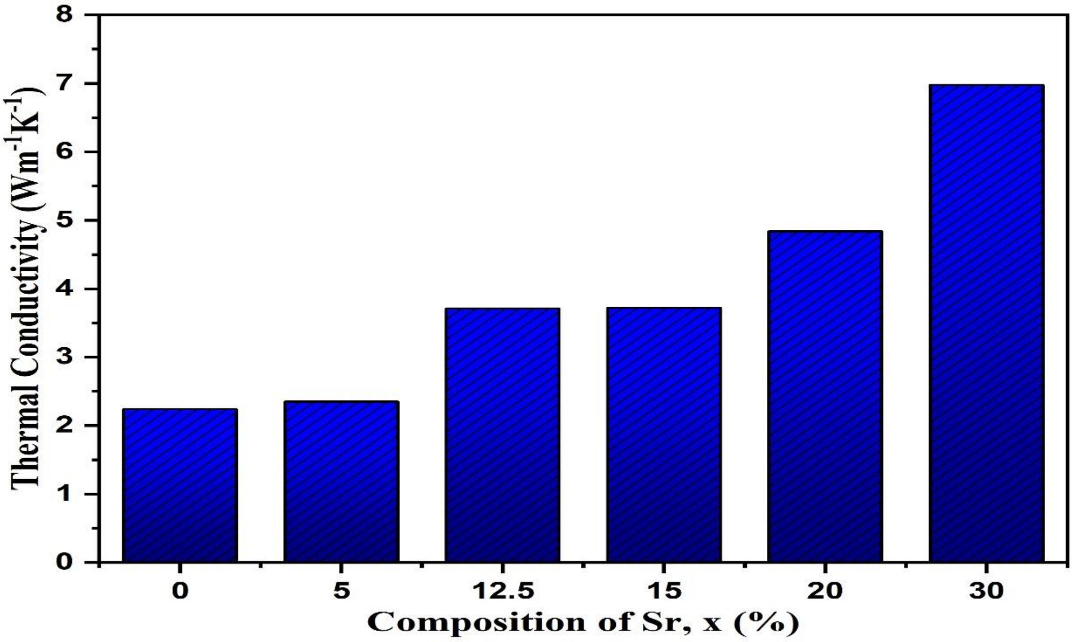

Figure A. The room temperature thermal conductivity of as prepared samples of the BSrxT (x=0, 5, 12.5, 15, 20 and 30%) ceramics

3rd Claim. Band Gap Engineering in Yttrium-Doped Barium Titanate ($BaTiO_3$) for Enhanced Electronic Properties

I have experimentally demonstrated that the addition of Y^{3+} leads to a decrease in the band gap energy of $BaTiO_3$ ceramics prepared by the sol-gel method. The band gap energy of $Ba_{1-x}Y_xTiO_3$, (x=0-0.3) ceramics prepared by doping 0; 5; 12.5; 15; 20 and 30 wt% Y^{3+}, decreases steadily from 3.1eV (Pure $BaTiO_3$) to 2.21eV (30m/m% Yttrium).

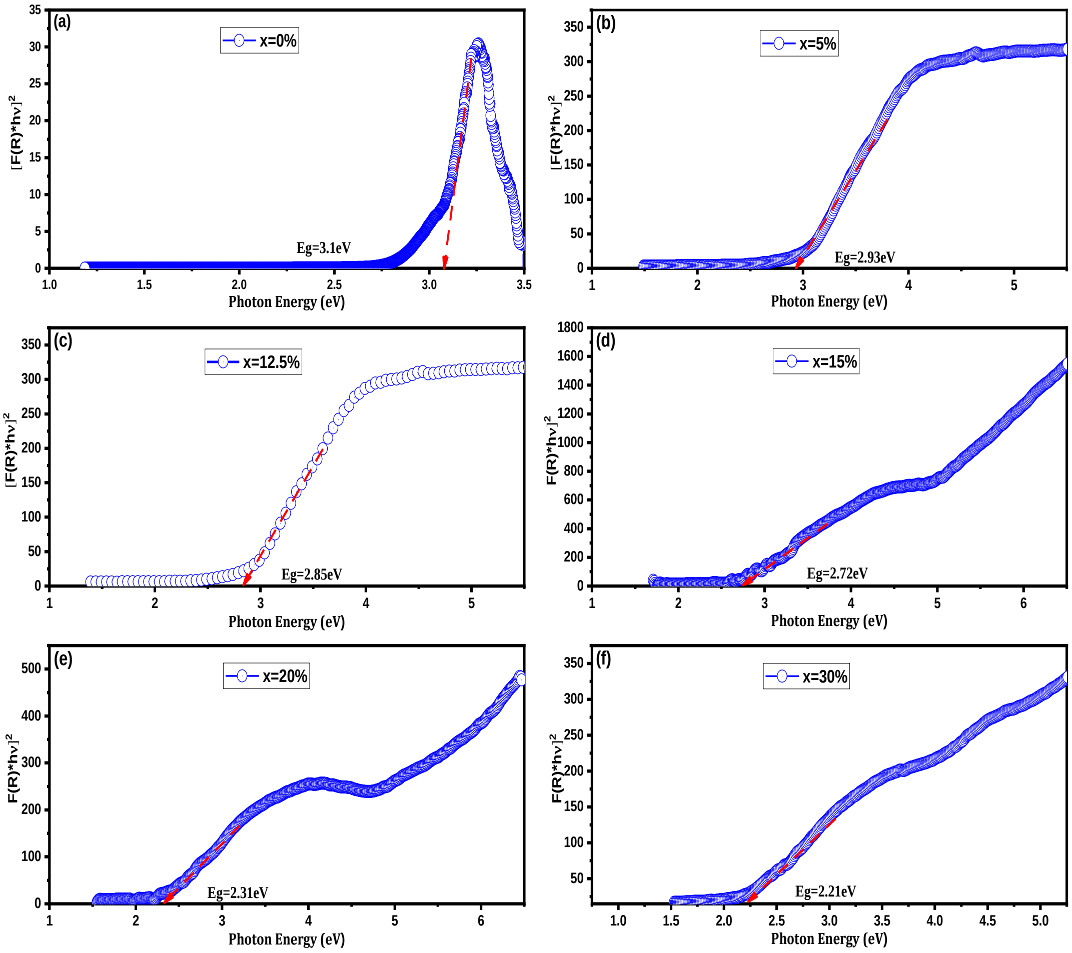

Figure B. Band gap energy from Tauc plot of (a) BT, (b) BY5%T, (c) BY12.5%T, (d) BY15%T, (e) BY20%T, and (f) BY30%T

Table A. Band gap value of $Ba_{1-x}Y_xTiO_3$, (x=0-0.3)

Sample	Band gap value (eV) This work
$Ba_{1-x}Y_xTiO_3$, x=0.00	3.10
$Ba_{1-x}Y_xTiO_3$, x=0.05	2.93
$Ba_{1-x}Y_xTiO_3$, x=0.125	2.85
$Ba_{1-x}Y_xTiO_3$, x=0.15	2.72
$Ba_{1-x}Y_xTiO_3$, x=0.20	2.31
$Ba_{1-x}Y_xTiO_3$, x=0.30	2.21

4th Claim. Effect of Sr and Y Dopants and co-Doping on Mechanical Properties in $BaTiO_3$

I have demonstrated that the 7.5% Sr and Y doping and co-doping ($BaTiO_3$, $B_{1-x}Sr_xTiO_3$, $Ba_{1-x}Y_xTiO_3$, $BaT_{1-x}Y_xO_3$, $Ba_{1-x}Y_xTi_{1-x}Y_xO_3$, and $Ba_{1-x}Sr_xTi_{1-x}Y_xO_3$ (x=0.075) reduces the compressive strength of samples made of the same low temperature sol-gel method $BaTiO_3$ powder by 8.9-17%. The decrease of the strength values of the samples (Fig.C) from 32.91 MPa (pure BaTiO3) to 28.09 MPa ($Ba_{1-x}Sr_xTi_{1-x}Y_xO_3$, x=0.075) and the decrease of the average grain size due to doping from 4.6 µm (pure $BaTiO_3$) to 0.51 µm (BSrTY = $Ba_{1-x}Sr_xTi_{1-x}Y_xO_3$, x=0.075) (Table B) occur in parallel.

Table B. The average Grain size of the compounds

Samples	Grain size (µm)
BT	4.6
BSrT	4.1
BYT	3.7
BTY	3.3
BYTY	0.9
BSrTY	0.5

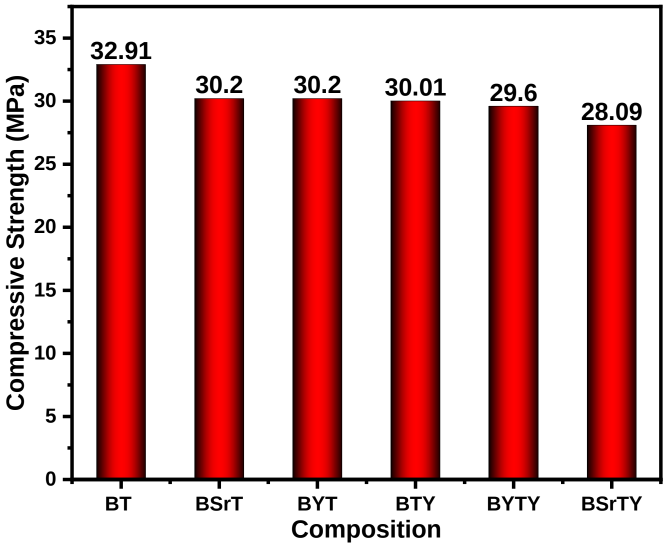

Figure C. Histogram of the compressive strength of the as-prepared BSrT, BYT, BTY, BYTY, and BSrTY samples

5th Claim. Unveiling the Impact of Sr and Y Doping and Co-Doping on the Optical Properties of $BaTiO_3$

The introduction of dual dopants, specifically 7.5% Sr in the Ba-site and 7.5% Y in the Ti-site, demonstrates a novel approach in influencing the conduction band's bottom in ceramic materials. This concurrent doping strategy leads to a significant narrowing of the conduction band, ultimately resulting in a remarkable reduction in the band gap energy. Notably, my research indicates a substantial decrease in the band gap energy from 3.1eV to 2.74eV when employing this dual dopant strategy, compared to materials doped with only one element (either Sr or Y, but not both).

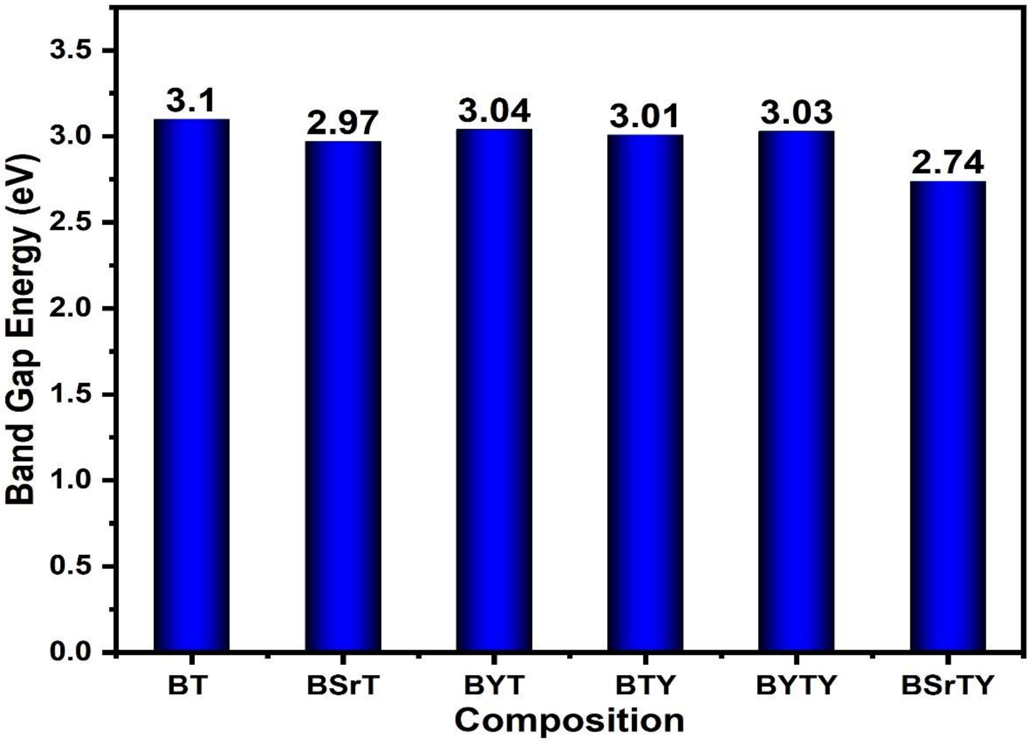

Figure D. Band gap energy of the as-produced samples

6th Claim. Elaboration of new $Ba_{0.85}Sr_{0.15}TiO_3$/Cu composites: via sol-gel and spark plasma sintering

An innovative scientific approach for preparing a new composite, $Ba_{0.85}Sr_{0.15}TiO_3$/Cu, has been established through the integration of the sol-gel method with spark plasma sintering. Barium strontium titanate (BST) powders, synthesized via the sol-gel technique, were combined with high-purity Cu powders (Cu, purity: 99.8%, average particle size: 5µm). The BST powders were initially mixed with Cu content ranging from 0 to 40 wt.% using zirconia balls as grinding media in a ball milling process with ethanol for 12 hours. Subsequently, the slurry was dried, and the resulting mixed powders were extracted. To densify the BST–Cu composite powders, spark plasma sintering (SPS) was employed. During the processing cycle, powder (2–2.6 g) was loaded into a graphite pressure die (inner diameter of 20 mm). The powders, with varying copper content, were heated under vacuum initially up to 600 °C by a preset program within 3 minutes, followed by applying a heating rate of 100 °C/min beyond this temperature until reaching the final sintering temperature (TF = 950 °C). Temperature measurement was conducted using an optical pyrometer focused on the surface of the graphite die, automatically regulating from 600 °C to the final sintering temperature. Upon reaching TF, a uniaxial pressure of 50 MPa was applied, and a dwelling time of 15 minutes was maintained for sintering. Notably, the ceramic samples produced by this novel method exhibited no contamination, demonstrating the ability to achieve high-purity materials even at low temperatures.

7th Claim. Enhanced Electrical and Dielectric Properties of Spark Plasma Sintered BST-Cu Composites

I discovered that the effective engineering and consolidation of dense BST-Cu ceramic composites through spark plasma sintering resulted in a gradual increase in AC conductivity with higher Cu content and temperature. The observed shift in the primary electrical conduction mechanism from oxygen vacancy migration to band conduction involving trapped electrons within oxygen vacancies was notable. Increasing Cu content had a positive impact on electrical conductivity, with a rising trend below the Curie temperature (Tc) and a decline above 130°C. This temperature-dependent behavior was linked to differences in electrical conduction mechanisms between semiconductors and conductors.

Impedance plots revealed higher Z'' peak values at grain boundaries compared to grains, indicating a two-layer model with conducting grains separated by poorly conducting grain boundaries. The grain boundary resistance (R_{gb}) decreased with increased Cu content.
The dielectric behavior of BST-Cu composites displayed variability based on the phase ratio. Remarkably, composites with 30 wt% Cu content achieved a maximum permittivity of 1.0×10^5 at 1 kHz. Additionally, these composites exhibited heightened permittivity at low frequencies compared to high frequencies, attributed to Maxwell–Wagner polarization.

Publications

Articles related to the dissertation:

1. Mohammed Tihtih, Jamal Eldin FM Ibrahim, Mohamed A. Basyooni, Redouane En-nadir, Walid Belaid, Irina Hussainova and István Kocserha, “Development of Yttrium-Doped BaTiO3 for Next-Generation Multilayer Ceramic Capacitors.” *ACS Omega* (2023): *IF (4.10) Q1*
2. Mohammed Tihtih, Jamal Eldin FM Ibrahim, Mohamed A Basyooni, Redouane En-Nadir, Irina Hussainova, Istvan Kocserha, “Functionality and Activity of Sol–Gel-Prepared Co and Fe co-Doped Lead-Free BTO for Thermo-Optical Applications.” *ACS Omega* (2023): *IF (4.10) Q1*
3. Mohammed Tihtih, Jamal Eldin FM Ibrahim, Mohamed A Basyooni, Emese Kurovics, Walid Belaid, Irina Hussainova, István Kocserha, “Role of A-site (Sr), B-site (Y), and A, B sites (Sr, Y) substitution in lead-free BaTiO3 ceramic compounds: Structural, optical, microstructure, mechanical, and thermal conductivity properties.” *Ceramics International* (2023): *IF (5.2) Q1*
4. Mohammed Tihtih, Jamal Eldin F M Ibrahim, Mohamed A Basyooni, Walid Belaid, László A Gömze, István Kocserha, “Structural, optical, and electronic properties of barium titanate: experiment characterisation and first-principles study.” *Materials Technology* (2023): *IF (4.2) Q1*
5. Mohammed Tihtih, Jamal Eldin F M Ibrahim, Mohamed A Basyooni, Walid Belaid, László A Gömze, István Kocserha, “Structural, optical, and electronic properties of barium titanate: experiment characterisation and first-principles study.” *Materials Technology* (2023): *IF (4.2) Q1*
6. Mohammed Tihtih, Jamal Eldin FM Ibrahim, Mohamed A. Basyooni, Redouane En-nadir, Walid Belaid, Mohamed M. Abdelfattah, Irina Hussainova, Gábor Pszota and István Kocserha, “Enhanced optical and thermal conductivity properties of barium titanate ceramic via strontium doping for thermo-optical applications.” *Optical and Quantum Electronics* (2023): *IF (3.0) Q2*
7. Mohammed Tihtih, Jamal Eldin FM Ibrahim, Emese Kurovics, and László A. Gömze. "Synthesis of $Ba_{1-x}SrxTiO_3$ (x= 0–0.3) ceramic powders via sol-gel method: structural, microstructure, thermal conductivity, and compressive strength properties." *Crystal Research and Technology* 57, no. 1 (2022): 2100106. *IF (1.639) Q2*
8. Mohammed Tihtih, Jamal Eldin FM Ibrahim, Emese Kurovics, and László A. Gömze. "Study of the structure, microstructure and temperature dependent thermal conductivity properties of $SrTiO_3$: via Y^{3+} substitution." In *Journal of Nano Research*, vol. 69, pp. 33-42. Trans Tech Publications Ltd, 2021. *IF (3.06) Q3*
9. Mohammed Tihtih, Jamal Eldin FM Ibrahim, Emese Kurovics, and Mohamed Abdelfattah. "Study on the effect of Bi dopant on the structural and optical properties of $BaTiO_3$ nanoceramics synthesized via sol-gel method." In *Journal of Physics: Conference Series*, vol. 1527, no. 1, p. 012043. IOP Publishing, 2020. *IF (0.55) Q3*
10. Mohammed Tihtih, Aleksei V. Ponaryadov, Jamal Eldin FM Ibrahim, Emese Kurovics, Elena L. Kotova, and László A. Gömze. "Effect of temperature on the structural

properties of barium titanate nanopowders synthesis via sol-gel process." *Epitoanyag-Journal of Silicate Based & Composite Materials* 72, no. 5 (2020). *IF (1.079)*

11. Mohammed Tihtih, Karoum Limame, Yahya Ababou, Salaheddine Sayouri, and Jamal Eldin FM Ibrahim. "Sol-gel synthesis and structural characterization of Fe doped barium titanate nanoceramics." *Építöanyag* 6 (2019): 190-193. *IF (1.079)*

Other publications:

1. Redouane En-nadir, Haddou El Ghazi, Mohammed Tihtih, Shrouk E. Zaki, Walid Belaid, Ibrahim Maouhoubi, Izeddine Zorkani.. " Exploring the electronic properties of shallow donor impurities in modified ∩-shaped potential: effects of applied electric field, parabolicity, compositions, and thickness." *The European Physical Journal B* 96(6):78 (2024). *IF (1.6) Q2*
2. Redouane En-Nadir, Mohamed A Basyooni-M Kabatas, Mohammed Tihtih, Haddou El Ghazi. " Innovative sustainable ceramic Bricks: Linear and nonlinear optical absorption coefficients in InGaN/GaN quantum wells: Interplay between intense laser field and higher-order anharmonic potentials." *Heliyon* (2023). *IF (4.1) Q1*
3. Mohamed A Basyooni, Mohamed Achehboune, Issam Boukhoubza, AEH Gaballah, Mohammed Tihtih, Walid Belaid, Redouane En-nadir, Issam Derkaoui, Ahmed M Abdelbar, Shrouk E Zaki, Şule Ateş, Yasin Ramazan Eker. " Impact of thickness on optoelectronic properties of α-MoO3 film photodetectors: Integrating first-principles calculations with experimental analysis." *Physica B: Condensed Matter* (2023). *IF (2.8) Q2*
4. Jamal Eldin FM Ibrahim, Emese Kurovics, Mohammed Tihtih, Mohamed A Basyooni, István Kocserha. "Reaction synthesis of porous nano-structured mullite ceramic composites from alumina and zeolite-poor rock with enhanced strength and low thermal conductivity." *Results in Engineering* (2023). *IF (5.00) Q1*
5. Redouane En-Nadir, Mohamed A Basyooni-M. Kabatas, Mohammed Tihtih, Walid Belaid, Ilyass Ez-Zejjari, El Ghmari Majda, Haddou El Ghazi, Ahmed Sali, Izeddine Zorkani. " Enhancing Emission via Radiative Lifetime Manipulation in Ultrathin InGaN/GaN Quantum Wells: The Effects of Simultaneous Electric and Magnetic Fields, Thickness, and Impurity." *Nanomaterials* (2023). *IF (5.3) Q1*
6. Mohamed A Basyooni, Mohammed Tihtih, Shrouk E Zaki, Yasin Ramazan Eker. " High-Performance Negative Self-Powered α-MoO3/Ir/α-MoO3 Photodetectors: Probing the Influence of Coulomb Deep Traps." *ACS Applied Electronic Materials* (2023). *IF (7.2) Q1*
7. Redouane En-nadir, Haddou El-ghazi, Liviu Leontie, Mohammed Tihtih, Shrouk E Zaki, Walid Belaid, Aurelian Carlescu, Izeddine Zorkani. " Tailoring optoelectronic properties of InGaN-based quantum wells through electric field, indium content, and confinement shape: A theoretical investigation." *Physica B: Condensed Matter* (2023). *IF (2.8) Q2*
8. Redouane En-nadir, Haddou El-ghazi, Mohammed Tihtih, Walid Belaid, Shrouk E Zaki, Ibrahim Maouhoubi, Izeddine Zorkani. " Analyzing the combined influences of external electric field, impurity-location, in-content, and QW’s number on donor-

impurity binding energy in multiple quantum wells with finite squared potential." *Optical and Quantum Electronics* (2023). *IF (3.0) Q2*

9. Jamal Eldin FM Ibrahim, Mohammed Tihtih, Ethem İlhan Şahin, Mohamed A Basyooni, István Kocserha. " Sustainable Zeolitic Tuff Incorporating Tea Waste Fired Ceramic Bricks: Development and Investigation." *Case Studies in Construction Materials* (2023). *IF (6.2) Q1*
10. Redouane En-nadir, Haddou El Ghazi, Mohammed Tihtih, Shrouk E Zaki, Walid Belaid, Ibrahim Maouhoubi, Izeddine Zorkani. " Exploring the electronic properties of shallow donor impurities in modified∩-shaped potential: effects of applied electric field, parabolicity, compositions, and thickness." *The European Physical Journal B* (2023). *IF (1.6) Q2*
11. Mohamed A Basyooni, Amina Houimi, Mohammed Tihtih, Shrouk E Zaki, Issam Boukhoubza, Walid Belaid, Redouane En-nadir, Jamal Eldin FM Ibrahim, GF Attia. " Boosting the efficiency of Cu2ZnSnS4 solar cells with VO2 phase transition photonic crystal." *Optical Materials* (2023). *IF (3.9) Q2*
12. Mohamed A Basyooni, AEH Gaballah, Mohammed Tihtih, Issam Derkaoui, Shrouk E Zaki, Yasin Ramazan Eker, Şule Ateş. " Thermionic Emission of Atomic Layer Deposited MoO3/Si UV Photodetectors." *Materials* (2023). *IF (3.4) Q2*
13. Walid Belaid, Haddou El Ghazi, Shrouk E Zaki, Mohamed A Basyooni, Mohammed Tihtih, Redouane Ennadir, Hamdi Şükür Kılıç, Izeddine Zorkani, Anouar Jorio. " A theoretical study of the effects of electric field, hydrostatic pressure, and temperature on photoionization cross-section of a donor impurity in (Al, Ga)N/AlN double triangular quantum wells." *Physica Scripta* (2023). *IF (2.9) Q2*
14. Redouane En-nadir, Haddou El-ghazi, Walid Belaid, Mohammed Tihtih, Hassan Abboudi, Ibrahim Maouhoubi, Anouar Jorio, Izeddine Zorkani. " Intrasubband-related linear and nonlinear optical absorption in single, double and triple QW: the compositions, temperature and QW's number effects." *Philosophical Magazine* (2023). *IF (1.86) Q2*
15. Jamal Eldin FM Ibrahim, Mohammed Tihtih, Emese Kurovics, Ethem İlhan Şahin, László A Gömze, István Kocserha. " Glass-ceramic foams produced from zeolite-poor rock (Tokaj)." *Pollack Periodica* (2023). *IF (0.94) Q3*
16. Mohamed A Basyooni, Mohammed Tihtih, Issam Boukhoubza, Jamal Eldin FM Ibrahim, Redouane En-nadir, Ahmed M Abdelbar, Khalid Rahmani, Shrouk E Zaki, Şule Ateş, Yasin Ramazan Eker. " Iridium/Silicon Ultrathin Film for Ultraviolet Photodetection: Harnessing Hot Plasmonic Effects." *physica status solidi (RRL)–Rapid Research Letters* (2023). *IF (2.77) Q2*
17. Shrouk E Zaki, Mohamed A Basyooni, Walid Belaid, Mohammed Tihtih, Jamal Eldin FM Ibrahim, GF Attia. " Terahertz resonance frequency through ethylene glycol phononic multichannel sensing via 2D MoS2/PtSe2 structure." *Materials Chemistry and Physics* (2022). *IF (4.6) Q2*
18. Shrouk E Zaki, Mohamed A Basyooni, Mohammed Tihtih, Walid Belaid, Jamal Eldin FM Ibrahim, Mohamed Mostafa Abdelfattah, Amina Houimi, AM Abdelaziz. " Tin diselenide/zirconium disulfide terahertz acoustic multi-layer superlattice for liquid

sensing applications of acetonitrile; reconsidering Voigt-Reuss-Hill schemes." *Results in Physics* (2022). *IF (5.3) Q1*

19. Jamal Eldin FM Ibrahim, Mohammed Tihtih, Emese Kurovics, László A. Gömze and István Kocserha. " Innovative glass-ceramic foams prepared by alkali activation and reactive sintering of zeolite-poor rock and sawdust for thermal insulation." *Journal of Building Engineering* (2022): *IF (7.144) D1*
20. Mohamed A Basyooni, Shrouk E Zaki, Nada Alfryyan, Mohammed Tihtih, Yasin Ramazan Eker, Gamal F Attia, Mücahit Yılmaz, Şule Ateş, Mohamed Shaban. " Nanostructured MoS2 and WS2 Photoresponses under Gas Stimuli." *Nanomaterials* (2022). *IF (5.3) Q1*
21. Al-Saudi Sarah Kareem Mohammed, Emese Kurovics, Jamal-Eldin FM Ibrahim, Mohammed Tihtih, Andrea Simon, Róbert Géber. " Preparation of an Aluminum Titania/Mullite Composite from the Raw Materials Alumina, Titania and Silica Fume." *Revue des Composites et des Materiaux Avances* (2022). *IF (1.02) Q3*
22. Jamal Eldin FM Ibrahim, Emese Kurovics, Mohammed Tihtih, and László A. Gömze and István Kocserha. "Synthesis and characterization of alkali-activated zeolite-poor rocks." In Journal of Physics: Conference Series, vol. 2315, no. 1, p. 012020. IOP Publishing, 2022.
23. M Abdelfattah, R Géber, M Tihtih, I Kocserha. " Enhancement the properties of lightweight concrete mortars by some additive materials." In Journal of Physics: Conference Series, 2315 (1), 012005. IOP Publishing, 2022.
24. Mohamed A Basyooni, Shrouk E Zaki, Mohammed Tihtih, Yasin Ramazan Eker, Şule Ateş. " Photonic band gap engineering in (VO2) n/(WSe2) n photonic superlattice for versatile near-and mid-infrared phase transition applications." *Journal of Physics: Condensed Matter* (2022). *IF (2.7) Q2*
25. Emese Kurovics, Jamal-Eldin FM Ibrahim, Mohammed Tihtih, Emese Sebe. " Phase composition and microstructure of ceramics made from kaolin mineral, alumina, and corn starch." *Epitoanyag-Journal of Silicate Based & Composite Materials* 72, no. 5 (2022). *IF (1.079)*
26. Jamal Eldin FM Ibrahim, Olga B. Kotova, Shiyong Sun, Emese Kurovics, Mohammed Tihtih, and László A. Gömze. "Preparation of innovative eco-efficient composite bricks based on zeolite-poor rock and Hen's eggshell." *Journal of Building Engineering* 45 (2022): 103491. *IF (7.144) D1*
27. Jamal Eldin FM Ibrahim, Mohammed Tihtih, Mohamed A Basyooni, István Kocserha. " Innovative sustainable ceramic Bricks: Exploring the synergy of natural zeolite tuff and aluminum dross." *Construction and Building Materials* 297 (2021): 123715. *IF (6.14) D1*
28. Jamal Eldin FM Ibrahim, Afanasy S. Apkarian, Mohammed Tihtih, Sergei N. Kulkov, and László A. Gömze. "In-situ carbonization of natural zeolite-alumina composite materials incorporated sawdust." *Epitoanyag-Journal of Silicate Based & Composite Materials* 73, no. 4 (2021). *IF (1.079)*
29. Jamal Eldin FM Ibrahim, Emese Kurovics, Mohammed Tihtih, and László A. Gömze. "Ceramic bricks with enhanced thermal insulation produced from natural zeolite." *Pollack Periodica* 16, no. 3 (2021): 101-107. *IF (0.87) Q3*

30. Jamal Eldin FM Ibrahim, Mohammed Tihtih, and László A. Gömze. "Environmentally-friendly ceramic bricks made from zeolite-poor rock and sawdust." *Construction and Building Materials* 297 (2021): 123715. *IF (6.14) D1*
31. Irina N Sevostianova, TATIANA YU SABLINA, Sergei N Kulkov, Mohammed Tihtih, LÁSZLÓ A GÖMZE. " Stress-strain behavior of high porous zirconia ceramic." *Epitoanyag-Journal of Silicate Based & Composite Materials* (2021). *IF (1.079)*
32. Jamal Eldin FM Ibrahim, Ayhan Mergen, Umut Parlak, Emese Kurovics, Mohammed Tihtih, and László A. Gömze. "Synthesis and characterization of iron-doped $GdMnO_3$ multiferroic ceramics." *Építöanyag* (Online) 1 (2021): 24-27. *IF (1.079)*
33. Emese Kurovics, Olga B. Kotova, Jamal Eldin FM Ibrahim, Mohammed Tihtih, Shiyong Sun, Péter Pala, and László A. Gomze. "Characterization of phase transformation and thermal behavior of Sedlecky Kaolin." *Építöanyag* (Online) 4 (2020): 144-147. *IF (1.079)*
34. Aleksei V Ponaryadov, Olga B Kotova, Mohammed Tihtih, Shiyong Sun. " Natural titanium dioxide nanotubes." *Építöanyag* (Online) 4 (2020). *IF (1.079)*
35. Jamal Eldin FM Ibrahim, Dmitry A. Shushkov, Emese Kurovics, Mohammed Tihtih, Olga B. Kotova, Péter Pala, and László A. Gömze. "Effect of composition and sintering temperature on thermal properties of zeolite-alumina composite materials." *Epitoanyag-Journal of Silicate Based & Composite Materials* 72, no. 4 (2020). *IF (1.079)*
36. Emese Kurovics, Jamal Eldin FM Ibrahim, Mohammed Tihtih, Bella Udvardi, Kanokon Nuilek, & László A. Gömze. (2020, April). Examination of mullite ceramic specimens made by conventional casting method from kaolin and sawdust. In *Journal of Physics: Conference Series* (Vol. 1527, No. 1, p. 012034). IOP Publishing. *IF (0.55) Q3*
37. Jamal Eldin FM Ibrahim, Kurovics, M. Tihtih, P. Somdee, A. G. Gerezgiher, K. Nuilek, E. E. Khine, and M. Sassi. "Preparation and Investigation of Alumina-Zeolite Composite Materials." In *Journal of Physics: Conference Series*, vol. 1527, no. 1, p. 012029. IOP Publishing, 2020. *IF (0.55) Q3*
38. M Abdelfattah, I Kocserha, R Géber, M Tihtih, F Móricz. " Evaluating the properties and mineral phases of the expanded clay aggregates with the bentonite additive material." In *Journal of Physics: Conference Series*. IOP Publishing, 2020. *IF (0.55) Q3*

Books

Mohamed A Basyooni, Shrouk E Zaki, Mohammed Tihtih, Issam Boukhoubza, Redouane En-nadir, GF Attia. "Fundamentals and Classifications of CO2 Sensors." *Handbook of Nanosensors: Materials and Technological Applications* (2023).

Conference presentations

1. Structural and Magnetic Properties of iron doped $GdMnO_3$ Multiferroic Ceramics. The 5th International Conference on Competitive Materials and Technology Processes, Miskolc, Hungary. October 8 th – 12 th, 2018. Poster presentation
2. Structural and optical properties of Tetragonal Barium Titanate: experiment and a First Principle Study. Advances in Physics International Conference. Pretoria, South Africa. 11-12 April 2020. Oral presentation
3. A First Principal calculation of electronic structure of the tetragonal $PbTiO_3$ compound. Advances in Physics International Conference. Pretoria, South Africa. 11-12 April 2020. Poster presentation
4. The structure, morphology, and mechanical behaviors of $SrTiO_3/BA_{0.7}Y_3TIO_3$ nanocomposite powders. EUROASIA Congress on Scientific Researches and Recent Trends-VII. Baku, Azerbaijan. December 6-9, 2020. Oral presentation
5. Effect of Bismuth on the structural and optical properties of the sol gel processed Barium titanate. The 1st European Conference on Silicon and Silica Based Materials, Miskolc, Hungary, 7th – 11th October 2019. Poster presentation
6. Effect of temperature on the structural properties of barium titanate nanopowders synthesis via sol-gel process. International Web Conference on Recent Advances in Science
   IWCRAS 2020. 30th and 31st of July 2020. Oral presentation
7. Effect of temperature on the structural properties of barium titanate nanopowders synthesis via sol-gel process. MAS 12th international european conference on mathematics, engineering, natural&medical sciences. Izmir, Turkey. July 18-19, 2020. Oral presentation
8. Morphological and structural properties of Yittrium-modified $SrTiO_3$ ceramics fabricated by Sol-gel method. The 16th Miklós Iványi International PhD and DLA Symposium. 26-27 Oct 2020, Pécs, Hungary. Oral presentation
9. Synthesis and Characterization of Yittrium doped Strontium Titanate $Sr_{1-x}Y_xTiO_3$ Nanopowders by Sol-gel Route. The 16th Miklós Iványi International PhD and DLA Symposium. 26-27 Oct 2020, Pécs, Hungary. Poster presentation
10. Study of the Structure, Microstructure and Temperature Dependent Thermal Conductivity Properties of Strontium Titanate: via Y^{3+} substitution. Solid Compounds of Transition Elements SCTE 2021. April 26, 2021. Warsaw, Poland. Oral presentation
11. Study of the $BaTiO_3$ Electronic Structure Using Density Functional Theory Calculations. Solid Compounds of Transition Elements SCTE 2021. April 26, 2021. Warsaw, Poland. Poster presentation
12. Influence of Annealing Temperature on the Properties of Barium Titanate Nanoceramics. Modern problems of theoretical, experimental and applied mineralogy. December 9, 2020. Moscow, Russia. Oral presentation
13. Enhanced thermal conductivity of $Ba_{0.85}Sr_{0.15}TiO_3/SrTiO_3$ composites through sol-gel technique. Ec-Siliconf2: The 2nd European Conference on Silicon and Silica Based Materials, Miskolc-Lillafüred, Hungary, October 4 th – 8 th, 2021. Oral presentation

14. Development of doped Barium Titanate for Next-generation Semiconductive Ceramics: A Material and Performance Analysis. 7th International Conference on Catalysis and Chemical Engineering. Las Vegas, United State. February 14-19, 2023. Oral presentation

References

[1] *T. Zaman, M. K. Islam, M. A. Rahman, A. Hussain, M. A. Matin, and M. S. Rahman, "Mono and co-substitution of Sr 2+ and Ca 2+ on the structural, electrical and optical properties of barium titanate ceramics," Ceram Int, vol. 45, no. 8, pp. 10154–10162, Jun. 2019, doi: 10.1016/j.ceramint.2019.02.064.*

[2] Y. Slimani et al., "Study on the addition of SiO2 nanowires to BaTiO3: Structure, morphology, electrical and dielectric properties," Journal of Physics and Chemistry of Solids, vol. 156, p. 110183, Sep. 2021, doi: 10.1016/J.JPCS.2021.110183.

[3] C. Zhao et al., "Practical High Piezoelectricity in Barium Titanate Ceramics Utilizing Multiphase Convergence with Broad Structural Flexibility," J Am Chem Soc, vol. 140, no. 45, pp. 15252–15260, Nov. 2018, doi: 10.1021/JACS.8B07844.

[4] V. T. Rathod, "A Review of Acoustic Impedance Matching Techniques for Piezoelectric Sensors and Transducers," Sensors 2020, Vol. 20, Page 4051, vol. 20, no. 14, p. 4051, Jul. 2020, doi: 10.3390/S20144051.

[5] M. Tihtih et al., "Structural, optical, and electronic properties of barium titanate: experiment characterisation and first-principles study," Materials Technology, pp. 1–11, Aug. 2022, doi: 10.1080/10667857.2022.2107473.

[6] J. Liu, G. Jin, Y. Chen, and W. Xue, "Properties of yttrium-doped barium titanate ceramics with positive temperature coefficient of resistivity and a novel method to evaluate the depletion layer width," Ceram Int, vol. 45, no. 5, pp. 6119–6124, Apr. 2019, doi: 10.1016/J.CERAMINT.2018.12.086.

[7] M. J. Wang et al., "Doping behaviors of yttrium, zinc and gallium in BaTiO3 ceramics for AC capacitor application," Journal of Materials Science: Materials in Electronics, vol. 25, no. 7, pp. 2905–2912, Apr. 2014, doi: 10.1007/S10854-014-1958-3/FIGURES/5.

[8] D. Makovec, Z. Samardžija, and M. Drofenik, "Solid Solubility of Holmium, Yttrium, and Dysprosium in BaTiO3," Journal of the American Ceramic Society, vol. 87, no. 7, pp. 1324–1329, Jul. 2004, doi: 10.1111/J.1151-2916.2004.TB07729.X.

[9] M. Tihtih, J. E. F. M. Ibrahim, E. Kurovics, and L. A. Gömze, "Study of the Structure, Microstructure and Temperature Dependent Thermal Conductivity Properties of SrTiO3: Via Y3+ Substitution," Journal of Nano Research, vol. 69, pp. 33–42, 2021, doi: 10.4028/WWW.SCIENTIFIC.NET/JNANOR.69.33.

[10] A. Belous, O. V'yunov, L. Kovalenko, and D. Makovec, "Redox processes in highly yttrium-doped barium titanate," J Solid State Chem, vol. 178, no. 5, pp. 1367–1375, May 2005, doi: 10.1016/J.JSSC.2005.01.014.

[11] M. Paredes-Olguín, I. A. Lira-Hernández, C. Gómez-Yáñez, and F. P. Espino-Cortés, "Compensation mechanisms at high temperature in Y-doped BaTiO3," Physica B Condens Matter, vol. 410, no. 1, pp. 157–161, Feb. 2013, doi: 10.1016/J.PHYSB.2012.11.001.

[12] X. Wang, Y. Fan, G. Luo, R. Tu, Q. Shen, and L. Zhang, "Effect of yttrium (Y) substitution on the structure and dielectric properties of BaTiO3," Ceram Int, Nov. 2022, doi: 10.1016/J.CERAMINT.2022.11.060.

[13] A. Belous, O. V'yunov, M. Glinchuk, V. Laguta, and D. Makovez, "Redox processes at grain boundaries in barium titanate-based polycrystalline ferroelectrics semiconductors," J Mater Sci, vol. 43, no. 9, pp. 3320–3326, May 2008, doi: 10.1007/S10853-008-2503-7/FIGURES/8.

[14] G. Goel, M. V. Vasić, N. K. Katiyar, S. K. Kirthika, M. Pezo, and P. Dinakar, "Potential pathway for recycling of the paper mill sludge compost for brick making," Constr Build Mater, vol. 278, 2021, doi: 10.1016/j.conbuildmat.2021.122384.

[15] M. Habib et al., "Structural evolution and electromechanical properties of SrTiO3-modified Bi0.5Na0.5TiO3–BaTiO3 ceramics prepared by sol-gel and hydrothermal methods," Mater Chem Phys, vol. 266, p. 124529, Jul. 2021, doi: 10.1016/J.MATCHEMPHYS.2021.124529.

[16] *Y. Ma, J. Song, X. Wang, Y. Liu, and J. Zhou, "Synthesis, Microstructure and Properties of Magnetron Sputtered Lead Zirconate Titanate (PZT) Thin Film Coatings," Coatings 2021, Vol. 11, Page 944, vol. 11, no. 8, p. 944, Aug. 2021, doi: 10.3390/COATINGS11080944.*

[17] *M. Tihtih et al., "Role of A-site (Sr), B-site (Y), and A, B sites (Sr, Y) substitution in lead-free BaTiO3 ceramic compounds: Structural, optical, microstructure, mechanical, and thermal conductivity properties," Ceram Int, vol. 49, no. 2, pp. 1947–1959, Jan. 2023, doi: 10.1016/J.CERAMINT.2022.09.160.*

[18] *M. Tihtih, J. E. F. M. Ibrahim, E. Kurovics, and L. A. Gömze, "Synthesis of Ba1−xSrxTiO3 (x = 0–0.3) Ceramic Powders via Sol-Gel Method: Structural, Microstructure, Thermal Conductivity, and Compressive Strength Properties," Crystal Research and Technology, p. 2100106, Oct. 2021, doi: 10.1002/CRAT.202100106.*

[19] *D. Drdlik, V. Marak, K. Maca, and K. Drdlikova, "Modification of barium titanate sintering via rare earth oxides addition: Dilatometric and microstructural study," Ceram Int, vol. 48, no. 17, pp. 24599–24608, Sep. 2022, doi: 10.1016/J.CERAMINT.2022.05.105.*

[20] *K. Zhang, L. Li, M. Wang, and W. Luo, "Charge compensation in rare earth doped BaTiO3-based ceramics sintered in reducing atmosphere," Ceram Int, vol. 46, no. 16, pp. 25881–25887, Nov. 2020, doi: 10.1016/J.CERAMINT.2020.07.072.*

[21] *A. P. Aslla-Quispe, R. H. Miwa, and J. D. S. Guerra, "Role of the rare-earth doping on the multiferroic properties of BaTiO3: First-principles calculation," Physica B Condens Matter, vol. 615, p. 413107, Aug. 2021, doi: 10.1016/J.PHYSB.2021.413107.*

[22] *M. S. Alkathy et al., "Effect of sintering temperature on structural, electrical, and ferroelectric properties of lanthanum and sodium co-substituted barium titanate ceramics," J Alloys Compd, vol. 762, pp. 49–61, Sep. 2018, doi: 10.1016/J.JALLCOM.2018.05.138.*

[23] *Y. Luo, Y. Pu, P. Zhang, J. Zhao, Y. Wu, and Y. Liu, "Study on Dielectric Properties of SiO2-doped BaTiO3 Ceramics," https://doi.org/10.1080/00150193.2015.1071594, vol. 492, no. 1, pp. 10–16, Feb. 2016, doi: 10.1080/00150193.2015.1071594.*

[24] *S. H. Yoon, Y. S. Park, J. O. Hong, and D. S. Sinn, "Effect of the pyrochlore (Y2Ti2O7) phase on the resistance degradation in yttrium-doped BaTiO3 ceramic capacitors," J Mater Res, vol. 22, no. 9, pp. 2539–2543, Sep. 2007, doi: 10.1557/JMR.2007.0326.*

[25] *J. Zhang, Y. Hou, M. Zheng, W. Jia, M. Zhu, and H. Yan, "The Occupation Behavior of Y2O3 and Its Effect on the Microstructure and Electric Properties in X7R Dielectrics," Journal of the American Ceramic Society, vol. 99, no. 4, pp. 1375–1382, Apr. 2016, doi: 10.1111/JACE.14100.*

[26] *H. I. Alkhammash, A. M. Ibrahim, and S. Fouad, "Enhancement of dielectric properties of borate glasses doped BaTiO3 for energy storage devices: characterization of optical, thermal and electrical properties," Journal of Materials Science: Materials in Electronics, vol. 33, no. 21, pp. 17048–17063, Jul. 2022, doi: 10.1007/S10854-022-08582-2/FIGURES/18.*

[27] *J. Xing, M. Radovic, and A. Muliana, "Thermal properties of BaTiO3/Ag composites at different temperatures," Compos B Eng, vol. 90, pp. 287–301, Apr. 2016, doi: 10.1016/J.COMPOSITESB.2015.12.014.*

[28] *Y. Lin, Y. Jia, G. Alva, and G. Fang, "Review on thermal conductivity enhancement, thermal properties and applications of phase change materials in thermal energy storage," Renewable and Sustainable Energy Reviews, vol. 82, pp. 2730–2742, Feb. 2018, doi: 10.1016/J.RSER.2017.10.002.*

[29] *S.-S. RYU, H.-T. KIM, H. J. KIM, and S. KIM, "Characterization of mechanical properties of BaTiO3 ceramic with different types of sintering aid by nanoindentation," Journal of the Ceramic Society of Japan, vol. 117, no. 1367, pp. 811–814, 2009, doi: 10.2109/JCERSJ2.117.811.*

[30] *L. Chen et al., "Effect of MnO2 on the dielectric properties of Nb-doped BaTiO3-(Bi0.5Na0.5)TiO3 ceramics for X9R MLCC applications," Journal of the American Ceramic Society, vol. 102, no. 5, pp. 2781–2790, May 2019, doi: 10.1111/JACE.16157.*

[31] M. Tihtih et al., “Functionality and Activity of Sol–Gel-Prepared Co and Fe co-Doped Lead-Free BTO for Thermo-Optical Applications,” ACS Omega, Jan. 2023, doi: 10.1021/ACSOMEGA.2C07660.

[32] G. A. Komandin et al., “Electrodynamic properties of porous PZT-Pt films at terahertz frequency range,” physica status solidi c, vol. 14, no. 1–2, p. 1600211, Jan. 2017, doi: 10.1002/PSSC.201600211.

[33] P. Xu et al., “Flexible BaTiO3/SiC@PbTiO3/epoxy composite films with enhanced dielectric performance at high frequency,” Ceram Int, vol. 48, no. 14, pp. 20102–20109, Jul. 2022, doi: 10.1016/J.CERAMINT.2022.03.288.

[34] Z. Pan, L. Yao, J. Zhai, D. Fu, B. Shen, and H. Wang, “High-energy-density polymer nanocomposites composed of newly structured one-dimensional BaTiO3@Al2O3 nanofibers,” ACS Appl Mater Interfaces, vol. 9, no. 4, pp. 4024–4033, Feb. 2017, doi: 10.1021/ACSAMI.6B13663/ASSET/IMAGES/LARGE/AM-2016-13663C_0010.JPEG.

[35] J. Li et al., “The Effects of Spark-Plasma Sintering (SPS) on the Microstructure and Mechanical Properties of BaTiO3/3Y-TZP Composites,” Materials 2016, Vol. 9, Page 320, vol. 9, no. 5, p. 320, Apr. 2016, doi: 10.3390/MA9050320.

[36] J. Wang et al., “High energy density of polyimide composites containing one-dimensional BaTiO3@ZrO2 nanofibers for energy storage device,” J Alloys Compd, vol. 789, pp. 785–791, Jun. 2019, doi: 10.1016/J.JALLCOM.2019.03.142.

[37] M. Tihtih, J. E. F. M. Ibrahim, E. Kurovics, and L. A. Gömze, “Study of the Structure, Microstructure and Temperature Dependent Thermal Conductivity Properties of SrTiO3: Via Y3+ Substitution,” Journal of Nano Research, vol. 69, pp. 33–42, 2021, doi: 10.4028/WWW.SCIENTIFIC.NET/JNANOR.69.33.

[38] M. C. Chiu, H. C. Yao, C. J. Huang, and F. S. Shieu, “Improvement of dielectric properties of Ba0.6Sr0.4TiO3 thin films by MgO doping,” J Appl Phys, vol. 102, no. 1, p. 014110, Jul. 2007, doi: 10.1063/1.2748424.

[39] A. B. Ustinov, G. Srinivasan, and B. A. Kalinikos, “Ferrite-ferroelectric hybrid wave phase shifters,” Appl Phys Lett, vol. 90, no. 3, p. 031913, Jan. 2007, doi: 10.1063/1.2432953.

[40] S. Lopez-Esteban et al., “Electrical discharge machining of ceramic/semiconductor/metal nanocomposites,” Scr Mater, vol. 63, no. 2, pp. 219–222, Jul. 2010, doi: 10.1016/J.SCRIPTAMAT.2010.03.062.

[41] P. Cavaliere, B. Sadeghi, and A. Shabani, “Spark Plasma Sintering: Process Fundamentals,” Spark Plasma Sintering of Materials, pp. 3–20, 2019, doi: 10.1007/978-3-030-05327-7_1.

[42] M. Fattahi, M. Najafi Ershadi, M. Vajdi, F. Sadegh Moghanlou, A. Sabahi Namini, and M. Shahedi Asl, “On the simulation of spark plasma sintered TiB2 ultra high temperature ceramics: A numerical approach,” Ceram Int, vol. 46, no. 10, pp. 14787–14795, Jul. 2020, doi: 10.1016/J.CERAMINT.2020.03.003.

[43] R. S. Mahale, V. Shamanth, P. C. Sharath, R. Shashanka, and K. Hemanth, “A review on spark plasma sintering of duplex stainless steels,” Mater Today Proc, vol. 45, pp. 138–144, Jan. 2021, doi: 10.1016/J.MATPR.2020.10.357.

[44] E. Ghasali, P. Sangpour, A. Jam, H. Rajaei, K. Shirvanimoghaddam, and T. Ebadzadeh, “Microwave and spark plasma sintering of carbon nanotube and graphene reinforced aluminum matrix composite,” Archives of Civil and Mechanical Engineering 2018 18:4, vol. 18, no. 4, pp. 1042–1054, Mar. 2018, doi: 10.1016/J.ACME.2018.02.006.

[45] Z. Cheng and J. Lin, “Layered organic-inorganic hybrid perovskites: Structure, optical properties, film preparation, patterning and templating engineering,” CrystEngComm, vol. 12, no. 10, pp. 2646–2662, 2010, doi: 10.1039/c001929a.

[46] “Synthesis, Properties and Mineralogy of Important Inorganic Materials - Terence E. Warner - Google Books.” Accessed: Jul. 01, 2020. [Online]. Available: https://books.google.hu/books?hl=en&lr=&id=IR_IxoBT_S4C&oi=fnd&pg=PR7&dq=%5B20%5D%09T.E.+Warner,+Synthesis,+properties+and+mineralogy+of+important+inorganic

+materials,+John+Wiley+%26+Sons,+2012.&ots=sX5saiM-0W&sig=qnU6Hc6AdLy_ZdJ0FVenAumknko&redir_esc=y#v

[47] O. Bohnke, C. Bohnke, and J. L. Fourquet, "Mechanism of ionic conduction and electrochemical intercalation of lithium into the perovskite lanthanum lithium titanate," Solid State Ion, vol. 91, no. 1–2, pp. 21–31, 1996, doi: 10.1016/s0167-2738(96)00434-1.

[48] G. A. Samara, "Pressure and temperature dependence of the dielectric properties and phase transitions of the ferroelectric perovskites: Pbtio3 and batio3," Ferroelectrics, vol. 2, no. 1, pp. 277–289, 1971, doi: 10.1080/00150197108234102.

[49] M. R. Ghazanfari, R. Amini, S. F. Shams, M. Alizadeh, and H. A. Ardakani, "Effect of mechanical alloying synthesis process on the dielectric properties of (Bi0.5Na0.5)0.94Ba0.06TiO3 piezoceramics," Mater Res Bull, vol. 68, pp. 260–266, 2015, doi: 10.1016/j.materresbull.2015.03.047.

[50] P. Muralt, R. G. Polcawich, and S. Trolier-McKinstry, "Piezoelectric thin films for sensors, actuators, and energy harvesting," MRS Bull, vol. 34, no. 9, pp. 658–664, Sep. 2009, doi: 10.1557/mrs2009.177.

[51] S. Švarcová, K. Wiik, J. Tolchard, H. J. M. Bouwmeester, and T. Grande, "Structural instability of cubic perovskite BaxSr1 - xCo1 - yFeyO3 - δ," Solid State Ion, vol. 178, no. 35–36, pp. 1787–1791, 2008, doi: 10.1016/j.ssi.2007.11.031.

[52] M. R. Mohammadi and D. J. Fray, "Sol-gel derived nanocrystalline and mesoporous barium strontium titanate prepared at room temperature," Particuology, vol. 9, no. 3, pp. 235–242, 2011, doi: 10.1016/j.partic.2010.08.012.

[53] Z. Peng and Y. Chen, "Preparation of BaTiO3 nanoparticles in aqueous solutions," in Microelectronic Engineering, Apr. 2003, pp. 102–106. doi: 10.1016/S0167-9317(03)00032-7.

[54] A. Habib, R. Haubner, and N. Stelzer, "Effect of temperature, time and particle size of Ti precursor on hydrothermal synthesis of barium titanate," Mater Sci Eng B Solid State Mater Adv Technol, vol. 152, no. 1–3, pp. 60–65, Aug. 2008, doi: 10.1016/j.mseb.2008.06.018.

[55] K. M. Hung, W. D. Yang, and C. C. Huang, "Preparation of nanometer-sized barium titanate powders by a sol-precipitation process with surfactants," J Eur Ceram Soc, vol. 23, no. 11, pp. 1901–1910, 2003, doi: 10.1016/S0955-2219(02)00431-4.

[56] Y. Hayashi, T. Kimura, and T. Yamaguchi, "Preparation of rod-shaped BaTiO3 powder," J Mater Sci, vol. 21, no. 3, pp. 757–762, Mar. 1986, doi: 10.1007/BF01117350.

[57] Y. W. Cho, S. K. Choi, and G. Venkata Rao, "The influence of an extrinsic interfacial layer on the polarization of sputtered BaTi O3 film," Appl Phys Lett, vol. 86, no. 20, pp. 1–3, May 2005, doi: 10.1063/1.1921358.

[58] H. Xu, L. Gao, and J. Guo, "Hydrothermal Synthesis of Tetragonal Barium Titanate from Barium Chloride and Titanium Tetrachloride under Moderate Conditions," Journal of the American Ceramic Society, vol. 85, no. 3, pp. 727–729, 2004, doi: 10.1111/j.1151-2916.2002.tb00163.x.

[59] C. S. Kim et al., "Synthesis and particle size effect on the phase transformation of nanocrystalline TiO2," Materials Science and Engineering C, vol. 27, no. 5-8 SPEC. ISS., pp. 1343–1346, Sep. 2007, doi: 10.1016/j.msec.2006.12.006.

[60] B. J. Chen, E. Y. B. Pun, and H. Lin, "Photoluminescence and spectral parameters of Eu3+ in sodium-aluminum-tellurite ceramics," J Alloys Compd, vol. 479, no. 1–2, pp. 352–356, Jun. 2009, doi: 10.1016/j.jallcom.2008.12.072.

[61] S. C. Erwin, L. Zu, M. I. Haftel, A. L. Efros, T. A. Kennedy, and D. J. Norris, "Doping semiconductor nanocrystals," Nature, vol. 436, no. 7047, pp. 91–94, Jul. 2005, doi: 10.1038/nature03832.

[62] D. J. Norris, A. L. Efros, and S. C. Erwin, "Doped nanocrystals," Science (1979), vol. 319, no. 5871, pp. 1776–1779, 2008, doi: 10.1126/science.1143802.

[63] K. G. Stamplecoskie, L. Ju, S. S. Farvid, and P. V. Radovanovic, "General control of transition-metal-doped GaN nanowire growth: Toward understanding the mechanism of

dopant incorporation," Nano Lett, vol. 8, no. 9, pp. 2674–2681, Sep. 2008, doi: 10.1021/nl8009523.

[64] M. Prades, N. Masó, H. Beltrán, E. Cordoncillo, and A. R. West, "Polymorphism of BaTiO3 Acceptor Doped with Mn3+, Fe3+, and Ti3+," Journal of the American Ceramic Society, vol. 91, no. 7, pp. 2364–2366, Jul. 2008, doi: 10.1111/j.1551-2916.2008.02397.x.

[65] M. T. Buscaglia, V. Buscaglia, M. Viviani, P. Nanni, and M. Hanuskova, "Influence of foreign ions on the crystal structure of BaTiO3," J Eur Ceram Soc, vol. 20, no. 12, pp. 1997–2007, 2000, doi: 10.1016/S0955-2219(00)00076-5.

[66] R. L. Brutchey, G. Cheng, Q. Gu, and D. E. Morse, "Positive temperature coefficient of resistivity in donor-doped BaTiO 3 ceramics derived from nanocrystals synthesized at low temperature," Advanced Materials, vol. 20, no. 5, pp. 1029–1033, 2008, doi: 10.1002/adma.200701804.

[67] N. Masó et al., "Synthesis and electrical properties of Nb-doped $BaTiO_3$," J. Mater. Chem., vol. 16, no. 30, pp. 3114–3119, 2006, doi: 10.1039/B601251E.

[68] W. Q. Cao and M. M. Ismail, "Giant dielectric constant phenomena in Bi2O3-doped Ba0.8Sr0.2TiO3 ferroelectrics," Materials Technology, vol. 32, no. 5, pp. 321–326, Apr. 2017, doi: 10.1080/10667857.2016.1216297.

[69] H. T. Langhammer, T. Walther, R. Böttcher, and S. G. Ebbinghaus, "On the incorporation of iron into hexagonal barium titanate: II. Magnetic moment, electron paramagnetic resonance (EPR) and optical transmission," Journal of Physics Condensed Matter, vol. 32, no. 38, p. 385702, Sep. 2020, doi: 10.1088/1361-648X/ab9345.

[70] M. Shandilya, R. Rai, and J. Singh, "Review: Hydrothermal technology for smart materials," Advances in Applied Ceramics, vol. 115, no. 6. Taylor and Francis Ltd., pp. 354–376, Jun. 13, 2016. doi: 10.1080/17436753.2016.1157131.

[71] N. P. Bhagya, P. A. Prashanth, R. H. krishna, B. M. Nagabhushana, and R. S. Raveendra, "Photoluminescence studies of Eu3+ activated SrTiO3 nanophosphor prepared by solution combustion approach," Optik (Stuttg), vol. 145, pp. 678–687, Sep. 2017, doi: 10.1016/j.ijleo.2017.07.003.

[72] A. Karaphun, S. Phokha, S. Hunpratub, T. Putjuso, and E. Swatsitang, "Influence of Ba substitution, Fe doping and annealing effect on magnetic and optical properties of Sr0.9Ba0.1Ti1−xFexO3 nanoparticles prepared by the hydrothermal method," Journal of Materials Science: Materials in Electronics, vol. 29, no. 10, pp. 8188–8200, May 2018, doi: 10.1007/s10854-018-8825-6.

[73] E. Hajisaeid et al., "Printed planar tunable composite right/ <scp>left-handed leaky-wave</scp> antenna based on a tunable <scp>polymer-BST</scp> substrate," Microw Opt Technol Lett, vol. 63, no. 2, pp. 626–637, Feb. 2021, doi: 10.1002/mop.32639.

[74] P. P. Khirade, V. Vinayak, P. B. Kharat, and A. R. Chavan, "Green Synthesis of Ba1−xSrxTiO3 ceramic nanopowders by sol-gel combustion method using lemon juice as a fuel: Tailoring of Microstructure, ferroelectric, dielectric and electrical properties," Opt Mater (Amst), no. September, p. 110664, 2020, doi: 10.1016/j.optmat.2020.110664.

[75] M. Arshad et al., "Fabrication, structure, and frequency-dependent electrical and dielectric properties of Sr-doped BaTiO3 ceramics," Ceram Int, vol. 46, no. 2, pp. 2238–2246, 2020, doi: 10.1016/j.ceramint.2019.09.208.

[76] G. Panomsuwan and H. Manuspiya, "Structural and dielectric properties of sol-gel derived Ba 1-x Sr x TiO 3 ($0 \leq x \leq 0.5$) ceramics for energy storage applications Recent citations Correlation between size and phase structure of crystalline BaTiO 3 particles synthesized by sol-gel method Structural and dielectric properties of sol-gel derived Ba 1-x Sr x TiO 3 (0□,,□x□,,□0.5) ceramics for energy storage applications," 2018, doi: 10.1088/2053-1591/aaedf2.

[77] *H. C. Wang et al., "Enhancement of thermoelectric figure of merit by doping Dy in La 0.1Sr0.9TiO3 ceramic," Mater Res Bull, vol. 45, no. 7, pp. 809–812, Jul. 2010, doi: 10.1016/j.materresbull.2010.03.018.*

[78] *H. Muta, K. Kurosaki, and S. Yamanaka, "Thermoelectric properties of rare earth doped SrTiO3," J Alloys Compd, vol. 350, no. 1–2, pp. 292–295, Feb. 2003, doi: 10.1016/S0925-8388(02)00972-6.*

[79] *Z. Peng, J. Li, P. Liang, Z. Yang, and X. Chao, "Improved dielectric properties and grain boundary response of SrTiO3 doped Y2/3Cu3Ti4O12 ceramics fabricated by Sol-gel process for high-energy-density storage applications," J Eur Ceram Soc, vol. 37, no. 15, pp. 4637–4644, Dec. 2017, doi: 10.1016/j.jeurceramsoc.2017.06.025.*

[80] *E. Rosa Silva, M. Curi, J. G. Furtado, H. C. Ferraz, and A. R. Secchi, "The effect of calcination atmosphere on structural properties of Y-doped SrTiO 3 perovskite anode for SOFC prepared by solid-state reaction," Ceram Int, vol. 45, no. 8, pp. 9761–9770, Jun. 2019, doi: 10.1016/j.ceramint.2019.02.011.*

[81] *D. Hu et al., "Optimization the energy density and efficiency of BaTiO3-based ceramics for capacitor applications," Chemical Engineering Journal, vol. 409, p. 127375, Apr. 2021, doi: 10.1016/J.CEJ.2020.127375.*

[82] *P. C. Bowes, J. N. Baker, and D. L. Irving, "Site preference of Y and Mn in nonstoichiometric Ba TiO3 from first principles," Phys Rev Mater, vol. 4, no. 8, p. 084601, Aug. 2020, doi: 10.1103/PhysRevMaterials.4.084601.*

[83] *S. Pradhan, H. Kaur, and M. Jayasimhadri, "Photoluminescence and thermal sensing properties of Er3+ doped silicate based phosphors for multifunctional optoelectronic device applications," Ceram Int, vol. 47, no. 19, pp. 27694–27701, Oct. 2021, doi: 10.1016/J.CERAMINT.2021.06.194.*

[84] *A. Boubaia, A. Assali, S. Berrah, H. Bennacer, I. Zerifi, and A. Boukortt, "Band gap and emission wavelength tuning of Sr-doped BaTiO3 (BST) perovskites for high-efficiency visible-light emitters and solar cells," Mater Sci Semicond Process, vol. 130, p. 105837, Aug. 2021, doi: 10.1016/J.MSSP.2021.105837.*

[85] *N. Zamperlin, R. Ceccato, M. Fontana, A. Pegoretti, A. Chiappini, and S. Dirè, "Effect of Hydrothermal Treatment and Doping on the Microstructural Features of Sol-Gel Derived BaTiO3 Nanoparticles," Materials 2021, Vol. 14, Page 4345, vol. 14, no. 15, p. 4345, Aug. 2021, doi: 10.3390/MA14154345.*

[86] *Y. Zhao, Q. Wang, J. H. Lv, X. Zhao, and C. M. Wang, "Dielectric properties and electrocaloric effect of yttrium-modified BaTiO3 ceramics," Ceram Int, vol. 47, no. 13, pp. 18610–18618, Jul. 2021, doi: 10.1016/J.CERAMINT.2021.03.192.*

[87] *I. C. Amaechi et al., "Ultrafast microwave-assisted hydrothermal synthesis and photocatalytic behaviour of ferroelectric Fe3+-doped BaTiO3 nanoparticles under simulated sunlight," Catal Today, vol. 360, pp. 90–98, Jan. 2021, doi: 10.1016/J.CATTOD.2019.07.021.*

[88] *W. Peng, L. Li, S. Yu, P. Yang, and K. Xu, "Dielectric properties, microstructure and charge compensation of MnO2-doped BaTiO3-based ceramics in a reducing atmosphere," Ceram Int, Jul. 2021, doi: 10.1016/J.CERAMINT.2021.07.083.*

[89] *M. Naveed-Ul-Haq, "Exploring Ba(Ti, Sn)O3: An experimental and theoretical study of structural, ferroelectric, electronic, and optical properties," Mater Today Commun, vol. 28, p. 102494, Sep. 2021, doi: 10.1016/J.MTCOMM.2021.102494.*

[90] *Q. Xu and Z. Li, "Dielectric and ferroelectric behaviour of Zr-doped BaTiO3 perovskites," Processing and Application of Ceramics, vol. 14, no. 3, pp. 188–194, Jul. 2020, doi: 10.2298/PAC2003188X.*

[91] *G. M. Osoro, D. Bregiroux, M. P. Thi, and F. Levassort, "Structural and piezoelectric properties evolution induced by cobalt doping and cobalt/niobium co-doping in BaTiO3," Mater Lett, vol. 166, pp. 259–262, 2016, doi: 10.1016/j.matlet.2015.12.086.*

[92] S. Rajan, P. M. M. Gazzali, and G. Chandrasekaran, "Electrical and magnetic phase transition studies of Fe and Mn co-doped BaTiO3," J Alloys Compd, vol. 656, pp. 98–109, Jan. 2016, doi: 10.1016/J.JALLCOM.2015.09.199.

[93] K. Madhan and R. Murugaraj, "Structural, electrical, and weak ferromagnetic-to-antiferromagnetic nature of Ni and La co-doped BaTiO3 by sol–gel combustion route," Journal of Sol-Gel Science and Technology 2020 95:1, vol. 95, no. 1, pp. 11–21, May 2020, doi: 10.1007/S10971-020-05311-1.

[94] A. Jain and A. K. Panwar, "Synergetic effect of rare-earths doping on the microstructural and electrical properties of Sr and Ca co-doped BaTiO3 nanoparticles," Ceram Int, vol. 46, no. 8, pp. 10270–10278, Jun. 2020, doi: 10.1016/J.CERAMINT.2020.01.020.

[95] M. Arshad et al., "Fabrication, structure, and frequency-dependent electrical and dielectric properties of Sr-doped BaTiO3 ceramics," Ceram Int, vol. 46, no. 2, pp. 2238–2246, Feb. 2020, doi: 10.1016/J.CERAMINT.2019.09.208.

[96] S. Yadav, M. Chandra, R. Rawat, V. Sathe, A. K. Sinha, and K. Singh, "Structural correlations in the enhancement of ferroelectric property of Sr doped BaTiO3," Journal of Physics: Condensed Matter, vol. 32, no. 44, p. 445402, Aug. 2020, doi: 10.1088/1361-648X/ABA384.

[97] B. Yang et al., "Insights into the tribo-/pyro-catalysis using Sr-doped BaTiO3 ferroelectric nanocrystals for efficient water remediation," Chemical Engineering Journal, vol. 416, p. 128986, Jul. 2021, doi: 10.1016/J.CEJ.2021.128986.

[98] R. Verma, A. Chauhan, K. M. Batoo, R. Kumar, M. Hadi, and E. H. Raslan, "Structural, morphological, and optical properties of strontium doped lead-free BCZT ceramics," Ceram Int, vol. 47, no. 11, pp. 15442–15457, Jun. 2021, doi: 10.1016/j.ceramint.2021.02.110.

[99] P. Ren et al., "Effects of doping sites on electrical properties of yttrium doped BaTiO3," Mater Lett, vol. 174, pp. 197–200, Jul. 2016, doi: 10.1016/j.matlet.2016.03.110.

[100] S. Mittal, R. Laishram, and K. C. Singh, "Multi-phase coexistence in yttrium-substituted Ba0.9Ca0.1Zr0.07Ti0.93O3 lead-free piezoceramics," Ceram Int, vol. 45, no. 1, pp. 1237–1245, Jan. 2019, doi: 10.1016/J.CERAMINT.2018.09.312.

[101] J. Suchanicz, P. Czaja, K. Kluczewska, H. Czternastek, M. Sokolowski, and A. Węgrzyn, "The Influence of Pb(Mg1/3Nb2/3)O3-doping on the thermoelectric properties of BaTiO3 ceramics," Phase Transitions, vol. 91, no. 9–10, pp. 1036–1043, 2018, doi: 10.1080/01411594.2018.1506880.

[102] M. Tihtih, J. F. M. Ibrahim, E. Kurovics, and M. Abdelfattah, " Study on the effect of Bi dopant on the structural and optical properties of BaTiO 3 nanoceramics synthesized via sol-gel method ," J Phys Conf Ser, vol. 1527, p. 012043, 2020, doi: 10.1088/1742-6596/1527/1/012043.

[103] P. P. Khirade, S. D. Birajdar, A. V. Raut, and K. M. Jadhav, "Effect of Fe – substitution on phase transformation, optical, electrical and dielectrical properties of BaTiO3 nanoceramics synthesized by sol-gel auto combustion method," J Electroceram, vol. 37, no. 1–4, pp. 110–120, Dec. 2016, doi: 10.1007/S10832-016-0044-Z/TABLES/1.

[104] M. Afqir, M. Elaatmani, A. Zegzouti, A. Oufakir, and M. Daoud, "Sol–gel synthesis, structural and dielectric properties of Y-doped BaTiO 3 ceramics," Journal of Materials Science: Materials in Electronics, vol. 30, no. 6, pp. 5495–5502, Mar. 2019, doi: 10.1007/S10854-019-00843-X/FIGURES/10.

[105] H. Z. Ye and X. Y. Liu, "Review of recent studies in magnesium matrix composites," Journal of Materials Science 2004 39:20, vol. 39, no. 20, pp. 6153–6171, Oct. 2004, doi: 10.1023/B:JMSC.0000043583.47148.31.

[106] M. Lou et al., "Temperature-induced wear transition in ceramic-metal composites," Acta Mater, vol. 205, p. 116545, Feb. 2021, doi: 10.1016/J.ACTAMAT.2020.116545.

[107] Y. Qi, G. Chen, Z. Li, L. Chen, W. Han, and Z. Du, "A novel approach to fabricate ceramic/metal interpenetrating phase composites by ultrasonic-assisted spontaneous

infiltration," Ceram Int, vol. 47, no. 2, pp. 2903–2907, Jan. 2021, doi: 10.1016/J.CERAMINT.2020.09.121.

[108] S. Rathod, G. Tiwari, and D. Chougale, "Ballistic performance of ceramic–metal composite structures," Mater Today Proc, vol. 41, pp. 1125–1129, Jan. 2021, doi: 10.1016/J.MATPR.2020.08.759.

[109] A. M. Sadoun, A. W. Abdallah, I. M. R. Najjar, M. Basha, and M. Elmahdy, "Effect of lattice structure evolution and stacking fault energy on the properties of Cu–ZrO2/GNP nanocomposites," Ceram Int, vol. 47, no. 21, pp. 29598–29606, Nov. 2021, doi: 10.1016/J.CERAMINT.2021.07.129.

[110] E. K. Antwi, K. Liu, and H. Wang, "A review on ductile mode cutting of brittle materials," Frontiers of Mechanical Engineering 2018 13:2, vol. 13, no. 2, pp. 251–263, Feb. 2018, doi: 10.1007/S11465-018-0504-Z.

[111] J. Lin and H. Chen, "Effect of particle morphologies on the percolation of particulate porous media: A study of superballs," Powder Technol, vol. 335, pp. 388–400, Jul. 2018, doi: 10.1016/J.POWTEC.2018.05.015.

[112] N. Travitzky, "Processing of ceramic–metal composites," https://doi.org/10.1179/1743676111Y.0000000073, vol. 111, no. 5–6, pp. 286–300, Aug. 2013, doi: 10.1179/1743676111Y.0000000073.

[113] J. Niittynen, R. Abbel, M. Mäntysalo, J. Perelaer, U. S. Schubert, and D. Lupo, "Alternative sintering methods compared to conventional thermal sintering for inkjet printed silver nanoparticle ink," Thin Solid Films, vol. 556, pp. 452–459, Apr. 2014, doi: 10.1016/J.TSF.2014.02.001.

[114] H. Pastor, "Metallic Borides: Preparation of Solid Bodies — Sintering Methods and Properties of Solid Bodies," Boron and Refractory Borides, pp. 457–493, 1977, doi: 10.1007/978-3-642-66620-9_25.

[115] M. A. Awotunde, A. O. Adegbenjo, B. A. Obadele, M. Okoro, B. M. Shongwe, and P. A. Olubambi, "Influence of sintering methods on the mechanical properties of aluminium nanocomposites reinforced with carbonaceous compounds: A review," Journal of Materials Research and Technology, vol. 8, no. 2, pp. 2432–2449, Apr. 2019, doi: 10.1016/J.JMRT.2019.01.026.

[116] K. Biswas, A. S. Sharma, and B. Basu, "On the densification mechanisms and properties of Cu–Pb and Cu–Pb–TiB2 nanocomposites densified using spark plasma sintering," Scr Mater, vol. 69, no. 2, pp. 122–126, Jul. 2013, doi: 10.1016/J.SCRIPTAMAT.2013.02.046.

[117] B. V. Neamţu, I. Chicinaş, O. Isnard, I. Ciascai, F. Popa, and T. F. Marinca, "Consolidation and DC magnetic properties of nanocrystalline Supermalloy/iron composite cores prepared by spark plasma sintering," J Magn Magn Mater, vol. 353, pp. 6–10, Mar. 2014, doi: 10.1016/J.JMMM.2013.10.021.

[118] O. A. Graeve, M. S. Saterlie, R. Kanakala, S. D. De La Torre, and J. C. Farmer, "The kinetics of devitrification of amorphous alloys: The time–temperature–crystallinity diagram describing the spark plasma sintering of Fe-based metallic glasses," Scr Mater, vol. 69, no. 2, pp. 143–148, Jul. 2013, doi: 10.1016/J.SCRIPTAMAT.2013.02.019.

[119] Z. H. Zhang, Z. F. Liu, J. F. Lu, X. B. Shen, F. C. Wang, and Y. D. Wang, "The sintering mechanism in spark plasma sintering – Proof of the occurrence of spark discharge," Scr Mater, vol. 81, pp. 56–59, Jun. 2014, doi: 10.1016/J.SCRIPTAMAT.2014.03.011.

[120] M. Tihtih et al., "Role of A-site (Sr), B-site (Y), and A, B sites (Sr, Y) substitution in lead-free BaTiO3 ceramic compounds: Structural, optical, microstructure, mechanical, and thermal conductivity properties," Ceram Int, vol. 49, no. 2, pp. 1947–1959, Jan. 2023, doi: 10.1016/J.CERAMINT.2022.09.160.

[121] M. Tihtih et al., "Development of Yttrium-Doped BaTiO3 for Next-Generation Multilayer Ceramic Capacitors," ACS Omega, Feb. 2023, doi: 10.1021/ACSOMEGA.2C07497.

[122] W. L. Oberkampf and T. G. Trucano, "Verification and validation in computational fluid dynamics," Progress in Aerospace Sciences, vol. 38, no. 3, pp. 209–272, Apr. 2002, doi: 10.1016/S0376-0421(02)00005-2.

[123] J. H. Panchal, S. R. Kalidindi, and D. L. McDowell, "Key computational modeling issues in Integrated Computational Materials Engineering," Computer-Aided Design, vol. 45, no. 1, pp. 4–25, Jan. 2013, doi: 10.1016/J.CAD.2012.06.006.

[124] H. Huang, W. Qiu, O. K. Tan, W. Zhu, and L. M. Zhou, "Effect of excess TiO2 on the phase evolution and densification of sol-gel derived (Ba,Sr)TiO3 powders," J Electroceram, vol. 16, no. 4, pp. 337–341, 2006, doi: 10.1007/s10832-006-9875-3.

[125] P. P. Khirade, V. Vinayak, P. B. Kharat, and A. R. Chavan, "Green Synthesis of Ba1−xSrxTiO3 ceramic nanopowders by sol-gel combustion method using lemon juice as a fuel: Tailoring of Microstructure, ferroelectric, dielectric and electrical properties," Opt Mater (Amst), vol. 111, p. 110664, Jan. 2021, doi: 10.1016/J.OPTMAT.2020.110664.

[126] A. Moghtada, A. Heidary Moghadam, and R. Ashiri, "Tetragonality enhancement in BaTiO3 by mechanical activation of the starting BaCO3 and TiO2 powders: Characterization of the contribution of the mechanical activation and postmilling calcination phenomena," Int J Appl Ceram Technol, vol. 15, no. 6, pp. 1518–1531, Nov. 2018, doi: 10.1111/ijac.13019.

[127] L. R. K. T. Jacob, Shubhra Raj, "Vegard ' s law : a fundamental relation," International Journal of Materials Research, vol. 98, pp. 776–779, 2007.

[128] S. Lee and C. A. Randall, "A modified Vegard's law for multisite occupancy of Ca in BaTi O3 -CaTi O3 solid solutions," Appl Phys Lett, vol. 92, no. 11, pp. 1–4, 2008, doi: 10.1063/1.2857475.

[129] G. K. Williamson and W. H. Hall, "X-Ray broadening from filed aluminium and tungsten," Acta Metallurgica, vol. 1, pp. 22–31, 1953.

[130] A. King, R. Singh, R. Anand, S. K. Behera, and B. B. Nayak, "Phase and luminescence behaviour of Ce-doped zirconia nanopowders for latent fingerprint visualisation," Optik, vol. 242. 2021. doi: 10.1016/j.ijleo.2021.167087.

[131] P. P. Khirade, A. B. Shinde, A. V. Raut, S. D. Birajdar, and K. M. Jadhav, "Investigations on the synthesis, structural and microstructural characterizations of Ba1-xSrxZrO3 nanoceramics," Ferroelectrics, vol. 504, no. 1, pp. 216–229, 2016, doi: 10.1080/00150193.2016.1241633.

[132] M. Singh, B. C. Yadav, A. Ranjan, M. Kaur, and S. K. Gupta, "Synthesis and characterization of perovskite barium titanate thin film and its application as LPG sensor," Sens Actuators B Chem, vol. 241, pp. 1170–1178, 2017, doi: 10.1016/j.snb.2016.10.018.

[133] K. Niesz, T. Ould-Ely, H. Tsukamoto, and D. E. Morse, "Engineering grain size and electrical properties of donor-doped barium titanate ceramics," Ceram Int, vol. 37, no. 1, pp. 303–311, 2011, doi: 10.1016/j.ceramint.2010.08.040.

[134] Y. He, "Heat capacity, thermal conductivity, and thermal expansion of barium titanate-based ceramics," Thermochim Acta, vol. 419, no. 1–2, pp. 135–141, 2004, doi: 10.1016/j.tca.2004.02.008.

[135] J. Xing, M. Radovic, and A. Muliana, "Thermal properties of BaTiO3/Ag composites at different temperatures," Compos B Eng, vol. 90, pp. 287–301, 2016, doi: 10.1016/j.compositesb.2015.12.014.

[136] H. Muta, K. Kurosaki, and S. Yamanaka, "Thermoelectric properties of doped BaTiO3-SrTiO3 solid solution," J Alloys Compd, vol. 368, no. 1–2, pp. 22–24, 2004, doi: 10.1016/j.jallcom.2003.07.016.

[137] A. I. Hussein, A. N. C. Mat, N. A. A. Abd Wahab, I. Ab. Rahman, A. Husein, and Z. Ab-Ghani, "Synthesis and properties of novel calcia-stabilized zirconia (Ca-SZ) with nano calcium oxide derived from cockle shells and commercial source for dental application," Applied Sciences (Switzerland), vol. 10, no. 17, 2020, doi: 10.3390/APP10175751.

[138] *Y. Slimani, A. Selmi, E. Hannachi, M. A. Almessiere, A. Baykal, and I. Ercan, "Impact of ZnO addition on structural, morphological, optical, dielectric and electrical performances of BaTiO3 ceramics," Journal of Materials Science: Materials in Electronics, vol. 30, no. 10, pp. 9520–9530, May 2019, doi: 10.1007/S10854-019-01284-2/FIGURES/10.*

[139] *J. Liu, G. Jin, Y. Chen, and W. Xue, "Properties of yttrium-doped barium titanate ceramics with positive temperature coefficient of resistivity and a novel method to evaluate the depletion layer width," Ceram Int, vol. 45, no. 5, pp. 6119–6124, Apr. 2019, doi: 10.1016/J.CERAMINT.2018.12.086.*

[140] *C. H. Kim, K. J. Park, Y. J. Yoon, M. H. Hong, J. O. Hong, and K. H. Hur, "Role of yttrium and magnesium in the formation of core-shell structure of BaTiO3 grains in MLCC," J Eur Ceram Soc, vol. 28, no. 6, pp. 1213–1219, Jan. 2008, doi: 10.1016/J.JEURCERAMSOC.2007.09.042.*

[141] *M. Tihtih, J. F. M. Ibrahim, E. Kurovics, and M. Abdelfattah, "Study on the effect of Bi dopant on the structural and optical properties of BaTiO3 nanoceramics synthesized via sol-gel method," J Phys Conf Ser, vol. 1527, no. 1, 2020, doi: 10.1088/1742-6596/1527/1/012043.*

[142] *M. Tihtih et al., "Enhanced optical and thermal conductivity properties of barium titanate ceramic via strontium doping for thermo-optical applications," Opt Quantum Electron, vol. 55, no. 3, pp. 1–20, Mar. 2023, doi: 10.1007/S11082-022-04516-8/TABLES/3.*

[143] *J. Qi, L. Li, Y. Wang, Y. Fan, and Z. Gui, "Yttrium doping behavior in BaTiO3 ceramics at different sintered temperature," Mater Chem Phys, vol. 82, no. 2, pp. 423–427, Nov. 2003, doi: 10.1016/S0254-0584(03)00264-5.*

[144] *M. Reda, S. I. El-Dek, and M. M. Arman, "Improvement of ferroelectric properties via Zr doping in barium titanate nanoparticles," Journal of Materials Science: Materials in Electronics, vol. 33, no. 21, pp. 16753–16776, Jul. 2022, doi: 10.1007/S10854-022-08541-X/TABLES/8.*

[145] *E. Hannachi, M. A. Almessiere, Y. Slimani, R. B. Alshamrani, G. Yasin, and F. Ben Azzouz, "Preparation and characterization of high-Tc (YBa2Cu3O7-δ)1-x/(CNTs)x superconductors with highly boosted superconducting performances," Ceram Int, vol. 47, no. 16, pp. 23539–23548, Aug. 2021, doi: 10.1016/J.CERAMINT.2021.05.071.*

[146] *W. J. Choi, D. Yang, S. C. Jeon, and K. S. Moon, "Effect of charge compensation change on the crystal structure, grain growth behavior, and dielectric properties in the La2O3-doped BaTiO3 system with MnCO3 addition," J Alloys Compd, vol. 916, p. 165388, Sep. 2022, doi: 10.1016/J.JALLCOM.2022.165388.*

[147] *E. Hannachi et al., "Impact of tin oxide on the structural features and radiation shielding response of some ABO3 perovskites ceramics (A = Ca, Sr, Ba; B = Ti)," Appl Phys A Mater Sci Process, vol. 127, no. 12, pp. 1–12, Dec. 2021, doi: 10.1007/S00339-021-05092-6/FIGURES/16.*

[148] *H. Kacem et al., "Deep understanding of structural and physical properties of BaTiO3 over a broad temperature range," Inorg Chem Commun, vol. 144, p. 109771, Oct. 2022, doi: 10.1016/J.INOCHE.2022.109771.*

[149] *O. Ruzimuradov, G. Hasegawa, K. Kanamori, and K. Nakanishi, "Preparation of Hierarchically Porous Nanocrystalline CaTiO3, SrTiO3 and BaTiO3 Perovskite Monoliths," Journal of the American Ceramic Society, vol. 94, no. 10, pp. 3335–3339, Oct. 2011, doi: 10.1111/J.1551-2916.2011.04613.X.*

[150] *A. Garrido-Hernández et al., "Structural studies of BaTiO3:Er3+ and BaTiO3:Yb3+ powders synthesized by hydrothermal method," Journal of Rare Earths, vol. 32, no. 11, pp. 1016–1021, Nov. 2014, doi: 10.1016/S1002-0721(14)60176-9.*

[151] *K. S. Park, "Structural and electrical properties of FeMg0.7Cr0.6Co0.7−xAlxO4 (0 ≤ x ≤ 0.3) thick film NTC thermistors," J Eur Ceram Soc, vol. 26, no. 6, pp. 909–914, Jan. 2006, doi: 10.1016/J.JEURCERAMSOC.2004.12.021.*

[152] *T. Badapanda et al., "Optical and dielectric study of strontium modified barium zirconium titanate ceramic prepared by high energy ball milling," J Alloys Compd, vol. 645, pp. 586–596, Oct. 2015, doi: 10.1016/J.JALLCOM.2015.05.005.*

[153] *C. Pascual-Gonzalez et al., "Continuously controllable optical band gap in orthorhombic ferroelectric KNbO3-BiFeO3 ceramics," Appl Phys Lett, vol. 110, no. 17, p. 172902, Apr. 2017, doi: 10.1063/1.4982600.*

[154] *C. Pascual-Gonzalez et al., "Band gap evolution and a piezoelectric-to-electrostrictive crossover in (1 − x)KNbO 3 – x (Ba 0.5 Bi 0.5)(Nb 0.5 Zn 0.5)O 3 ceramics," J Mater Chem C Mater, vol. 5, no. 8, pp. 1990–1996, Feb. 2017, doi: 10.1039/C6TC05515J.*

[155] *W. Zhou, H. Deng, L. Yu, P. Yang, and J. Chu, "Magnetism switching and band-gap narrowing in Ni-doped PbTiO3 thin films," J Appl Phys, vol. 117, no. 19, p. 194102, May 2015, doi: 10.1063/1.4921459.*

[156] *X. Chen et al., "Influence of transition metal doping (X = Mn, Fe, Co, Ni) on the structure and bandgap of ferroelectric Bi3.15Nd0.85Ti2X1O12," J Phys D Appl Phys, vol. 50, no. 10, p. 105104, Feb. 2017, doi: 10.1088/1361-6463/AA5624.*

[157] *W. S. Choi and H. N. Lee, "Strain tuning of electronic structure in B i4 T i3 O12-LaCo O3 epitaxial thin films," Phys Rev B Condens Matter Mater Phys, vol. 91, no. 17, p. 174101, May 2015, doi: 10.1103/PHYSREVB.91.174101/FIGURES/4/MEDIUM.*

[158] *G. Li, J. Xie, J. Wang, L. Xia, Y. Li, and W. Hu, "Nanoscale Surface Disorder for Enhanced Solar Absorption and Superior Visible-Light Photocatalytic Property in Ti-Rich BaTiO3 Nanocrystals," ACS Omega, vol. 4, no. 6, pp. 9673–9679, Jun. 2019, doi: 10.1021/ACSOMEGA.9B00739/ASSET/IMAGES/LARGE/AO-2019-00739Y_0001.JPEG.*

[159] *A. Alshoaibi, M. B. Kanoun, B. Ul Haq, S. Alfaify, and S. Goumri-Said, "Insights into the Impact of Yttrium Doping at the Ba and Ti Sites of BaTiO3on the Electronic Structures and Optical Properties: A First-Principles Study," ACS Omega, vol. 5, no. 25, pp. 15502–15509, Jun. 2020, doi: 10.1021/ACSOMEGA.0C01638/ASSET/IMAGES/MEDIUM/AO0C01638_M001.GIF.*

[160] *A. MADANI, M. Alghamdi, B. Alamri, and shoaa Althobaiti, "Structural and Optical Properties Of Sb-Batio3 and Y- Batio3 Doped Ceramics Prepared by Solid-State Reaction."*

[161] *R. Yin, Y. Zhang, W. Zhao, X. Huang, X. Li, and L. Qian, "Graphene platelets/aluminium nitride metacomposites with double percolation property of thermal and electrical conductivity," J Eur Ceram Soc, vol. 38, no. 14, pp. 4701–4706, Nov. 2018, doi: 10.1016/J.JEURCERAMSOC.2018.06.036.*

[162] *C.-S. Park, W. Han, D. Il Shim, H. H. Cho, and H.-H. Park, " The Effect of Mesoporous Structure on the Thermoelectric Properties of Nonstoichiometric La-Doped SrTiO 3 ," J Electrochem Soc, vol. 163, no. 6, pp. E155–E158, Mar. 2016, doi: 10.1149/2.0441606JES/XML.*

[163] *J. Suchanicz, P. Czaja, K. Kluczewska, H. Czternastek, M. Sokolowski, and A. Węgrzyn, "The Influence of Pb(Mg1/3Nb2/3)O3-doping on the thermoelectric properties of BaTiO3 ceramics," https://doi.org/10.1080/01411594.2018.1506880, vol. 91, no. 9–10, pp. 1036–1043, Oct. 2018, doi: 10.1080/01411594.2018.1506880.*

[164] *X. Xiao et al., "Tailoring the structure and thermoelectric properties of BaTiO3via Eu2+ substitution," Physical Chemistry Chemical Physics, vol. 19, no. 21, pp. 13469–13480, May 2017, doi: 10.1039/C7CP00020K.*

[165] *Y. Hudiono, A. Greenstein, C. Saha-Kuete, B. Olson, S. Graham, and S. Nair, "Effects of composition and phonon scattering mechanisms on thermal transport in MFI zeolite films," J Appl Phys, vol. 102, no. 5, p. 053523, Sep. 2007, doi: 10.1063/1.2776006.*

[166] *K. D. Parrish, J. R. Abel, A. Jain, J. A. Malen, and A. J. H. McGaughey, "Phonon-boundary scattering in nanoporous silicon films: Comparison of Monte Carlo techniques," J Appl Phys, vol. 122, no. 12, p. 125101, Sep. 2017, doi: 10.1063/1.4993601.*

[167] *H. Lee, D. Vashaee, D. Z. Wang, M. S. Dresselhaus, Z. F. Ren, and G. Chen, "Effects of nanoscale porosity on thermoelectric properties of SiGe," J Appl Phys, vol. 107, no. 9, p. 094308, May 2010, doi: 10.1063/1.3388076.*

[168] *H. Obara, A. Yamamoto, C. H. Lee, K. Kobayashi, A. Matsumoto, and R. Funahashi, "Thermoelectric properties of Y-doped polycrystalline SrTiO3," Japanese Journal of Applied Physics, Part 2: Letters, vol. 43, no. 4 B, p. L540, Apr. 2004, doi: 10.1143/JJAP.43.L540/XML.*

[169] *S. Saini, J. Shah, R. K. Kotnala, and K. L. Yadav, "Nickel substituted oxygen deficient nanoporous lithium ferrite based green energy device hydroelectric cell," J Alloys Compd, vol. 827, p. 154334, Jun. 2020, doi: 10.1016/J.JALLCOM.2020.154334.*

[170] *J. Shah, A. Shukla, M. Kar, G. Gupta, S. Jain, and R. K. Kotnala, "ZnO nanoflakes self-assembled from the water splitting process using a hydroelectric cell," React Chem Eng, vol. 7, no. 8, pp. 1836–1846, Jul. 2022, doi: 10.1039/D2RE00094F.*

[171] *X. Li et al., "Synthesis and properties of Y-doped SrTiO3 as an anode material for SOFCs," J Power Sources, vol. 166, no. 1, pp. 47–52, Mar. 2007, doi: 10.1016/J.JPOWSOUR.2007.01.008.*

[172] *X. Wang, P. Ren, Q. Wang, H. Fan, and G. Zhao, "Dielectric, piezoelectric and conduction properties of yttrium acceptor-doped BaTiO3 ceramics," Journal of Materials Science: Materials in Electronics, vol. 27, no. 11, pp. 11762–11769, Nov. 2016, doi: 10.1007/S10854-016-5315-6/FIGURES/6.*

[173] *Q. Sun et al., "Sol-hydrothermal synthesis, crystal structures and excellent dielectric stability of yttrium doped BaTiO3 ceramics," https://doi.org/10.1080/10667857.2016.1253265, vol. 31, no. 14, pp. 854–859, Dec. 2016, doi: 10.1080/10667857.2016.1253265.*

[174] *I. Sakaguchi et al., "Oxygen Diffusion in Rare-Earth Doped BaTiO3 Ceramics," Key Eng Mater, vol. 582, pp. 189–193, 2014, doi: 10.4028/WWW.SCIENTIFIC.NET/KEM.582.189.*

[175] *G. Panomsuwan and H. Manuspiya, "Structural and dielectric properties of sol–gel derived Ba1–xSrxTiO3 (0 ≤ x ≤ 0.5) ceramics for energy storage applications," Mater Res Express, vol. 6, no. 2, p. 026310, Nov. 2018, doi: 10.1088/2053-1591/AAEDF2.*

[176] *C. L. Freeman, J. A. Dawson, H. R. Chen, J. H. Harding, L. Bin Ben, and D. C. Sinclair, "A new potential model for barium titanate and its implications for rare-earth doping," J Mater Chem, vol. 21, no. 13, pp. 4861–4868, Mar. 2011, doi: 10.1039/C0JM04058D.*

[177] *R. A. Eichel, "Defect structure of oxide ferroelectrics-valence state, site of incorporation, mechanisms of charge compensation and internal bias fields : IInvited review for J. Electroceram.," J Electroceram, vol. 19, no. 1, pp. 9–21, Sep. 2007, doi: 10.1007/S10832-007-9068-8/FIGURES/7.*

[178] *S. Lee, W. H. Woodford, and C. A. Randall, "Crystal and defect chemistry influences on band gap trends in alkaline earth perovskites," Appl Phys Lett, vol. 92, no. 20, p. 201909, May 2008, doi: 10.1063/1.2936091.*

[179] *M. Ferrari and L. Lutterotti, "Method for the simultaneous determination of anisotropic residual stresses and texture by x-ray diffraction," J Appl Phys, vol. 76, no. 11, p. 7246, Jun. 1998, doi: 10.1063/1.358006.*

[180] *S. E. Zaki et al., "Role of oxygen vacancies in vanadium oxide and oxygen functional groups in graphene oxide for room temperature CO 2 gas sensors," Sens Actuators A Phys, vol. 294, pp. 17–24, Aug. 2019, doi: 10.1016/j.sna.2019.04.037.*

[181] *G. Choi, A. H. Choi, L. A. Evans, S. Akyol, and B. Ben-Nissan, "A review: Recent advances in sol-gel-derived hydroxyapatite nanocoatings for clinical applications," Journal of the American Ceramic Society, vol. 103, no. 10, pp. 5442–5453, Sep. 2020, doi: 10.1111/jace.17118.*

[182] *M. Ganguly, S. K. Rout, C. W. Ahn, I. W. Kim, and M. Kar, "Structural, electrical and optical properties of Ba(Ti1−xYb4x/3)O3 ceramics," Ceram Int, vol. 39, no. 8, pp. 9511–9524, Dec. 2013, doi: 10.1016/J.CERAMINT.2013.05.070.*

[183] *H. Y. Tian et al., "Determination of the optical properties of sol-gel-derived BaxSr1-xTiO3 thin film by spectroscopic ellipsometry," Journal of Physics: Condensed Matter, vol. 13, no. 18, p. 4065, May 2001, doi: 10.1088/0953-8984/13/18/314.*

[184] *S. Parida, A. Satapathy, E. Sinha, A. Bisen, and S. K. Rout, "Effect of Neodymium on Optical Bandgap and Microwave Dielectric Properties of Barium Zirconate Ceramic," Metall Mater Trans A Phys Metall Mater Sci, vol. 46, no. 3, pp. 1277–1286, Mar. 2015, doi: 10.1007/S11661-014-2725-Z/TABLES/3.*

[185] *T. T. Khan and S. C. Ur, "Thermoelectric properties of the yttrium-doped ceramic oxide SrTiO3," Journal of the Korean Physical Society 2017 70:1, vol. 70, no. 1, pp. 93–97, Jan. 2017, doi: 10.3938/JKPS.70.93.*

[186] *H. Muta, K. Kurosaki, and S. Yamanaka, "Thermoelectric properties of rare earth doped SrTiO3," J Alloys Compd, vol. 350, no. 1–2, pp. 292–295, Feb. 2003, doi: 10.1016/S0925-8388(02)00972-6.*

[187] *J. Liu et al., "Influence of rare earth doping on thermoelectric properties of SrTiO3 ceramics," J Appl Phys, vol. 114, no. 22, p. 223714, Dec. 2013, doi: 10.1063/1.4847455.*

[188] *C. J. Xiao, "A study on the damping capacity of BaTiO3-reinforced Al-matrix composites," Bulletin of Materials Science, vol. 39, no. 2, pp. 463–467, Apr. 2016, doi: 10.1007/S12034-016-1171-5/FIGURES/7.*

[189] *H. Y. Lee, J. S. Kim, N. M. Hwang, and D. Y. Kim, "Effect of sintering temperature on the secondary abnormal grain growth of BaTiO3," J Eur Ceram Soc, vol. 20, no. 6, pp. 731–737, May 2000, doi: 10.1016/S0955-2219(99)00197-1.*

[190] *N. Xu, Y. P. Pu, B. Wang, H. D. Wu, and K. Chen, "Microstructure and electrical properties of BaTiO3/Cu ceramic composite sintered in nitrogen atmosphere," Ceram Int, vol. 38, no. SUPPL. 1, pp. S249–S253, Jan. 2012, doi: 10.1016/J.CERAMINT.2011.04.094.*

[191] *Z. Yang et al., "Grain size engineered lead-free ceramics with both large energy storage density and ultrahigh mechanical properties," Nano Energy, vol. 58, pp. 768–777, Apr. 2019, doi: 10.1016/J.NANOEN.2019.02.003.*

[192] *C. N. Berglund and H. J. Braun, "Optical Absorption in Single-Domain Ferroelectric Barium Titanate," Physical Review, vol. 164, no. 2, p. 790, Dec. 1967, doi: 10.1103/PhysRev.164.790.*

[193] *Z. Yu and C. Ang, "Maxwell–Wagner polarization in ceramic composites BaTiO3–(Ni0.3Zn0.7)Fe2.1O4," J Appl Phys, vol. 91, no. 2, pp. 794–797, Jan. 2002, doi: 10.1063/1.1421033.*

[194] *D. O'Neill, R. M. Bowman, and J. M. Gregg, "Dielectric enhancement and Maxwell–Wagner effects in ferroelectric superlattice structures," Appl Phys Lett, vol. 77, no. 10, pp. 1520–1522, Sep. 2000, doi: 10.1063/1.1290691.*

[195] *K. Górska and A. Horzela, "The Volterra type equations related to the non-Debye relaxation," Commun Nonlinear Sci Numer Simul, vol. 85, p. 105246, Jun. 2020, doi: 10.1016/J.CNSNS.2020.105246.*

[196] *A. Rached, M. A. Wederni, K. Khirouni, S. Alaya, R. J. Martín-Palma, and J. Dhahri, "Structural, optical and electrical properties of barium titanate," Mater Chem Phys, vol. 267, p. 124600, Jul. 2021, doi: 10.1016/J.MATCHEMPHYS.2021.124600.*

[197] *M. Tyunina, "Conductivity in Ferroelectric Barium Titanate: Electrons Versus Oxygen Vacancies," IEEE Trans Ultrason Ferroelectr Freq Control, vol. 68, no. 2, pp. 296–302, Feb. 2021, doi: 10.1109/TUFFC.2020.2978901.*

[198] *C. Deng et al., "Spark plasma sintered graphene/copper calcium titanate ceramic composites with negative permittivity and enhanced thermal conductivity," Ceram Int, vol. 49, no. 10, pp. 16149–16155, May 2023, doi: 10.1016/J.CERAMINT.2023.01.212.*